Reactive Hydride Composites for Efficient Hydrogen Energy Storage

Christopher Chinedu Nwakwuo

St Cross College

A thesis submitted for the degree of Doctor of Philosophy

Department of Materials

University of Oxford

Hilary Term 2011

Abstract

Solid state chemical storage of hydrogen in metals offers promising advantages over compressed hydrogen gas and condensed liquid hydrogen, especially for mobile applications with respect to safety and energy efficiency. However, no single metal hydride simultaneously satisfies the essential performance criteria for onboard hydrogen storage namely, high gravimetric and/or volumetric energy density, fast kinetics and favorable thermodynamics.

Recently, a breakthrough achievement was made by the development of reactive hydride composites in which two metal hydride systems (e.g. $NaBH_4$ and MgH_2) are mixed together resulting in better sorption properties than the individual pure systems. In this approach, the formation of MgB_2 by exothermic reaction destabilizes the composite and consequently reduces the overall enthalpy and sorption temperature of the endothermic desorption reaction.

In this work the thermodynamic and kinetic properties of reactions in $2NaH + MgB_2 + 4H_2 \leftrightarrow 2NaBH_4 + MgH_2$ and $3NaH + MgB_2 + 4H_2 \leftrightarrow 2NaBH_4 + NaMgH_3$ were established using multiple experimental techniques like volumetric measurements, ex-situ and in-situ X-ray diffraction, calorimetry, and especially electron microscopy.

Under the applied experimental conditions of 50 bar hydrogen and 400 ^oC during the hydrogenation of $2NaH + MgB_2$ and 0.1 bar hydrogen and 450 ^oC during the dehydrogenation of $2NaBH_4 + MgH_2$, both reactions were kinetically limited and proceeded in multisteps. The absorption reaction was partial, being restricted by the unexpected formation of $NaMgH_3$ which limits the formation of $NaBH_4$ while the desorption reaction was complete and limited by the growth of MgB_2 through some intermediate complexes at the $Mg/NaBH_4$ interface where the intermediate phase forms a barrier to diffusion.

Conversely, in the $3NaH + MgB_2$ system, absorption in 100 bar hydrogen and 300 ^oC was complete but slow, while in the $2NaBH_4 + NaMgH_3$ system, complete desorption was achieved in multisteps under 0.1 bar hydrogen and 450 ^oC.

The formation of intermediate and stable complexes during these reactions poses a significant restraint to hydrogen sorption reactions. However, lower onset sorption temperatures have been established in these systems than in the pure compounds due to their simultaneous destabilization in the composite state.

This study have demonstrated the complexity of desorption and absorption mechanisms in these composite systems and the difficulty of obtaining such reactions at low temperatures required for mobile applications. This understanding of the rate limiting reaction steps in reactive hydride composites provides the basis for further optimization of these materials for efficient hydrogen storage applications.

Preface

The research described in this thesis was carried out by the author in the Department of Materials, University of Oxford under the supervision of Prof. John M. Sykes and Dr. John L. Hutchison. Part of this work have been published in peer-reviewed journals and presented at international conferences as follows:

Peer-reviewed papers:

- C. C. Nwakwuo, C. Pistidda, M. Dornheim , J. L. Hutchison, J. M. Sykes "*Microstructural analysis of hydrogen absorption in 2NaH + MgB_2*", Scripta Materiala. 64 (4), 351-354, 2010.

- C. C. Nwakwuo, C. Pistidda, M. Dornheim, J. L. Hutchison, J. M. Sykes "*Microstructural study of hydrogen desorption in $2NaBH_4$ + MgH_2 reactive hydride composite*", International Journal of Hydrogen Energy. 37 (3), 2382-2387, 2011.

- C. C. Nwakwuo, J. L. Hutchison, J. M. Sykes "*Hydrogen sorption in 3NaH + MgB_2/ $2NaBH_4$ + $NaMgH_3$ reactive hydride composite,* Scripta Materiala. 66 (3-4), 175-177, 2011.

- D. Pottmaier, S. Garroni, C. Pistidda, C. C. Nwakwuo, M.Orlova, D. Cakir, F.Dolci, G.Vaughan, J. Sykes, M. D. Barò, G. H. L. A. Brocks, W. Lohstroh, M. Dornheim, M. Baricco "*Hydrogen sorption in $NaBH_4$/MgH_2 reactive hydride composite,* Acta Materialia (submitted).

International conference proceedings and workshops:

- C. C. Nwakwuo, C. Pistidda, M. Dornheim , J. L. Hutchison, J. M. Sykes "*Microstructural analysis of hydrogen absorption in 2NaH + MgB_2*", Materials Research Society, Fall Meeting , Nov. 29 - December 03, 2010, Boston-USA.

- C. C. Nwakwuo, J. L. Hutchison, J. M. Sykes "*Microstructural study of hydrogen sorption in reactive hydride composites*" International Workshop on Solid State Hydrogen Storage, October 5-6, 2010, Torino- Italy.

- C. C. Nwakwuo, J. L. Hutchison, J. M. Sykes, *"Structural transformations during hydrogen sorption in 2NaH + MgB_2/$2NaBH_4$ + MgH_2"* International Conference on Materials for Energy, July 4-8, 2010, Karlsruhe-Germany.

- 18th World Hydrogen Energy Conference, *"Hydrogen production technologies, storage systems and fuel cells"* June 16-21, 2010, Essen-Germany.

Acknowledgements

First and foremost, I would like to express my heartfelt gratitude to my supervisors Prof. John M. Sykes and Dr. John L. Hutchison who were a constant source of motivation and inspiration throughout this research project. Their constructive guidance and encouragement to take real initiative in solving experimental and analytical problems made this work successful.

I am greatly thankful to Mr. Claudio Pistidda at GKSS research center Germany, for his collaboration during the duration of the COSY project. I am also grateful to Dr. Martin Dornheim for his very useful contributions. Further thanks are due to the department of Nanotechnology at GKSS Research Center Germany, for supplying most of the materials used in this project.

I would like to express my thanks to the electron microscopy technical support group at the Department of Materials, University of Oxford for being incredibly helpful by providing training in various electron microscopy and analytical techniques required to carry out the experiments. I acknowledge with special thanks, the many helpful contributions of Dr. Sergio Lozano-Perez during this project.

I wish to acknowledge my college advisor, Professor Peter Brocklehurst for his encouragement and inspiring discussions.

I am sincerely grateful to the European Commission for the financial support provided through the Marie Curie Research Training Network MRTN-CT-2006-035366 as well as the Department of Materials, University of Oxford.

I would like to thank all my friends and colleagues I met in Oxford for their help and valuable conversations.

Lastly, I am deeply grateful and indebted to my family for their constant and unwavering love and support and wish to dedicate this thesis to them.

Contents

1.0 Introduction

1.1 Moving beyond the fossil fuel age

The growth and development of world economies over past decades have resulted in escalating demand for energy and raised serious environmental challenges notably, global warming and adverse climate changes due to increased green-house gas emissions from industrial, agricultural and transportation systems. Furthermore, over a longer time scale, fossil energy reserves will drastically reduce and eventually be depleted. These issues have stimulated immense interest in the gradual transition from the current hydrocarbon-driven economy to renewable and environmentally friendly energy systems e.g. solar energy, hydro power, hydrogen energy, wind power, geo-thermal energy and bio-fuel.

Hydrogen is an ideal energy carrier and may play a key role in future energy storage, distribution and conversion within a comprehensive clean-energy system. Hydrogen is essentially non-polluting, as its combustion produces only water. In addition, it is naturally abundant, constituting approximately three-quarters of the universe's elemental mass.

The concept of zero CO_2-emission can be realized by a fuel cell which utilizes hydrogen as its primary fuel. Fuel cells are not limited by the Carnot cycle and thus offer higher energy efficiency than fossil-fuel internal combustion engines. Hydrogen has the highest gravimetric energy density of any chemical fuel. It has three times the gravimetric energy density of gasoline (120 $MJkg^{-1}$ and 44 $MJkg^{-1}$

for hydrogen and gasoline respectively) [1]. Although hydrogen energy is at present more expensive than petroleum, it can be produced at relatively low cost by splitting of water through electrolytic, photochemical or biological means. As indicated in figure 1, the hydrogen-based energy cycle, consists of three major links; (1) production of hydrogen, (2) storage of hydrogen and (3) transformation of energy stored in hydrogen. Clean electrical energy can be generated by a fuel cell with water as the only by-product. Thus carbon dioxide and other green-house emissions are avoided.

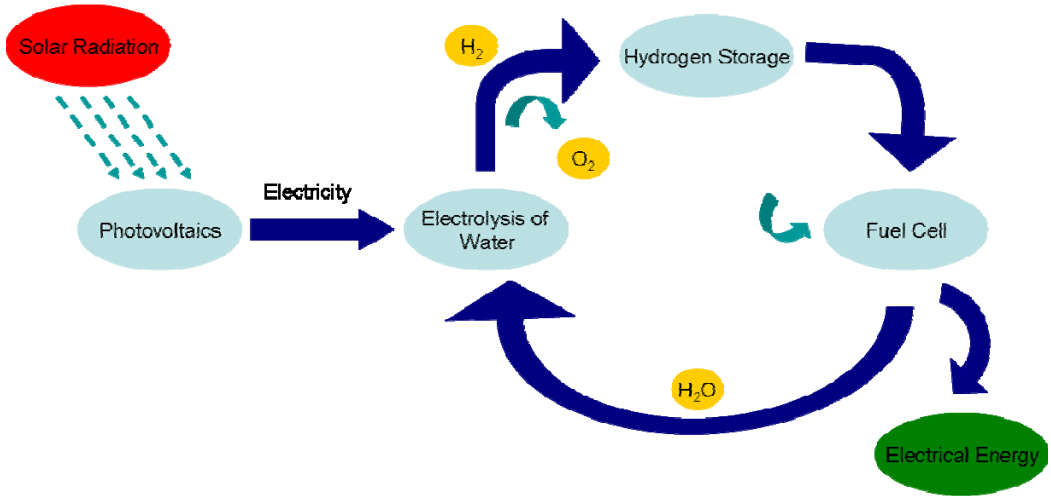

Figure 1.1: Schematic of the hydrogen energy cycle based on photovoltaics and fuel cells.

While hydrogen has great potential as an efficient fuel, its large-scale use in fuel cells for mobile applications is limited by the absence of a suitable and efficient method for onboard storage. Renewable energy resources are generally intermittent; hence the need for intermediate storage is obvious, especially for mobile applications.

1.2 Hydrogen storage

Hydrogen can be stored as compressed gas, cryogenic liquid or by absorption into solid as metal hydrides. While gas and liquid storage systems are conventional technologies in a provisional hydrogen economy, solid storage as metal hydrides is still undergoing research and development and knowledge of the reaction mechanism is fledgy. Table 1 lists the various properties of these hydrogen storage methods. They are further discussed to illustrate their advantages and disadvantages.

Table 1.1: Properties of hydrogen storage methods [2].

Storage Properties	**Units**	**Gas storage**	**Liquid storage**	**Solid storage (metal hydride)**
Temperature	^{o}C	25	-252	25-400
Pressure	Bar	700	1	1
Volumetric density	kg H_2L^{-1} (%)	~4	7	~15
Gravimetric density	kg H_2Kg^{-1} (%)	13	~2	<18

Compressed hydrogen at ambient temperature is the most developed and commercially available hydrogen storage technique. The very low density (0.09 g L^{-1}) of hydrogen at 1 bar (in comparison to carbonaceous fuels) demands high pressures in the order of 400-700 bars to achieve sufficient volumetric and

gravimetric energy densities. This poses high weight, energy and cost constraints on the design and production of reinforced pressure-resistant containers. Additionally, the safety of pressurized tanks due to risk of leakage or rupture is an issue of utmost concern especially in mobile applications.

Condensed hydrogen has a volumetric density of 0.07 kgL^{-1} at 1 bar while compressed hydrogen has a volumetric density of 0.039 kgL^{-1} at 700 bars. Thus by condensation, more hydrogen per volume can be stored than by compression. However, a large amount of energy is required for hydrogen liquefaction in insulated vacuum containers at -252 ^{o}C with about 40% loss in the energy content of hydrogen [3]. Consequently, this lowers the energy efficiency of the entire storage system. In addition, the necessity for hydrogen boil-off (through heat leakage) due to its very-low boiling point (-252.87 ^{o}C) poses a safety concern and limits the storage life.

The third and most promising alternative for storing hydrogen is in a metal matrix at moderate temperatures and pressures because some metals react reversibly with hydrogen to form stable metallic hydrides [4]. Light metal hydrides offer the greatest storage potential in terms of volumetric and gravimetric hydrogen density. In addition, metal hydride storage tanks are more compact and safer than compressed or liquid hydrogen tanks. Under pressure, bulk metal powders in a storage tank absorb hydrogen by exothermic reaction. The combination of high gravimetric storage capacity, good thermodynamics and kinetics are essential requirements for the realization of a hydrogen based economy for mobile applications.

The idea is to be able to use the waste heat from a proton exchange membrane/polymer electrolyte membrane (PEM) fuel cell at 85 ^{o}C to desorb hydrogen from metal hydride and re-absorb hydrogen into the metal.

Recently, complex hydrides have received considerable attention as potential hydrogen storage materials, with particular focus on light weight alkali and alkali-earth metals such as Li, Na and Ca cations which are ionically bonded to complex anions like alanates, amides and borohydrides [5-7]. Although some of these materials exhibit favourable thermodynamic properties, kinetic constraints and irreversibility of hydrogenation and dehydrogenation reactions significantly limit their application as mobile hydrogen storage systems. A pioneering work [5] demonstrated the reversibility of $NaAlH_4$ doped with Ti. Since then, several attempts have been made to investigate other complex hydrides. Furthermore, suitable tuning of thermodynamic properties by alloying and intermetallic compound formation has been applied in the past, with fair success reported in the cases of MgH_2 and ZrH_2 [8, 9]. However the resulting loss in hydrogen capacity posses a significant drawback to this approach.

A breakthrough was realized by the development of the Reactive Hydride Composites (RHC) [10-13]. In this novel approach, the exothermic formation of MgB_2 which occurs during the endothermic desorption of a combined system of two metal hydrides, considerably reduces the overall reaction enthalpy as well as desorption temperature, while still maintaining a high gravimetric storage capacity. A detailed description of the concept of Reactive Hydride Composites will be presented in section 2.5.

1.3 Scope of work

In this work, the hydrogen desorption and absorption mechanisms of the reactive hydride composites of $2NaBH_4 + MgH_2 \leftrightarrow 2NaH + MgB_2 + 4H_2$ and $2NaBH_4 + NaMgH_3 \leftrightarrow 3NaH + MgB_2 + 4H_2$ are investigated. The effects of temperature, pressure and composition on sorption kinetics and thermodynamics of these reactive hydride composites are carefully examined. Structural transformations and phase formation processes during absorption and desorption reactions are analysed in order to establish the reaction mechanism and origin of kinetic barriers limiting the complex reactions in these materials.

The $2NaBH_4 + MgH_2 \leftrightarrow 2NaH + MgB_2 + 4H_2$ system has a theoretical gravimetric capacity of 7.8 wt.% hydrogen, with an overall reaction enthalpy of 62 $kJmol^{-1}H_2$ resulting in an equilibrium pressure of 1 bar at 350°C. Although this system has been recently explored [14-16], the hydrogen sorption properties observed are not yet fully understood. Details on this hydride composite system are presented later in section 2.5 of this work.

The $2NaBH_4 + NaMgH_3 \leftrightarrow 3NaH + MgB_2 + 4H_2$ composite has a theoretical storage of 6.4 wt.% hydrogen and an estimated overall reaction enthalpy of 44 $kJmol^{-1}H_2$ in an equilibrium pressure of 1 bar at 350°C. This novel system is synthesized and analysed as part of this work, to shed light on the rate limiting reactions during hydrogen sorption in reactive hydride composites.

In the first step of this work, the process of hydrogen absorption in $2NaH + MgB_2 + 4H_2 \rightarrow 2NaBH_4 + MgH_2$ is explored. While in the second step, the process of hydrogen desorption in $2NaBH_4 + MgH_2 \rightarrow 2NaH + MgB_2 + 4H_2$ is

investigated. The third step examines the hydrogen absorption and desorption mechanism in $3NaH + MgB_2 + 4H_2 \leftrightarrow 2NaBH_4 + NaMgH_3$ system.

In tackling these tasks, volumetric analysis, differential scanning calorimetry, ex-situ and in-situ X-ray diffraction and transmission electron microscopy are used.

This work contributes to a better understanding of the complex reaction mechanism which is essential for the optimization of reactive hydride composites for efficient hydrogen energy storage applications.

2.0 Literature Review

This section presents the basic concepts of hydrogen storage in metals as well as a critical evaluation of previous investigations on the improvement of thermodynamic and kinetic properties of metal hydrides and reactive hydride composites for efficient hydrogen storage applications.

2.1 Chemical Storage of Hydrogen in Metals

Some metals react readily with hydrogen to form metal hydrides as expressed by the following reaction;

$$M\,(solid) + {}^{x}\!/_{2}\,H_2\,(gas) \rightarrow MH_x\,(solid) + Q \quad (2.1)$$

Where M represents the metal and Q is the heat energy released during the reaction. In most cases the reaction is exothermic. However, it is pertinent to note that the formation of a metal hydride is not a single process.

The metal-hydrogen reaction proceeds in a series of distinct steps: physisorption, dissociation, chemisorption, diffusion, phase transition, nucleation and growth as described by the one-dimensional Lennard-Jones potential energy diagram in figure 2.1 [4, 17].

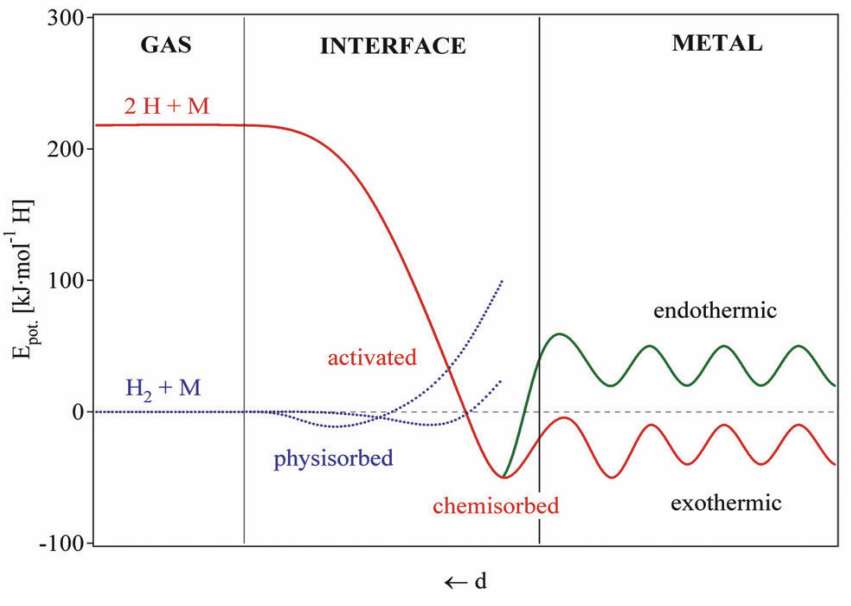

Figure 2.1: A schematic of the Lennard-Jones potential energy diagram of metal–hydrogen interaction (M represents Metal) [4].

A hydrogen molecule approaching the metal surface experiences a weak attractive van der Waals force resulting in the physisorbed state at about 0.2nm radii from the metal surface. [E_{phy}= - (2-10) kJmol^{-1} H_2] [4]. Closer to the metal surface, it overcomes the activation barrier for dissociation, depending on the surface elements involved, by electron sharing with the metal atom at the surface to form the chemisorbed state. [E_{chem}= - (10-100) kJmol^{-1} H_2] [4]. Through an activated process, the chemisorbed hydrogen (atomic hydrogen) jumps into the metal subsurface layer and diffuses onto low energy interstitial sites in the bulk metal lattice and subsequently dissolves exothermically to form solid solution α-phase, with a small hydrogen to metal ratio (H/M<0.1).

The pressure composition isotherm in figure 2.2, best describes the thermodynamics of metal hydride formation. As hydrogen concentration in the

metal increases (H/M>0.1), the hydrogen-hydrogen interaction becomes significant due to lattice expansion and at maximum solubility of hydrogen in the α-phase, the hydride phase (β) nucleates and grows. The concentration of hydrogen in the hydride phase is often H/M=1.

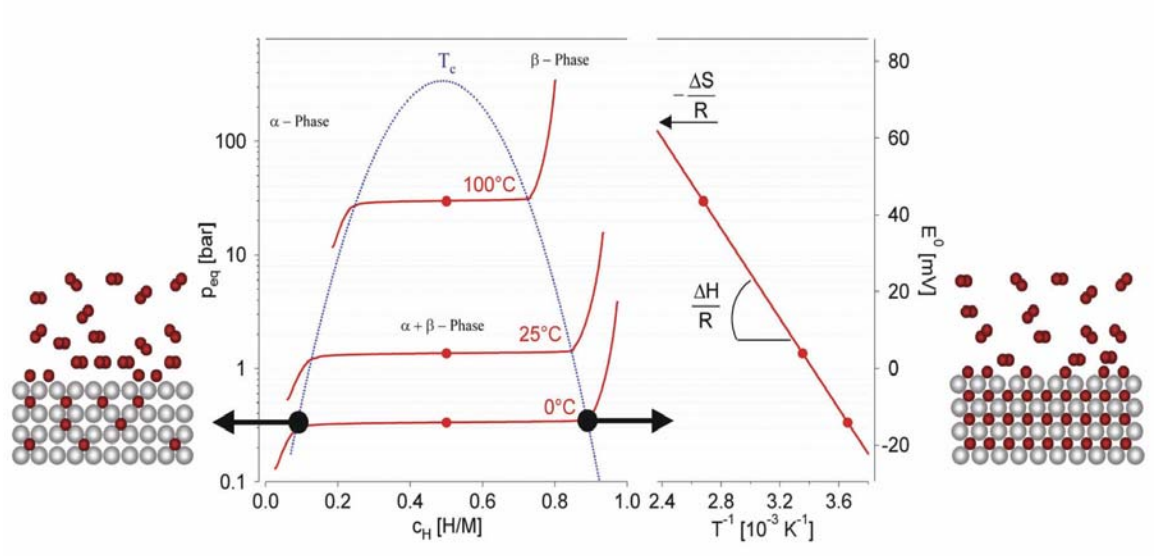

Figure 2.2: Left: Pressure-Composition-Isotherms (PCI) for a typical metal hydride. Right: Van't Hoff plot for a typical metal hydride derived from the measured pressures at equilibrium midpoints from the PCI [4].

The slope of the line (figure 2.2 right) is equal to the enthalpy of reaction divided by the gas constant and the intercept at 1/T= 0 K is equal to the entropy of reaction divided by the gas constant.

While the α- and β-phases coexist, a flat plateau is formed at a given pressure in the isotherm and the plateau length determines the amount of hydrogen that can be reversibly stored in the metal. At a critical temperature T_C, the two-phase region terminates and the transition from α-phase to β-phase is

then continuous. In the pure β-phase, the hydrogen pressure rises steeply with increasing hydrogen concentration. The operating temperature of the metal hydride is fixed by the plateau pressure in thermodynamic equilibrium and by the overall reaction kinetics. The temperature dependent plateau pressure is the equilibrium dissociation pressure of the hydride and is a measure of the stability of the hydride. The equilibrium/plateau pressure (P_{eq}) as a function of temperature (T) is related to changes in enthalpy (ΔH) and entropy (ΔS) by the Van't Hoff equation.

$$\ln\langle\frac{P_{eq}}{P^{\circ}}\rangle = \frac{\Delta H}{RT} - \frac{\Delta S}{R} \qquad (2.2)$$

Where R is the ideal gas constant and P^{o} is the reference pressure [4].

Hydrogen is stored in the interstitial sites of the host metal lattice as atoms. During absorption, the lattice expands often losing some of its symmetry. The coexistence of the non-expanded α- phase and anisotropically expanded β-phase, results in lattice defects and internal strain fields, which could consequently decrepitate brittle host metals. Hydrogen atoms vibrate about their equilibrium position with some local motions, and diffuse over a long-range. Based on electronic structure, the hydrogen proton attracts electrons in the host metal, resulting in low-energy electron bands which hybridize with the hydrogen band forming low-lying bands, about 6-8 eV below the Fermi level. Due to shifting of the Fermi level, different phase transitions could occur [2].

2.2 Essential criteria for hydrogen storage in metals

The key challenge for an ideal hydrogen storage system is to simultaneously meet all the criteria for on-board mobile applications. These target properties are based on some tunable parameters; structure (crystal form, interfaces and defects), thermo-chemistry (composition, phases and dopants) and reaction mechanism (distribution, diffusion path and transient species) [18]. The US Department of Energy [1] has set up targets for on-board hydrogen storage systems (table 2.1). These system and application-driven targets are based on achieving similar performance and cost levels as current carbonaceous fuel storage systems for automobiles.

Table 2.1: U.S. DOE hydrogen storage system performance targets [1].

Storage Parameter	**Units**	**2007**	**2010**	**2015**
Gravimetric				
Hydrogen density	kg H_2Kg^{-1} (system)	4.5 %	6.0 %	9.0 %
Volumetric				
Hydrogen density	kg H_2L^{-1} (system)	3.6 %	4.5 %	8.1%
Min/Max delivery temperature	^oC	-20/85	-30/85	-40/85
Min/Max H_2 delivery pressure	atm	8/100	4/100	3/100
System fuelling rate	kg H_2min^{-1}	0.5	1.5	2.0
Cycle life	cycles	500	1000	1500

2.2.1 Capacity

The gravimetric hydrogen storage capacity of a material is an important consideration in many applications, especially for non stationary applications. This is essential in automobiles to increase mileage and the range of distance covered prior to refueling. Most metallic elements can form stable hydrides with varying degree of chemical bonding; however, focus is on light metals within the first twenty elements in the periodic table because of their capability to absorb high amounts of hydrogen per unit weight. In the past decades several combinations of metallic compounds (figure 2.3) have been proposed, prepared and tested experimentally for their hydrogen storage properties [4]. Thermodynamic and kinetic constraints have been the main issues limiting their applicability.

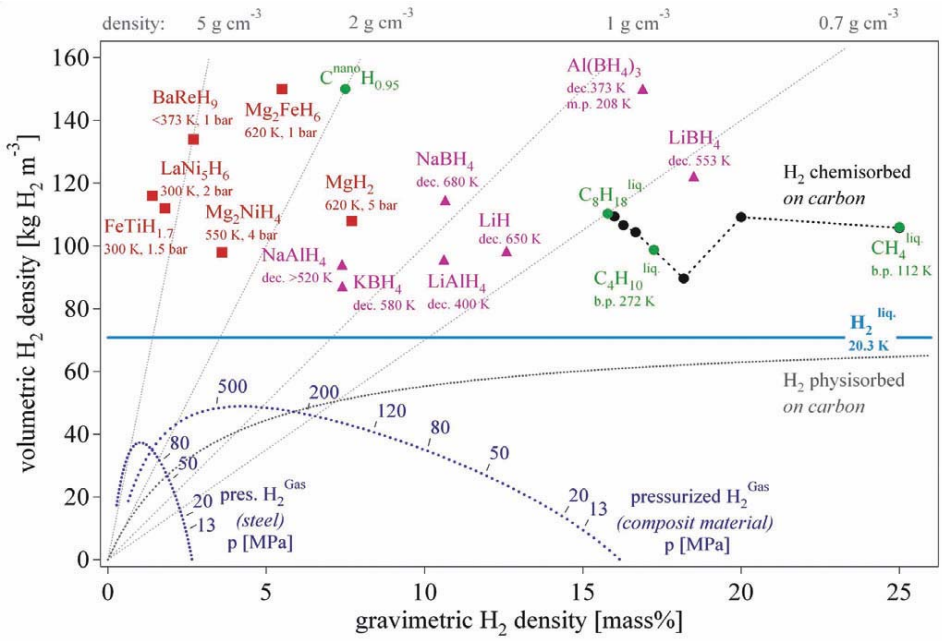

Figure 2.3: Volumetric and gravimetric hydrogen capacities of selected hydrides [4].

2.2.2 Thermodynamic Stability

The formation of metal hydrides results in the release of heat of absorption (ΔH), which directly influences the thermodynamic stability of the metal hydride. High thermodynamic stability means a larger ΔH and consequently higher absorption and desorption temperatures. For practical applications, a low sorption temperature in a range of 80-90 ºC corresponding to a heat of formation of 20-30 $kJmol^{-1}$ H_2 [2] at one bar, is desirable to decrease the amount of energy necessary to release hydrogen from a metal hydride and for efficient utilization of the waste heat at 85°C from the polymer electrolyte membrane (PEM) fuel cell.

The metal-hydrogen bonds in many candidate storage systems are either too weak or too strong for realistic applications. While physisorption involves weak bonding [E_{phy}= - (2-10) $kJmol^{-1}$ H_2] [4] and requires very low temperatures to achieve significant hydrogen capacity, chemisorption involves strong bonding [E_{chem}= - (10-100) $kJmol^{-1}$ H_2] [4] and requires high temperatures to dissociate stable bonds. Consequently, the need for optimization of tunable parameters like structure, thermo-chemistry and reaction mechanism is obvious in order to develop storage systems with ideal properties. In addition, adequate thermal conductivity is essential to prevent hydride re-decomposition by the exothermic heat of hydrogenation.

2.2.3 Sorption Kinetics

Fast reaction kinetics is essential for hydrogen absorption and desorption in a relatively short period of time. For a sustained supply of hydrogen to a PEM fuel

cell, fast hydrogen desorption and absorption rates are necessary. As described earlier in section 2.1, the hydriding reaction involves multi-step processes of physisorption, dissociation, chemisorption, diffusion, phase transition, nucleation and growth, while the reverse of these processes occurs during the dehydriding reaction. The rate of reaction is determined by the slowest reaction step. Hence, identification of the rate-limiting step is crucial for optimization. Overall sorption kinetics can be enhanced by structural modification and catalysis to lower activation barriers and increase gateways for hydrogen diffusion [2, 4, 18].

2.2.4 Reversibility

Good reversibility in hydrogen storage materials with negligible loss in capacity is essential for repeated cycles of hydrogen absorption and desorption in service conditions. This depends on various parameters like the microstructure at the start of reaction, cycling temperature and type of catalyst being used. Song et al. [19] synthesized magnesium hydrides with Cr_2O_3, Al_2O_3 and CeO_2 as catalysts. Compared to the first cycle, hydrogen sorption was less in the fifth cycle owing to particle-agglomeration during previous absorption and desorption cycles.

Misch-metals such as La, Ce, Pr and Nd, have been used to enhance cyclic stability [20]. However, the use of these metals as additives seriously affects the hydrogen storage capacity and rates of hydrogenation and dehydrogenation. Thermodynamic constraints due to hydride stability or kinetic restrictions owing to

rate-limiting reaction steps have been key drawbacks to practical reversibility and cyclic stability in hydrogen storage systems.

2.2.5 Cost

Cost is a vital issue for large scale commercial application of hydrogen storage and fuel cell technology. Material and system targets should be based on attaining comparable overall cost and performance levels to the current fossil energy or even better.

2.3 Thermodynamic modification of metal hydrides

Because of their advantages over other hydrogen storage methods, metal hydrides have been extensively investigated over the past decades. But up to now, experimental results show that thermodynamic and kinetic constraints of hydrogen sorption in metal hydrides make it difficult for any single material or combination of materials to simultaneously fulfill all the essential criteria for efficient hydrogen storage. Only low temperature intermetallic hydrides e.g. $LaNi_5H_6$ and $FeTiH_2$ which release hydrogen at 12 ºC and -8 ºC, respectively and 2 bars hydrogen pressure have met this criterion. However these materials store less than 2 wt. % of hydrogen because they contain heavy elements and thus do not meet the gravimetric density criterion for mobile applications [21].

Particular attention is now focused on light metal hydrides such as LiH and MgH_2, complex hydrides such as $NaBH_4$, $NaAlH_4$, $LiBH_4$, $LiAlH_4$ and $LiNH_2$ and

composites of different hydrides because of their higher storage capacities [4, 22, 23]. Binary hydrides can have good performance e.g. magnesium hydride (MgH_2), can reversibly store up to 7.6 wt. % of hydrogen. However, due to the high stability of the hydride, the equilibrium desorption temperature at 1 bar H_2 pressure is about 280 ºC, with a reaction enthalpy of 78 $kJmol^{-1}$ H_2 [24]. Tetrahydroborate $[BH_4]^-$ based complex hydrides have high storage capacity e.g. $LiBH_4$, possesses the highest theoretical gravimetric hydrogen density of 18 wt. %. However, this hydride desorbs only 13.5 wt. % H_2 above 400 ºC with a heat of decomposition of about 68.6 $kJmol^{-1}$ H_2 [25, 26]. Alanate complex hydrides based on tetrahydroaluminate $[AlH_4]^-$ e.g. $NaAlH_4$, has a hydrogen capacity of 7.4 wt. %. At moderate temperatures between 100 ºC and 150 ºC, this hydride is sluggishly reversible and decomposes in two steps forming intermediate compounds of Na_3AlH_6 and NaH respectively [5]. The reaction kinetics can be enhanced by doping with suitable titanium-based catalysts and it releases a total of 5.6 wt. % H_2. However, it is still unattractive for mobile applications owing to its low effective gravimetric capacity.

In contrast to the delocalized metallic bonds which typify transition metal hydrides, binary and complex metal hydrides are mostly characterized by covalent, polar-covalent or ionic bonds [27-29]. These chemical bonds are often strong and highly directional, resulting in high thermodynamic stability due to restricted atomic motion and large activation barriers. Consequentially, this leads to slow kinetics in hydrogen sorption and limits reversibility of sorption. The correlation between the stability of complex hydrides and the ionic character of

the metal species has been investigated [30]. Complex hydrides with lower cation Pauling-electronegativity are less stable and hence more reactive. In addition, the stability of complex hydrides can be altered by partial substitution of either the cation or the boron and aluminium atoms in tetrahydroborates and tetrahydroaluminates respectively [31, 32]. Both Shang et al [33] and Berube et al [34] have reported that the introduction of considerable levels of structural defects and phase change by mechanical milling results in thermodynamic modifications. In both amorphous (defected) and crystalline microstructures, hydrogen atoms usually occupy similar interstitial sites, however owing to varied lattice distortion in the defected structure, the binding energies of different interstitial sites vary.

In classical metal hydrides, a modification of the lattice constant by alloying with further elements enables a continuous modification of reaction enthalpy, ΔH. Such a mechanism is not however possible for the ionically or covalently bonded hydrides. Figure 2.4 shows an enthalpy diagram illustrating destabilization by alloy formation during dehydrogenation of a metal hydride. Prior to destabilization, the hydride AH_2 releases hydrogen to form A + H_2, with a large reaction enthalpy and at a high equilibrium desorption temperature. However, when the hydride AH_2 is alloyed with element B, an alloy AB_x is exothermically formed during endothermic dehydrogenation from AH_2 + xB, resulting in a reduction in the enthalpy of reaction and lower equilibrium desorption temperature. Therefore, with alloying element B, the system cycles between the absorbed state (AH_2), and the stabilized state (AB_x) instead of pure A.

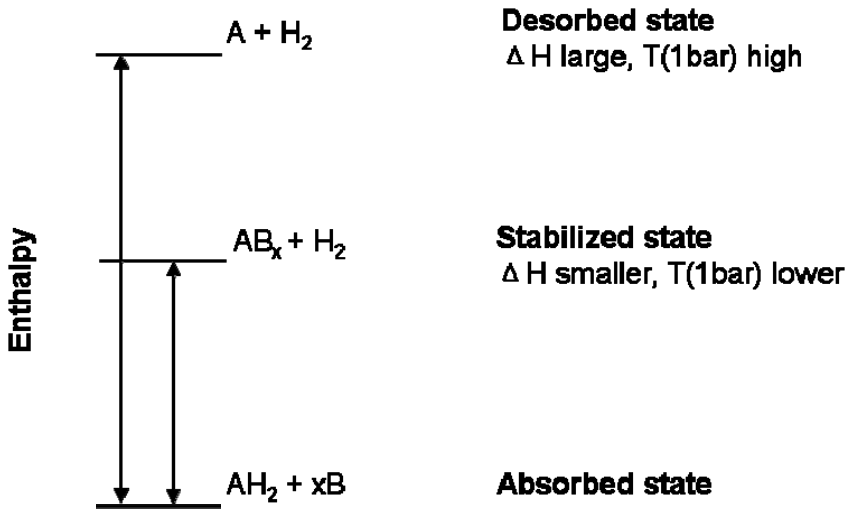

Figure 2.4: A schematic enthalpy diagram illustrating destabilization by alloy formation [35].

Several attempts have been made to thermodynamically modify the properties of metal hydrides by hydride destabilization/alloying with a view of reducing the reaction enthalpy as well as the sorption temperature and consequently increasing the equilibrium hydrogen pressure.

A prominent example of such efforts is the pioneering work of Reilly and Wiswall [8] using $MgCu_2$ to destabilize MgH_2 by alloying at 240 ^oC under an equilibrium pressure of 1 bar, with Mg_2Cu forming upon dehydrogenation according to the equation below:

$$^3/_2MgH_2 + ½MgCu_2 \rightarrow Mg_2Cu + {}^3/_2H_2 \quad (2.3)$$

The resulting temperature is ~40 ^{o}C, less than the equilibrium temperature for pure MgH_2:

$MgH_2 \rightarrow Mg + H_2$ [T (1 bar) = 280 ^{o}C] (2.4)

This strategy suggests the possibility of an additional step in which MgH_2 is destabilized by Cu in which case $MgH_2 + MgCu_2$ followed by Mg_2Cu are formed sequentially in two dehydrogenation steps. Similarly, the MgH_2/Al system forms a variety of Mg/Al alloys upon desorption [36]. The equilibrium pressure was measured to be three times higher than for pure MgH_2.

Furthermore, Veleckis [37] demonstrated that Li in Li/Al and Li/Pb alloys could be reversibly titrated with hydrogen to produce LiH+Al or Pb. In most intermetallic systems, the bonding is relatively weak and destabilization is therefore modest. However, in more covalently bound compounds, there can be stronger bonds resulting in larger destabilization. For instance, LiH and MgH_2 have been destabilized with silicon and in the LiH/Si system [38] resulting in a number of stoichiometric Li silicides that give isotherms with multiple equilibrium hydrogen pressures.

The hydrogen sorption properties of Mg-Ni-Si system have been explored by reacting MgH_2 with elemental Ni and Si [22]. Hydrogen interaction with the new ternary phase of Mg-Ni-Si was not observed. Instead it decomposed into two binary phases of Mg_2Ni and Mg_2Si. In addition, the reaction between Mg_2Ni yielded a composite compound of Mg_2NiH_4 and $Mg_2Si.Mg_2Si$ with a heat of formation of 79 kJmol^{-1} H_2 [22] and that could be a promising hydrogen storage material. However, due to its close-packed crystal structure, hydrogen sorption

kinetics are relatively poor especially in moderate temperature and pressure conditions (<300 ^{o}C and < 50 bars H_2). Further attempts to modify the crystal structure by partial substitution of Si via ternary alloying found a tendency for decomposition during cycling, hence elements with stronger affinity to both Mg and Si, like Li, C, Al, Ca etc were used. So far, hydride phases formed have either shown high thermal stability or irreversibility under moderate conditions.

The addition of a non-hydriding additive to a metal hydride as alloying specie inevitably reduces the total hydrogen capacity. However, the loss in capacity can be minimized if the alloying specie is a hydride. For example, if only high-capacity hydrides are chosen as additives, which react with each other under dehydrogenation in a reversible manner, a reduction in reaction enthalpy can be achieved without significant loss of hydrogen capacity. These are known as Reactive Hydride Composites [11, 13].

2.4 Kinetic modification of metal hydrides

The kinetics of hydrogen sorption in metal hydrides is determined by the slowest reaction step. The rate-limiting steps for hydrogen sorption in milled and catalysed MgH_2 were investigated by Barkhordarian et al [39]. According to their analysis, the hydrogenation reaction is diffusion controlled, while the dehydrogenation reaction is limited by surface reaction. According to Holtz [40], diffusion is not initially the rate limiting step during hydrogenation because no reaction has occurred and active sites are adequately available. Instead, the

velocity of the metal-hydride interface determines the reaction kinetics in the very early stages and assuming fast hydrogen diffusion, the interface grows with time. However, as the reaction proceeds, the hydride phase grows, forming a virtually impervious layer. As a result, the growth of the metal-hydride interface decreases with time and the diffusion of hydrogen through the formed hydride layer becomes the rate limiting step [41]. Furthermore, exposure of the material to oxygen reduces the rate of hydrogenation because of the stable oxide layer that is formed which also acts as a barrier to hydrogen [42].

For magnesium-based hydrides, Andreasen et al. [43] suggested that there is a correlation between differences in apparent activation energies and the presence of a surface layer of magnesium oxide which inhibits hydrogen diffusion.

Microstructure is one of the critical factors influencing the kinetics of hydrogen sorption in metal hydrides. Nanoscale grain and crystallite sizes reduce diffusion path lengths and the time for hydrogenation and dehydrogenation reactions [44-46]. Increased material surface area enhances the dissociation of molecular hydrogen into atomic hydrogen and permits easy diffusion of hydrogen into the bulk for subsequent chemical bonding with the host metal. Due to a lower packing density of atoms, diffusion of hydrogen is faster along grain boundaries, which also act as favourable nucleation sites for sorption reaction. Improved hydrogen sorption kinetics has been achieved using nanostructured materials [42, 47, 48] achieved by ball-milling. According to Suryanarayana [49], a continuous refinement of the microstructure occurs during ball milling, resulting in a very homogenous composition. In addition to the formation of nanostructures

and increased surface area, ball-milling creates surface and internal defects in the material. These lattice defects and micro-strains provide sites with low activation energy and lessen the hysteresis in hydrogen sorption cycles [50].

Suitable catalysis is another important factor in the optimization of sorption kinetics in metal hydride systems. Catalyst dispersions within the material matrix could form nucleation sites for absorption and desorption with lower surface and interfacial energies, thereby enhancing surface reactivity and facilitating fast dissociation and recombination of hydrogen molecules. Numerous efforts have been made to improve surface reaction kinetics in hydrogen storage materials using catalysts. They include the use of hydride-forming elements such as Ce, Nb and Ti [51] as well as non-hydride-forming elements as Fe, Co and Cr [52, 53].

The addition of 3d transition metals or their oxides as catalysts have been found to significantly improve sorption kinetics in nanocrystalline magnesium-based hydrides [54-58]. Due to better catalytic behaviour exhibited by oxides, Oelerich et al [54] and Barkhordarian et al [57, 58], independently investigated the influence of different metal and transition metal oxides on the sorption kinetics of magnesium based hydrides. Barkhordarian et al [59] identified some factors influencing the catalytic behaviour of transition-metal oxides in Mg-based hydrides. These factors are:

(i) *The density of structural defects in the transition-metal oxide*. Fromme [60] had reported that transition-metal ions on the oxide surface and in the bulk could experience a crystal field effect because of missing

oxygen ions at the surface. This result in electronic 3d splitting of the ions and likely responsible for the catalytic behaviour of transition metal oxides in hydrogen sorption reactions. Experimental investigations by Barkhordarian et al [59] on the effect of milling time on the desorption kinetics of catalysed MgH_2 shows that a higher amount of structural defects introduced by longer ball milling time enhances the catalytic activity of transition-metal oxides.

(ii) *Catalyst-support interaction and thermodynamic stability of the transition metal oxide*. Pure metal catalysts films are usually supported on ceramic substrates mainly oxides. Contrary to earlier supposition of their inertness, study has shown that these supports are catalytically active and the interfacial interaction between the metal catalyst and oxide support as well as the morphology and electronic structure of the oxide support significantly influences the catalytic activity of transition-metal oxides [61, 62]. Hammer [63] also detected a positive metal-support interaction in the MgO/Pd system, where the interaction of Pd with MgO resulted in an increased catalytic activity. From these investigations, a transition metal oxide with low thermodynamic stability favourably for interacts chemically with the oxide support. However, due to the poor catalytic efficiency of most pure transition metals, their chemical stability should be considerably high to avert a total reduction of the transition-metal compound by either magnesium or it hydride.

(iii) *Valence state of the transition-metal ions in the catalyst*. The variable oxidation states of the metal in a transition metal-containing compound is essential for an effective catalytic effect [54]. Further investigations by Barkhordarian et al [59] using different niobium oxides (Nb_2O_5, NbO_2 and NbO) indicates speed of reaction increases in the order $NbO < NbO_2 < Nb_2O_5$. The capability of transition metal ions to exhibit multiple valence states enables them to easily dissociate hydrogen molecules, thereby creating pathways for both hydride formation and hydride decomposition.

(iv) *Hydrogen affinity to transition-metal*. Since hydrogen atoms readily react with transition metal ions, an enhanced catalytic effect can result from a stronger transition metal-hydrogen bond. To verify this assumption, Barkhordarian et al [59] found Nb_2O_5 to be catalytically more effective than Ta_2O_5. Considering that both oxides have similar valence state and thermodynamic stability, the stronger interaction hydrogen atoms with niobium is the main reason for the faster sorption kinetics observed with Nb_2O_5.

Despite all attempts to improve sorption properties in light metal hydrides, the absorption and desorption temperatures of investigated systems are still higher than estimated from thermodynamics and therefore still limited by kinetic constraints. Further thermodynamic and/or kinetic modifications are essential to appreciably overcome these constraints associated with absorption and desorption reactions in metal hydrides.

2.5 Reactive hydride composites

Due to their high gravimetric storage densities, tetrahydroborates [e.g. $LiBH_4$ (18.5wt % H_2), $NaBH_4$ (10.8 wt % H_2), and $Ca(BH_4)_2$) (11.6wt % H_2)], have been materials of special interest for hydrogen storage applications. However, they suffer drawbacks of high desorption temperature, slow kinetics and limited reversibility.

The room temperature phase of $LiBH_4$ is orthorhombic. At a higher temperature of about 108 ^oC, the compound transforms to a hexagonal phase [64]. Further heating results in the melting of the material at about 275 ^oC [64, 65]. Pure $LiBH_4$ decomposes to LiH and B (see equation below) above 400 ^0C releasing 13.5wt % hydrogen with a heat of decomposition of 68.6 kJ/mol H_2 [2, 26].

$$2LiBH_4 \rightarrow LiH + B + {}^3/_2H_2 \quad (2.5)$$

Despite the high driving force, absorption (reverse reaction) is difficult at low temperature and pressure conditions. Orimo et al. reported that the re-hydrogenation reaction of LiH and B proceeded to form $LiBH_4$ at 600 ^0C under 350 bars of H_2 pressures [25].

Meanwhile, MgH_2 with a tetragonal crystal structure also has a high hydrogen storage capacity of 7.6wt% and shows good potential as a candidate material for hydrogen storage applications. It undergoes fast reaction kinetics when prepared by mechanical milling and suitably doped with catalysts [57]. The sorption kinetics of MgH_2 have been highly investigated [39, 57, 58]. Submicron and

nanostructured magnesium powder in the presence of a suitable catalyst, e.g., Nb_2O_5 showed reversible storage of hydrogen up to 7.0 wt% within a few minutes [24, 39, 57, 58]. In addition, the long-term stability of MgH_2 (up to 2000 cycles) has been proven [24]. However, due to its fairly stable magnesium-hydrogen bonds, decomposition of this hydride at moderate temperatures is thermodynamically unfeasible. The major disadvantage is its high desorption temperature, which is about 280 ºC at 1 bar hydrogen pressure, as also reflected in the high enthalpy of hydride formation: 78 $kJmol^{-1}$ H_2 [24]. For both materials, their reaction temperatures far exceed the target operating temperature of 85 ºC (from the waste heat of a PEM fuel cell) set for mobile applications.

In attempts to overcome these drawbacks, independent investigations by Barkhordarian et al [10, 11] and Vajo et al [12, 13] led to the development of the Reactive Hydride Composites as schematically illustrated in figure 2.5. The approach shows that the combination of two different metal hydrides results in a new composite hydride with lower reaction enthalpy and lower dehydrogenation temperature than the individual hydrides.

The principle of the Reactive Hydride Composites is that during endothermic desorption of a composite hydride system, the exothermic formation of MgB_2 proceeds simultaneously and stabilizes the desorbed state, resulting in a significant decrease in overall reaction enthalpy and desorption temperature. Examples of Reactive Hydride Composites are; $2LiBH_4 + MgH_2$, $2NaBH_4 + MgH_2$ and $Ca(BH_4)_2 + MgH_2$ [10, 11].

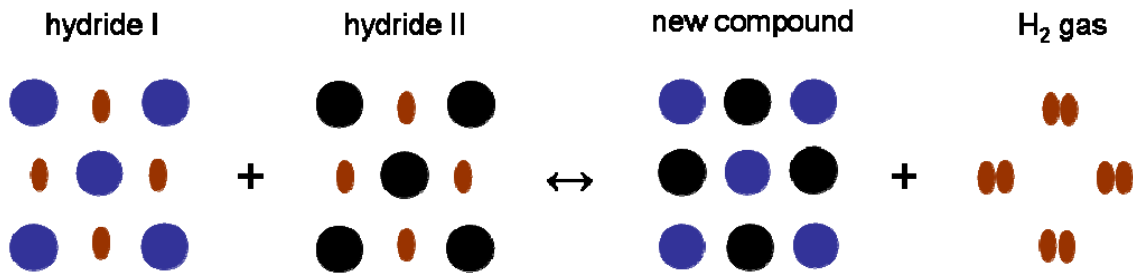

Figure 2.5: Schematic illustration of the concept of Reactive Hydride Composites.

The investigations by Vajo et al and Barkhordarian et al reveal that the addition of MgH_2 to $LiBH_4$ results in a significant change in sorption properties. They demonstrated that the composite of $2LiBH_4 + MgH_2$ can be reversibly destabilized releasing 11.5 wt. % H_2 according to the following equation:

$$2LiBH_4 + MgH_2 \leftrightarrow 2LiH + MgB_2 + 4H_2 \quad (2.6)$$

The estimated reaction enthalpy and equilibrium temperature at 1 bar hydrogen pressure are 46 $kJmol^{-1}$ H_2 and 170 ^oC respectively [11, 13]. Thus ideally the combination of $LiBH_4$ and MgH_2 decreases T (1 bar) to 170 ^oC compared to 400 ^oC and 280 ^oC for $LiBH_4$ and MgH_2 respectively [66]. Hence, both $LiBH_4$ and MgH_2 are destabilized in this composite system. However, as shown in figure 2.6, when heated from room temperature to 400 ºC under 5 bar hydrogen pressure, this reactive hydride composite appears to exhibit a two-step dehydrogenation process, with an intermediate incubation period [67]. The temperature at which desorption begins is much higher than predicted from enthalpy calculations. The plateau may be as a result of restricted nucleation of MgB_2 due to low atomic mobility or long diffusion path lengths for hydrogen.

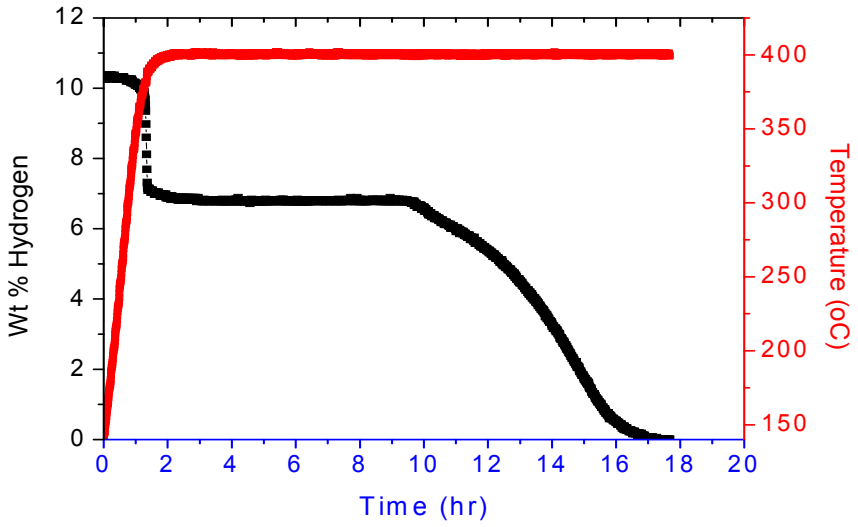

Figure 2.6: Desorption kinetics of as-milled $2LiBH_4 + MgH_2$ composite from room temperature to 400 ºC under 5 bar H_2 and [67].

Furthermore, Bösenberg et al [67] carried out simultaneously, differential scanning calorimetry (DSC), thermo-gravimetric analysis (TGA) and mass spectrometry (MS) of the dehydrogenation of as-milled $2LiBH_4 + MgH_2$ (see figure 2.7). Their analysis reveal four separate thermal events as follows; (A) phase transformation of $LiBH_4$; (B) melting of $LiBH_4$; (C) + (D) desorption of MgH_2 and $LiBH_4$. The significant release of hydrogen and the corresponding weight loss associated with peaks C and D indicate a two-step dehydrogenation phenomenon, as illustrated by the following the equation:

$$2LiBH_4 + MgH_2 \rightarrow Mg + 2LiBH_4 + H_2 \rightarrow MgB_2 + 2LiH + 4H_2 \quad (2.7)$$

However, absorption does proceed in a single step from $2LiH + MgB_2$ forming $2LiBH_4 + MgH_2$ under 50 bars hydrogen pressure and between 250-300 ^oC [67].

Barkhordarian et al [11] also performed in situ XRD analysis of the desorption of $2LiBH_4 + MgH_2$ doped with titanium isopropoxide as catalyst under 5 bar hydrogen pressure. According to their results shown in figure 2.8, A and B correspond to the polymorphic transformation and the melting of $LiBH_4$ respectively. From C, the desorption of MgH_2 to Mg and subsequent interaction with desorbed $LiBH_4$ takes place leading to the formation of MgB_2 and LiH. Again, sorption temperature is still higher than expected according to the principle of reactive hydride composites.

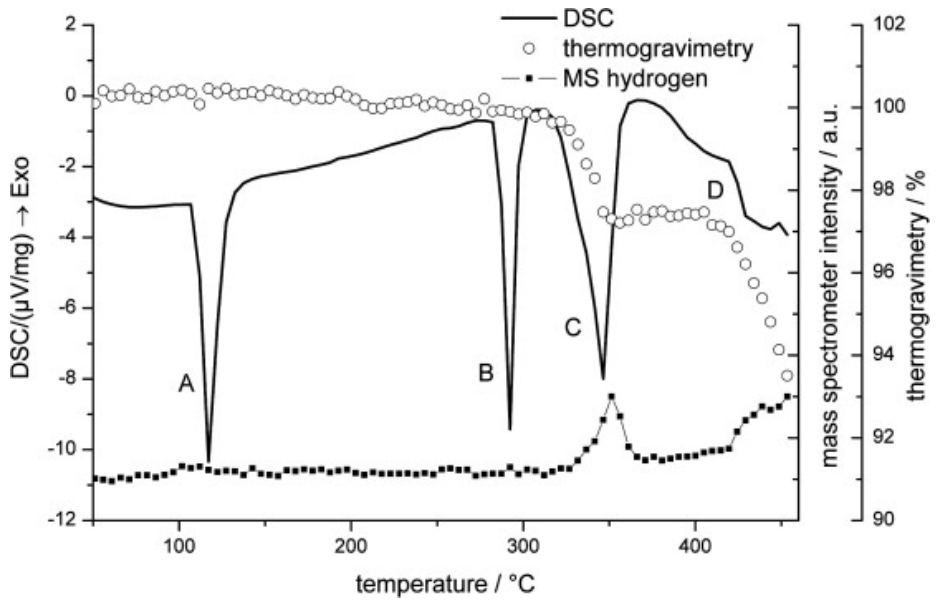

Figure 2.7: Simultaneous DSC, TGA and mass spectrometry of $2LiBH_4 + MgH_2$ reactive hydride composite, desorbed from room temperature to 465 °C at a heating rate of 5 K min^{-1} under an argon flow rate of 200 ml min^{-1} [67].

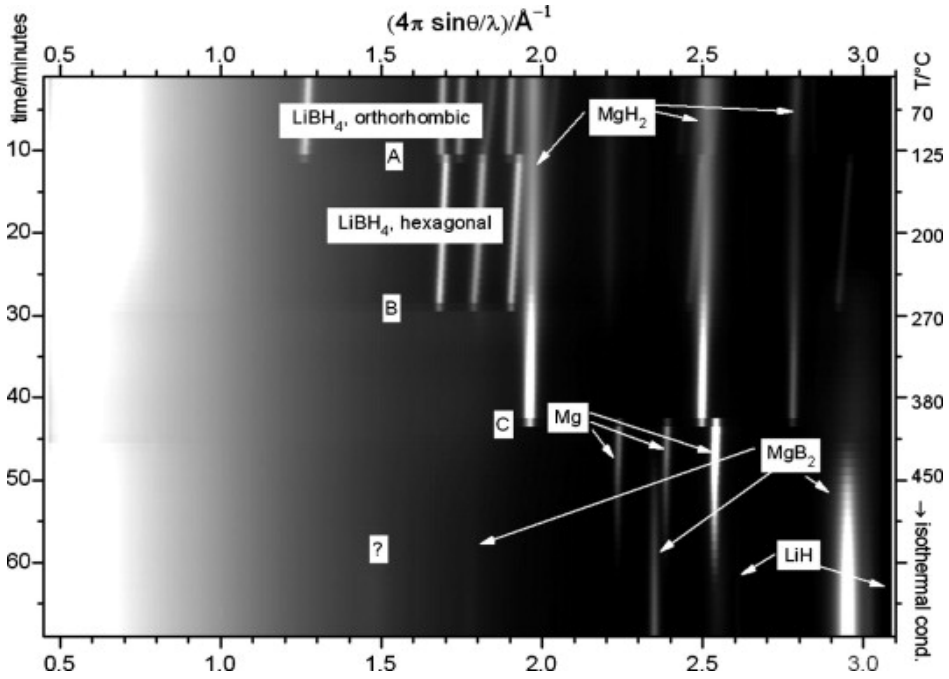

Figure 2.8: In-situ X-ray diffraction analysis of $2LiBH_4 + MgH_2$ composite, doped with 5 mol % titanium isopropoxide desorbed under 5 bars hydrogen from room temperature to 450 ºC at a heating rate of 5 ºCmin^{-1} [11].

Another complex tetrahydroborate, $NaBH_4$ which has a cubic lattice structure has a high thermal stability and decomposes at temperatures between 550 - 650 ^oC [2, 68] under 1 bar H_2 pressure with a reaction enthalpy of 88.2 kJmol^{-1} H_2 [69, 70]. These properties are not good enough for practical hydrogen storage applications. Lower sorption temperature have also been achieved by the principle of reactive hydride composites [10, 11] and the composite hydride of $2NaBH_4 + MgH_2$ is reversibly destabilized according to the following reaction:

$$2NaBH_4 + MgH_2 \leftrightarrow 2NaH + MgB_2 + 4H_2 \quad (2.8)$$

The resulting storage capacity is 7.8 wt. % H_2 at an equilibrium temperature of 350 ^oC with a reaction enthalpy of 62 $kJmol^{-1}H_2$.

Furthermore, DSC investigations on the sorption properties of different compositions of MgH_2 + $NaBH_4$ nano composites by Czujko et al [16] indicate two endothermic peaks at ~ 330 ^oC and ~ 405 ^oC in the MgH_2 + 20 wt.% $NaBH_4$ composite (see figure 2.9). These peaks are most likely related to desorption of MgH_2 and $NaBH_4$ respectively. However, the single endothermic desorption peak obtained in MgH_2 + 2 wt.% $NaBH_4$ at ~438 °C and in MgH_2 + 10 wt.% $NaBH_4$ at ~ 338 °C shows that both hydrides are simultaneously destabilized during desorption.

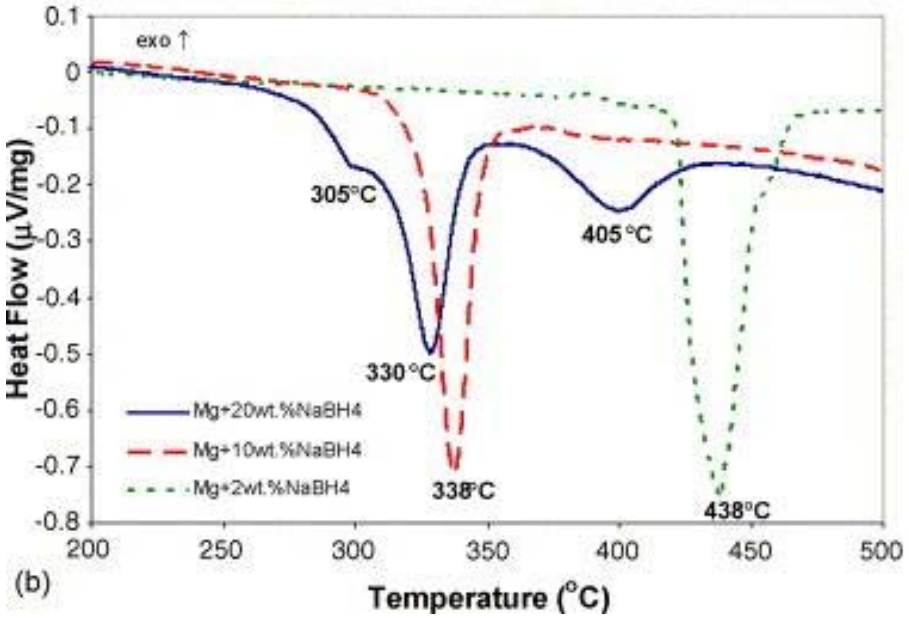

Figure 2.9: DSC spectra of different compositions of reactively milled MgH_2 + $NaBH_4$ composite hydrides [16].

The composite system of $Ca(BH_4)_2$ + MgH_2 can also be reversibly destabilized through the principle of reactive hydride composites according to the following equation:

$$Ca(BH_4)_2 + MgH_2 \leftrightarrow CaH_2 + MgB_2 + 4H_2 \quad (2.9)$$

An effective storage capacity of 8.3 wt. % H_2 is realizable at <160 ^oC [10, 11]. To test the reversibility of CaH_2 + MgB_2 composite, Barkhordarian et al [11] hydrogenated a molar ratio of the sample at two different temperatures and pressures. At 300 ^oC and 200 bars hydrogen pressure, a hydrogen absorption capacity of 4.7 wt.% was attained. At 400 ^oC and 350 bars hydrogen pressure, up 7.0 wt. % hydrogen was absorbed by the composite. Furthermore, In-situ X-ray diffraction studies by Barkhordarian et al [71], reveal the formation of $Ca(BH_4)_2$ and MgH_2.

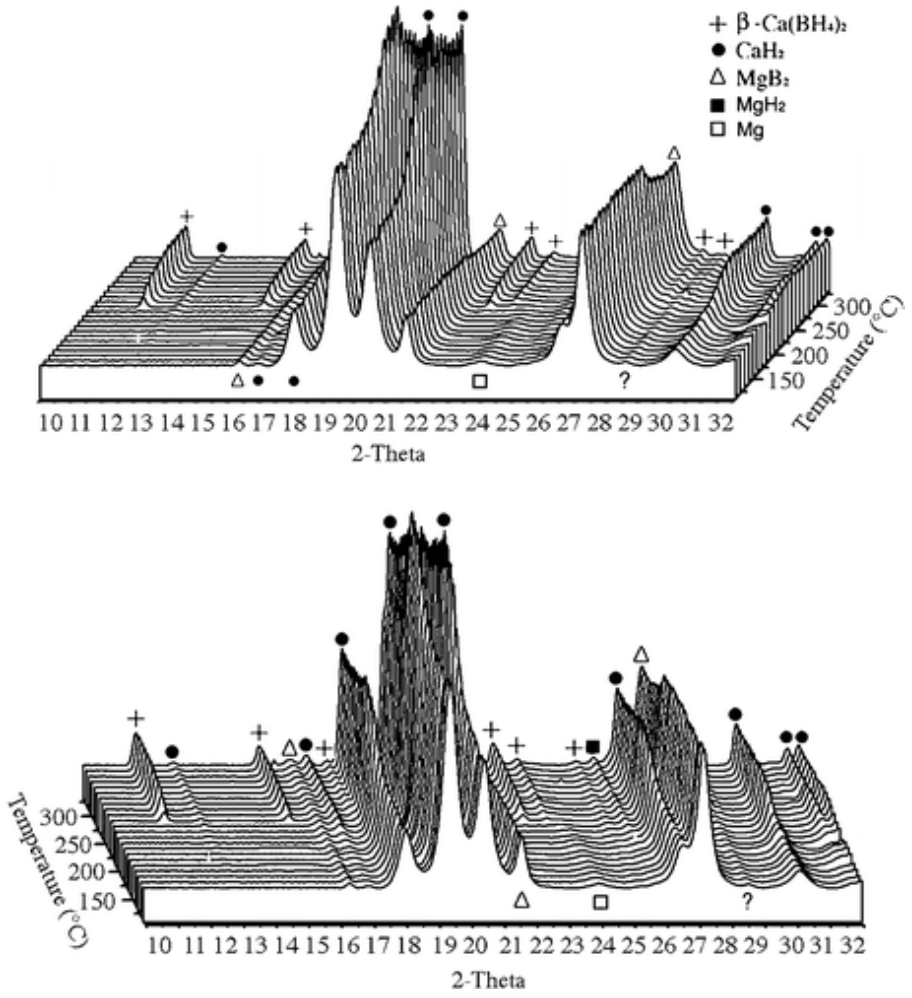

Figure 2.10: In situ SR-PXD patterns of CaH_2+MgB_2 composite, absorbed under 125 bar hydrogen at a heating rate of 5 $Kmin^{-1}$ [71].

A further investigation on reversible hydrogen storage in $TiCl_3$-catalyzed $Ca(BH_4)_2$ at ~400 ^oC and 90 bars H_2 have been reported [72]. Comparatively, $Ca(BH_4)_2$ is a fairly stable tetrahydroborate and the $Ca(BH_4)_2$ + MgH_2 composite is a good candidate for hydrogen storage applications due to its low sorption temperature.

MgB_2 has a proven kinetic advantage over elemental boron in the formation of tetrahydroborates, since the former provides the benefit of lower

thermodynamic driving force, which consequently reduces the sorption temperature. Further investigation into the likely origin of the kinetic effect of MgB_2 [11] suggests that less energy is required to detach a boron atom from the sp^2 layered structure of MgB_2 than from icosahedra units in pure boron. Given that the reactivity of boron largely depends on its atomic structure, it is reasonable to assume that the type of boron bonding (B-B, B-H, Mg-B-H), the bond length and the coordination number have significant influences on the reactivity of boron and its compounds.

Reactive hydride composites should indeed present a promising potential for hydrogen storage applications. However, hydrogen sorption only occurs at much higher temperatures than expected and the reactions are limited by slow reaction kinetics, especially at lower (desirable) temperatures. The thermodynamics and sorption kinetics of these composite hydrides are still being investigated and up to now, no comprehensive conclusions on their reaction mechanism have been made.

2.6 Microstructural characterisation of metal hydrides

Microstructural characterisation provides an important tool for further understanding the relationship between structure, morphology, composition and the two principal limitations of thermodynamics and kinetics associated with metal hydride systems. X-ray diffraction has been the most broadly used microstructural characterisation technique for examining metal hydrides [73].

However, electron microscopy can also provide relevant microstructural information on grain size, crystal orientation, phase distribution as well as other information not obtainable by other characterization techniques, and has been successfully used to characterize metal hydrides [74-85].

The following section intends to give an overview of what is currently understood in microstructural examination of bulk metal hydrides, especially the magnesium-based hydride systems using various electron microscopy techniques.

Transmission electron microscopy (TEM) studies have been carried out on both catalysed and non-catalysed MgH_2 [76-82, 86], and on complex metal hydrides such as $NaAlH_4$ [83, 84], $LiAlH_4$ [85] and $LiBH_4$ [87, 88]. Scanning electron microscopy (SEM) has in some cases been used to examine metal hydride systems [80, 81, 83, 85]. However, information from this technique has been limited to surface morphology at a micrometer scale, due to the lower magnification and resolution obtainable from scanning electron microscopes.

One of the main issues with TEM examination of MgH_2 has been its instability under a strong electron beam [76, 77]. Early investigation on the structure and morphology of electron beam-induced-decomposition of MgH_2 [76] showed the existence of super-lattice reflections due to the ordering of hydrogen vacancies, and the subsequent formation of a Mg-MgH_2 lamellar structure (~ 300nm wide) as decomposition proceeded owing to an increasing number of hydrogen vacancies. According to the report, Kikuchi features disappear with increasing beam intensity and the intensity of diffraction spots from MgH_2 crystal also decreases.

Sample preparation for TEM investigation has been another issue of extreme difficulty due the high sensitivity of metal hydrides to air. Mixing of powder samples with a suitable water-insoluble solvent like hexane and toluene in an inert atmosphere such as in a glove box, has been a widely adopted technique aimed at overcoming this problem [82, 83]. In addition, the three-dimensional shape of these powder particles partly limits examination to particle edges which are thinner relative to the centre. However, Kim et al [81] were able to prepare uniformly thin samples for TEM examination by Focused Ion Beam (FIB) milling, using an airlock sample loading chamber which prevented the oxidation of samples. This provided a wider area for observation in the microscope.

In this work, FIB milling was not used for sample preparation due to time constraints in developing a specialized airlock loading chamber for samples as well as cost constraints in acquiring a dedicated microscope for this purpose.

Their study on the microstructural evolution of 1 mol % NbF_5-doped MgH_2 by high angle annular dark field (HAADF) imaging reveal β-MgH_2 as the dominant crystalline phase and a surface layer of Nb film on MgH_2 particles which facilitates hydrogen uptake and release during absorption and desorption respectively. MgH_2 crystallite sizes of 20-40nm were measured and give fair agreement with earlier results of ~20nm obtained by X-ray diffraction analysis. High resolution electron microscopy (HREM) on the same material also indicate that the cubic MgF_2 phase formed during ball milling was influential on the onset activation of dehydrogenation of MgH_2, owing to its high affinity for hydrogen. Indexing of the selected area electron diffraction (SAED) pattern revealed the

presence of (022) β-$NbH_{0.89}$ which, according to the authors, helps to impede the growth of MgH_2 grains, thereby sustaining the catalytic role of dopant during sorption cycles.

Earlier, Yavari et al [73] using time resolved X-ray diffraction, disclosed the existence of MgH_2/NbH and MgH_2/Nb nano interfaces which can promote fast hydrogen diffusion. Furthermore, they described the action of Nb in the hydrogenation of both Mg and Nb as thermo-catalytic and the resulting fast kinetic effect as due to the high interfacial energy at the nano-interfaces.

In a TEM study on the catalytic role of Nb_2O_5 on the sorption properties of MgH_2, Porcu et al [82] showed that HAADF imaging is capable of locating dispersed oxide phases of Nb_2O_5 within MgH_2 by z-contrast, with fragments of additive embedded and finely distributed along grain boundaries thus providing fast gateways for hydrogen diffusion during desorption and absorption reactions. They also pointed out the partial reduction of Nb_2O_5 to Nb_2O and the formation of MgO phase. The interaction of MgO with unreduced Nb_2O_5 led to the formation of a mixed oxide of $MgNb_2O_{3.67}$ [79], which is known to facilitate proton diffusion [89, 90].

Similarly, Hanada et al [80], reported a homogeneous distribution of Nb_2O_5 particles in bulk MgH_2. From their study, Mg crystals grew to about 500 nm in diameter during sorption up to 200 ^oC. Although their TEM investigation did not detect additive particles within the MgH_2 matrix, it is believed that such uniform distribution of the catalyst particles may lead to fast sorption kinetics in MgH_2.

Microanalytical techniques such as energy dispersive X-ray spectroscopy (EDXS) and electron energy loss spectroscopy (EELS) have also been used to obtain quantitative compositional information on samples during analysis [80-83]. Whereas EDXS is capable of detecting heavier elements such as Na, Mg and Ca, lighter and low-z atoms such as Li and B are more easily detected by EELS.

It has so far been demonstrated that electron microscopy techniques can provide vital information about orientation and distribution of various phases within the matrix of bulk metal hydrides, especially in catalyzed systems, since catalysts are known to significantly influence sorption kinetics in light metal hydrides.

In addition to the basic reaction steps of hydrogen dissociation, diffusion and the nucleation and growth of the hydride phase, it is also necessary to consider the diffusion of metal atoms and its effect on overall sorption properties.

It is expected that by using transmission and high resolution electron microscopy and other micro-analytical techniques, an improved understanding of reaction mechanisms, phase interactions, and the origin of kinetic constraints in the reactive hydride composite of $2NaBH_4 + MgH_2$ can be achieved.

3.0 Experimental – Materials and Methods

In this chapter, a concise overview of the material preparation and measurement techniques is presented. Owing to variations in experimental conditions, the exact investigation parameters will be described in the results section.

3.1 Materials

The material used in this work is the Reactive Hydride Composite system of $2NaH + MgB_2$ / $2NaBH_4 + MgH_2$. The base materials were commercially purchased from the following suppliers:

Table 3.1: Materials used for experimental investigation and their sources.

Material	**Purity (%)**	**Supplier**
$NaBH_4$	98	Alfa-Aesar
MgH_2	95	Goldschmidt
NaH	95	Sigma-Aldrich
MgB_2	99.99	Alfa Aesar

3.2 Sample preparation by ball milling

To obtain homogeneous and nanostructured samples, the investigated materials were prepared by high-energy ball milling in a Spex 8000M shaker mill or a Fritsch P5 - planetary ball mill with a hardened stainless steel vial and milling

balls. The $2NaBH_4 + MgH_2$ samples were prepared using the Fritsch P5 - planetary ball mill, while the $2NaH + MgB_2$ and $3NaH + MgB_2$ samples were prepared using the Spex 8000M shaker mill. Material handling and all milling work were carried out in a purified argon atmosphere inside a glove box to prevent oxidation of the samples.

3.2.1 Spex shaker mill

In the Spex8000 shaker mill (figure 3.1), the materials were milled for 1 hour with a ball to powder ratio of 10:1 The Spex 8000-series mixer/mill is an efficient, compact laboratory mill capable of pulverizing samples in the 10-gram range. Functionally described as a shaker mill or high-energy ball mill, this mill shakes the hardened steel vial container back and forth about 1000 cycles per minute. The vial is shaken in a complex motion that combines back-and-forth oscillation with lateral movements. With each oscillation, the milling balls impact against one end of the vial and simultaneously mill the sample into nanoparticles.

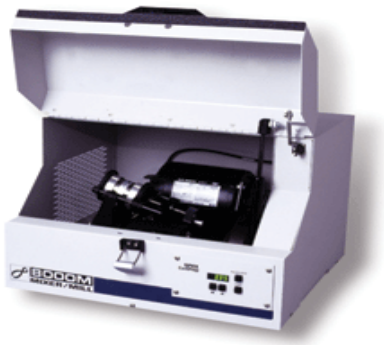

Figure 3.1: Photograph of a SPEX 8000M shaker mill at GKSS Research Center, Geesthacht Germany.

3.2.2 Planetary ball mill

In the Fritsch P5 - planetary ball mill (figure 3.2), the materials were milled for 20 hours with a ball to powder ratio of 10:1. The planetary ball mill is equipped with four steel vials and a "safe lock" clamping system and used for comminuting the bulk material to obtain a homogenized mixture. The apparatus mainly crushes the material by the high-energy impact of milling balls together with friction between the balls and the wall of the milling vial. The milling vessels with material and balls rotate around their own axis on a counter-rotating supporting disc as illustrated in figure 3.3. The centrifugal forces caused by the rotation of the milling vial and supporting discs work on the contents of the milling vessels. The milling balls cross the bowl at high speeds impacting with the material on the opposite wall thereby a creating size reduction by impact.

Figure 3.2: Photograph of a Fritsch P5-planetary ball mill at GKSS Research Center, Geesthacht Germany.

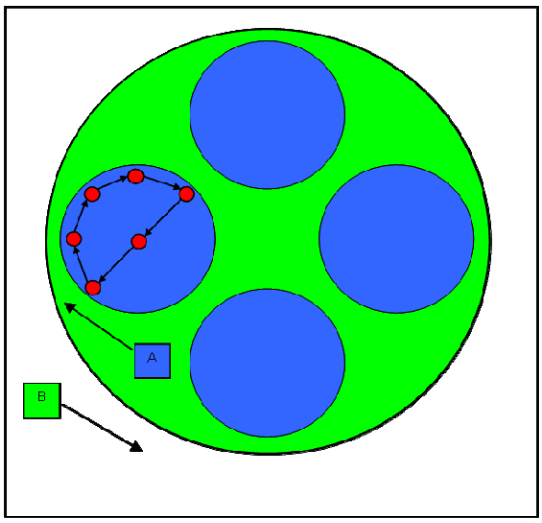

Figure 3.3: Schematic of a planetary ball mill showing the supporting disc (green), milling vial (blue) and the steel balls (red) in their rotation paths. The arrows “A” and “B” indicate the counter-rotating motions of the milling vial relative to the supporting disc.

3.3 Kinetic characterisation

The hydrogen sorption properties of the materials are measure using a Sievert´s-type apparatus (C2-3000) designed by HERA Hydrogen Systems Quebec, Canada. The measurement principle is based on the differential hydrogen pressure between the sample and an identical reference which are both subjected to the same measurement conditions. The amount of absorbed or desorbed hydrogen is obtained assuming the ideal gas law according to equation 3.1.

$$wt.\%H_2 = \frac{m_h \bullet V \bullet \Delta P}{R \bullet T \bullet m_s} \bullet (100) \qquad (3.1)$$

Where m_h = molar mass of hydrogen (g), V = total volume of hydrogen (m^3), ΔP = differential pressure (Pa), R = ideal gas constant (J/K.mol), T = chamber temperature (K), m_s = mass of sample (g).

Except where noted otherwise, hydrogen absorption measurements are performed by heating under 50/100 bar hydrogen pressure, from room temperature to 400 °C, and then held in isothermal conditions. Hydrogen desorption measurements are carried out by heating from room temperature to 450 °C, under an applied back pressure of 0.1 bar hydrogen, and then held in isothermal conditions. The standard heating rate for both absorption and desorption measurements is 3 °Cmin^{-1}. To curtail external influences from the surroundings, the main chamber containing the calibrated volume of gas is kept at 40 °C.

Figure 3.4: Photograph of the C2-3000 Sievert's-type apparatus used for volumetric analysis at GKSS Research Center, Geesthacht Germany.

3.4 Thermal analysis

Thermodynamic investigations of hydrogen absorption into $2NaH+MgB_2$ and hydrogen desorption from $2NaBH_4+MgH_2$ were carried out using the Netzsch DSC 204 HP Phoenix high-pressure differential scanning calorimeter (HP-DSC) with Al_2O_3 crucibles and lids. This apparatus measures the difference in temperature between the sample and the reference (empty crucible) as a function of either time or temperature. Both sample and reference are subjected to identical temperature during heating and cooling, at a controlled rate and the heat released or heat absorbed due to reactions is detected.

The DSC experiments were performed in collaboration with Mr. Claudio Pistidda of the Institute of Materials Research, at GKSS Research Centre Geesthacht, Germany. Measurements were performed between room temperature and 400/550°C at a heating rate of 5 °C min^{-1} and at a constant pressure throughout the temperature range. The standard back pressure is 50 bar hydrogen during the absorption reaction and 1 bar during the desorption reaction. The experiment is performed in a dedicated glove box under a purified argon atmosphere. The analysis provides qualitative information regarding the temperature of sorption reaction, formation and evolution of various phases.

The enthalpy change of reaction is determined by evaluating the area under the DTA peak. However, due to the complex reaction mechanism of these hydride systems, quantitative analysis of the hydrogenation and dehydrogenation processes cannot be obtained since the amounts of material involved in any single reaction step can not be accurately evaluated.

3.5 X-ray analysis

3.5.1 Ex-situ X-ray diffraction

X-ray Powder Diffraction (XRD) as illustrated in figure 3.5 is an efficient analytical technique to obtain structural information regarding the investigated material. X-rays are electromagnetic radiation with photon energies in the range of 100 eV - 100 keV. Only short wavelength x-rays otherwise referred to as hard x-rays in the range of a few angstroms to 0.1 angstrom (1 keV - 120 keV) are normally used for diffraction applications. This is because the wavelength is comparable to the size of atoms; hence they are ideally appropriate for characterising the phase composition and structural arrangement of atoms in materials. High energy x-rays are capable of penetrating deep into the samples and providing microstructural information about the material.

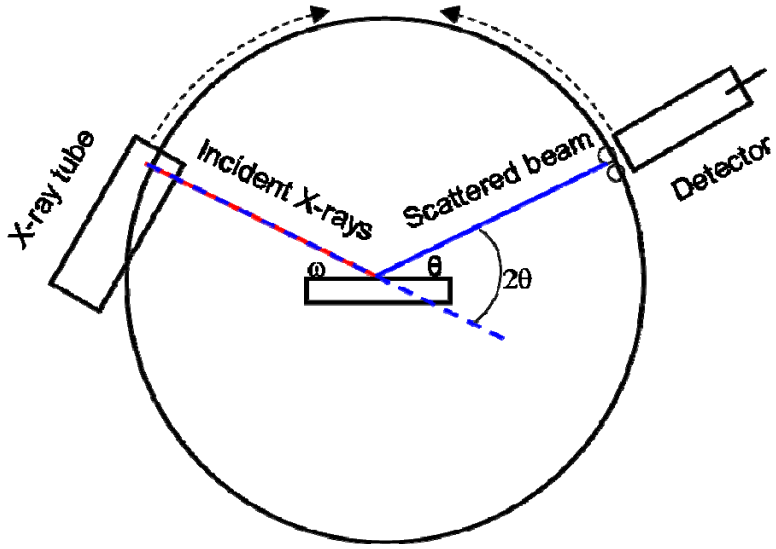

Figure 3.5: Experimental set-up of the X-ray diffractometer showing the X-ray tube, detector, incident X-rays and the scattered beam.

In bulk materials with randomly oriented crystalline domains, the diffraction pattern from a characteristic angle of diffracted X-rays shows concentric rings of scattering peaks which correspond to the different interplanar d spacings within the crystal lattice. The relative peak positions and their intensities are quantitatively analysed to identify the phase of the material being examined according to the Bragg law in equation 3.2. For a set of parallel planes of atoms (figure 3.6), with an interplanar distance d_{hkl} between them, constructive interference occurs when the Bragg's law is satisfied.

$$n \bullet \lambda = 2 \bullet d_{hkl} \bullet \sin\theta \qquad (3.2)$$

Where λ = wavelength of the x-ray, d_{hkl} = interplanar spacing q = the scattering angle, n = the order of the diffraction peak which is an integer.

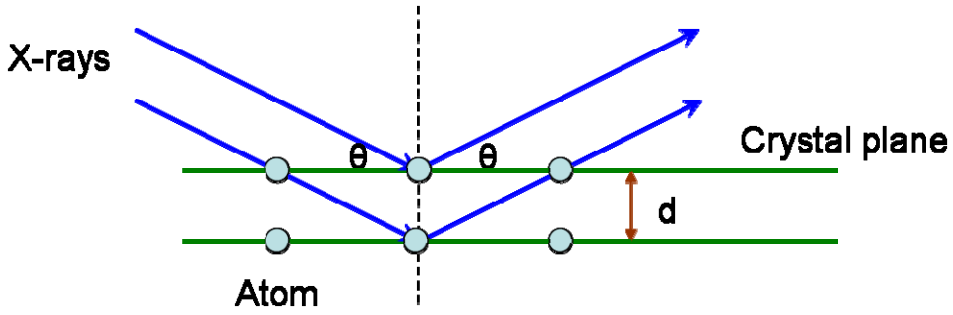

Figure 3.6: Schematic Illustration of the diffraction of parallel X-rays at a diffraction angle of θ, with a wavelength of λ from atoms in a set of crystal planes which are separated by an interplanar distance of d.

In this work, laboratory X-ray diffraction was performed using a Siemens D5000 diffractometer or a Bruker D8 Advance X-ray diffractometer both using Cu Kα radiation (λ = 0.15406 nm). Kapton film was used to protect the samples from oxidation. However despite the use of kapton foil to seal the samples it was impossible to completely avoid sample contamination by oxygen/moisture especially for slow scan measurements. The average crystallite sizes in Å were determined from the corresponding XRD spectra using the Debye-Scherrer formula in equation 3.3 [91].

$$D_{hkl} = \frac{k \bullet \lambda}{\beta \bullet \cos\theta} \qquad (3.3)$$

where k = 0.8 -- 1.39 (e.g. 0.9 is used in this work), λ the wavelength of the radiation (λ_{Cu} = 1.54056 Å), β the FWHM (full width at half maximum of diffraction peaks) in radians and θ half of the diffraction angle 2θ.

3.5.2 In-situ X-ray diffraction

The evolution of phases during hydrogenation and dehydrogenation reactions was investigated in-situ by Synchrotron Radiation Powder X-ray Diffraction (SR-PXD). The measurements are performed in transmission mode at the I711 beam line at the Max II Lab synchrotron in Lund Sweden.

The SR-PXD experiments were performed in collaboration with Mr. Claudio Pistidda of the Institute of Materials Research, GKSS Research Centre Geesthacht, Germany. The beam from a radiation source of 1.8 T multipole wiggler was focused vertically by a bendable mirror and horizontally by an

asymmetrically cut Si (111) monochromator [92]. The diffracted intensity was measured using a MAR 165 charge coupled device (CCD) plate detector, with wavelength in the range of 0.8-1.55 Å. Hydrogen pressures of up to 150 bar and temperatures up to 600°C can be applied in the experimental setup as shown in figure 3.7. The thermocouple which regulates the oven is integrated into a capillary tube containing the sample. The installed temperature controller allows for fluctuations in the order of ± 10 K, however a temperature disagreement of up to 50 K to the known equilibrium temperatures was observed.

Conclusions on sorption reaction mechanism are obtained from the quantitative analysis of the diffracted patterns relative to temperature and time.

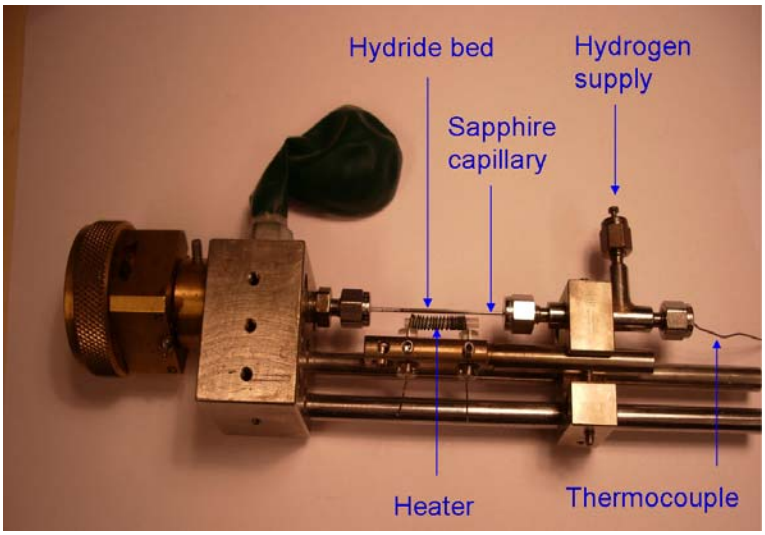

Figure 3.7: Photograph of the set up for in-situ XRD at I711 beam line, Max II Lab synchrotron, Lund.

3.6 Electron microscopy

Electron microscopy consists of a broad range of different techniques that use signals generated from the interaction of the electron beam with the sample to obtain information about crystallography, morphology, microstructure and composition. Electrons are charged particles and thus interact with the material through coulomb forces from both the positively charged atomic nuclei and orbiting electrons.

Conventional transmission electron microscopy involves the use of high-energy incident electrons to illuminate a thin sample through stages of a condenser lens system. The objective lens helps in the formation of either the image or diffraction pattern of the specimen. The intensity distribution of the incident electron behind the specimen is projected by a system of lenses enabling the image to be viewed on a screen. These incident electrons interact with a specimen in various ways and generate a broad range of secondary radiations and particles from the sample, as illustrated in figure 3.8. Most of the incident electron can pass through the specimen forming the non-scattered direct beam while many are elastically or inelastically scattered by the electrons or atomic nuclei of the specimen.

The scattered electrons, and other generated secondary signals are used by different TEM techniques to provide structural and chemical information of the sample [93]. Aspects of these techniques which are relevant to this work will be described in subsequent sections.

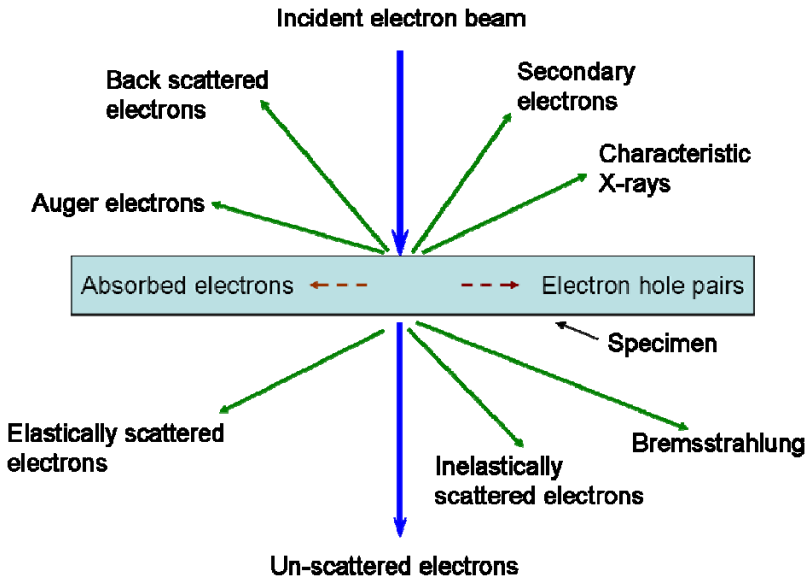

Figure 3.8: Signals generated when high energy incident electrons interact with a thin specimen.

3.6.1 Selected area electron diffraction

Electron diffraction is a collective scattering event with electrons being elastically scattered by atoms in a crystal. The resulting interference pattern is due to the interaction of the incoming plane electron wave with atoms thereby generating secondary waves which interfere with each other [93]. The interference of these waves occurs either constructively by generating diffracted beams at particular diffraction/scattering angles or destructively by cancelling out the beams completely. In selected area electron diffraction (SAED), the diffraction pattern contains electrons diffracted from a selected region confined by the selected area aperture. The area of sample where the electrons are diffracted depends on the size of the aperture. The diffraction pattern is observed

on a screen and recorded on a photographic film or on a charge coupled device (CCD) camera.

The advantages of electron diffraction over other methods like X-ray diffraction stems from the fact that the wavelength of an accelerated electron is much smaller than that of X-ray radiation. This enables a two dimensional distribution of the reciprocal lattice spots to be revealed. Furthermore, the geometry of an electron diffraction experiment can be varied over several incident angles by converging the electron beam into a cone, otherwise referred to as convergent beam electron diffraction. Like in X-ray diffraction (figure 3.6), electron diffraction can be described as a reflection of the beams from a parallel set of atomic planes and constructive interference occurs when the Bragg's diffraction condition is satisfied (equation 3.2).

$$n\lambda = 2d_{hkl}\sin\theta \qquad (3.2)$$

Where n is the order of diffraction and θ, the scattering/diffraction angle, λ is the wavelength of incident electrons and can be evaluated by the de Broglie relation (equation 3.4), d_{hkl} is the interplanar distance and can be determined from the diffraction patterns using equation 3.5.

$$\lambda = \frac{h}{p} \qquad (3.4)$$

(h= Planck's constant and p= particle momentum)

In figure 3.9 g_{hkl} is the diffraction vector from the central spot O to the first diffraction spot +G associated with particular (*hkl*) planes in the diffraction pattern. g_{hkl} is a vector in the reciprocal space with a length equal to d_{hkl} and an orientation perpendicular to the (*hkl*) planes [93]. The vector produces corresponding diffraction spots G when the orientation of the planes satisfies the Bragg law. Consequently, for crystalline materials, the interplanar spacings which are typical of a crystal structure can be determined from the diffraction pattern. Hence, by analyzing the diffraction patterns, it is possible to identify and distinguish between different crystal structures.

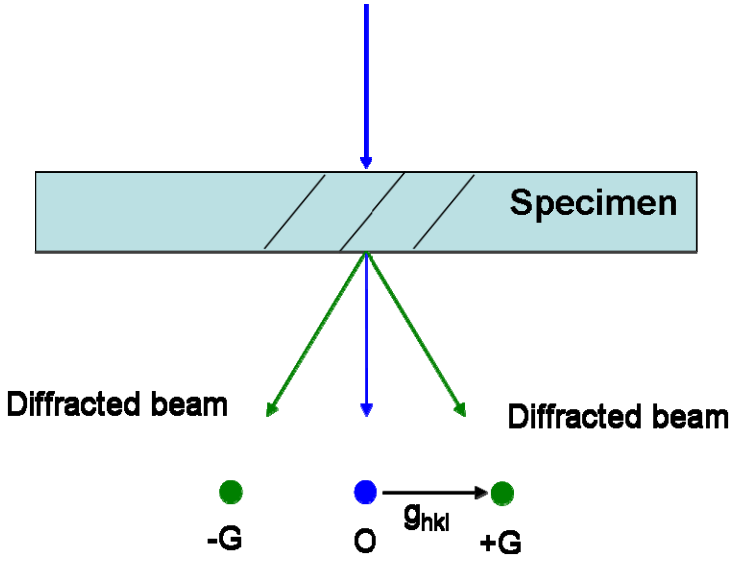

Figure 3.9: Schematic diagram illustrating the formation of electron diffraction pattern.

In this work, the lattice spacings d were evaluated by the following equation [93].

$$D \bullet d = L \bullet \lambda \qquad (3.5)$$

Where D is the length of the diffraction vectors g crystal spacing, λ is the wavelength of the incident electron beam and L is the camera length – the distance between the specimen and the image recording plane.

To enhance the accuracy of measured interplanar spacings, the camera length used in this work was calibrated using standard a thallous chloride sample which has well known crystal spacings. Phase identification was performed by matching the calculated lattice spacings with the reference crystallographic data available for material phases with known crystal structures. Different types of diffraction pattern result from different specimens depending on the grain size. While single crystals generally show a regular array of diffraction spots, polycrystals display ring patterns as shown in figure 3.10.

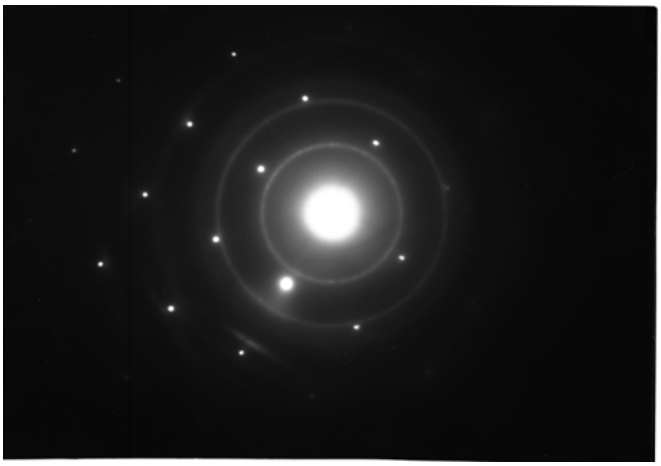

Figure 3.10: Example of selected area electron diffraction pattern from showing array of spots from a mono-crystalline material and ring patterns from a polycrystalline material.

3.6.2 Diffraction contrast - bright field and dark field imaging

The elastic scattering of electrons strongly depends on the scattering angle as the electron beam interacts with the electron cloud in the atom. In crystalline materials, the scattered beam is brighter (maximum intensity) at particular angles that satisfy Bragg-diffraction law. By either allowing only the transmitted beam or one of the diffracted beams to pass through the objective aperture, a bright field (BF) or dark field (DF) image is produced respectively (figure 3.11). This process gives rise to diffraction contrast and depends on the crystal structure and orientation of the sample [93].

In bright field mode, the aperture is placed in the back focal plane of the objective lens thereby allowing only the incident electron beam to pass through the optical axis. The resulting image is from the weakening of the direct beam as it interacts with the specimen. Hence, both mass-thickness and diffraction contrast contribute to the formation of the image. Mass-thickness contrast arises from incoherent elastic scattering of electrons, depending on the atomic number Z and the thickness of the sample. Thick areas, heavily enriched with atoms appear darker in bright field while thin areas appear brighter.

In dark field mode, the incident electron beam is either blocked or tilted so that only the diffracted beam passes through the optical axis. Thick areas, heavily enriched with atoms appear brighter in dark field while thin areas appear darker. Due to strong interactions between the diffracted beams and the specimen, valuable information about planar defects and particle size are obtainable from dark field images.

Diffraction contrast is dominant in single phase materials if the variations in sample thickness are minimal. The best diffraction contrast is achieved by setting up the two-beam dynamical diffracting condition where only one specific diffracted beam G is strongly excited.

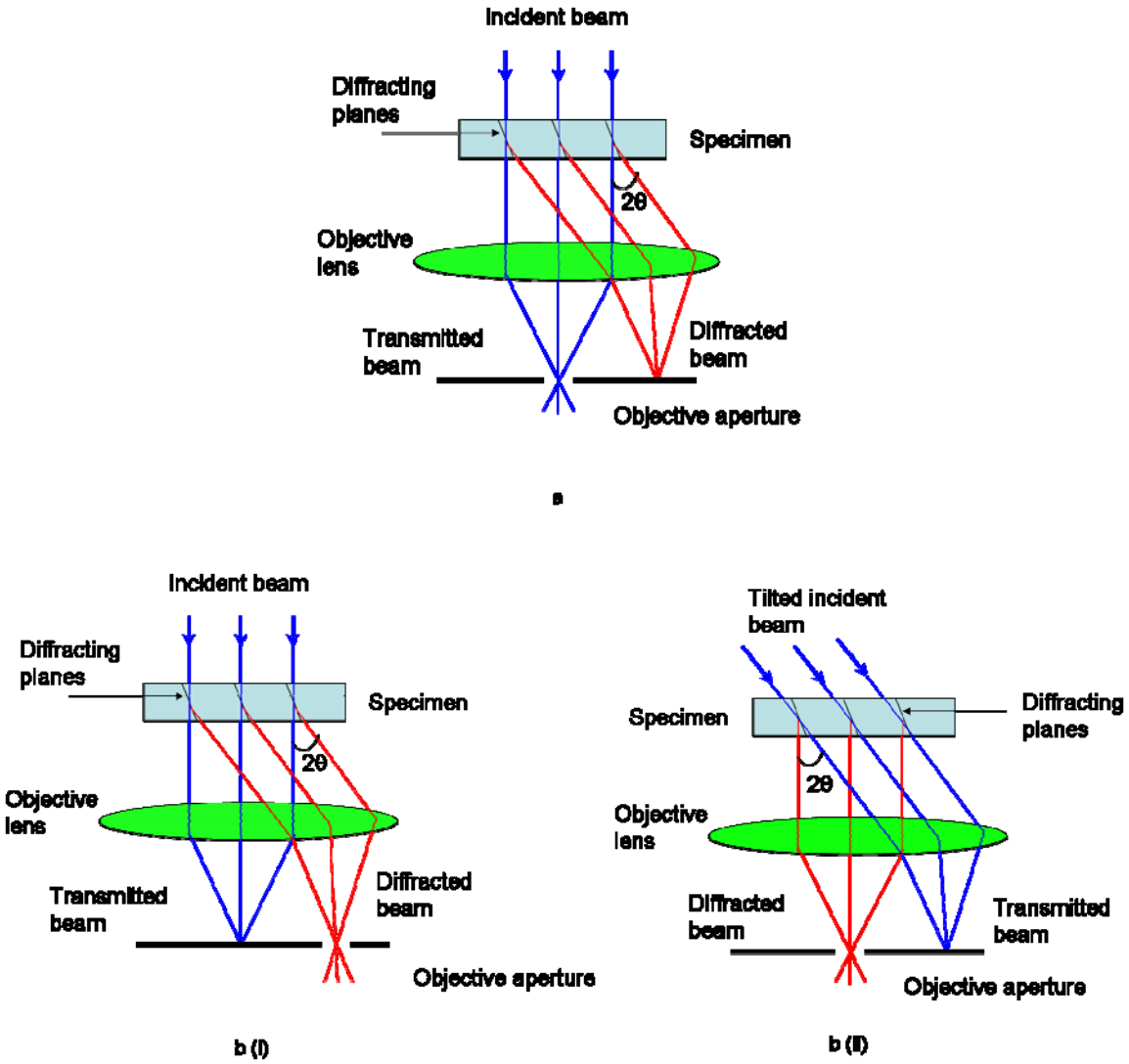

Figure 3.11: Schematic diagram illustrating (a) bright-field imaging, (b(i)) off-axis dark-field imaging and (b(ii) on-axis dark field imaging.

3.6.3 High resolution transmission electron microscopy

High resolution transmission electron microscopy (HRTEM) involves the use of phase contrast due to phase differences arising from interference of the incident electron beam with the diffracted beams. A high resolution image requires the selection of more than one beam. Therefore to obtain a phase contrast image of a thin specimen, a large objective aperture is selected to allow both the incident and diffracted beams to pass through the optical axis as schematically illustrated in figure 3.12.

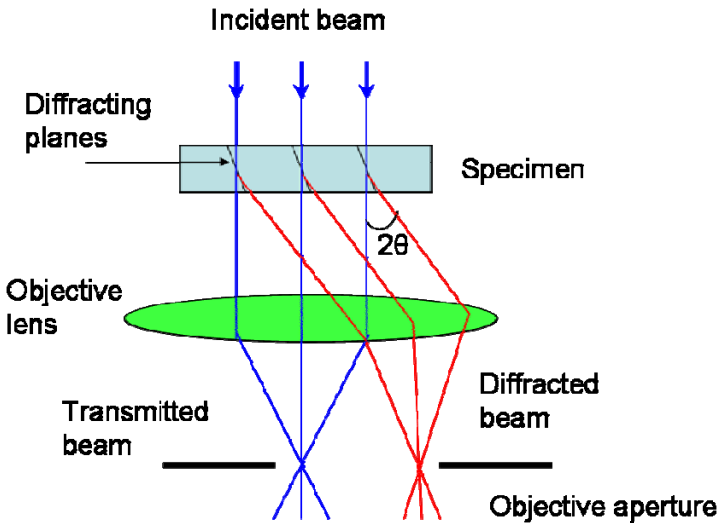

Figure 3.12: Schematic diagram illustrating imaging in high resolution transmission electron microscopy.

Considering the interference of the incident beam O and the diffracted beam G, the phase contrast in the **x** direction on a thin specimen is described by the following equation [93].

$$I = A^2 + B^2 + 2AB\sin(2\pi g' x - \pi s t)$$

where *I* is the beam intensity, *A* is the amplitude of the incident beam, *B* is related to the amplitude of the diffracted beam and depends on the extinction distance ξ_g for the diffraction vector *g*, and the excitation error *s*, *t* is the specimen thickness and *g' = g+s* along the *x* direction. The excitation error s describes the deviation from the exact Bragg diffraction.

The resulting phase contrast comes from the sinusoidal variation in intensity with different periodicities of g', along the direction *x* which is normal to *g'*. When *s* is equal to zero for reflection G, therefore g'=g, and consequently the lattice fringes in the HREM image will have a periodicity equal to *1/g* in the direction *x*. A periodicity variation when $s \neq 0$ are barely noticeable since s is very small. As the incident electron beam passes through a specimen, the elastic interaction results in modulations of its phase and amplitude. Thus the electron exit wave from the specimen contains information on lattice spacing and structure of the material.

However, due to aberrations in the objective lens (astigmatism, spherical C_s and chromatic C_c aberration), the quality of the image is reduced. The contrast transfer function (CTF) describes the intensity distribution of the exit wave function and can be explored via pass-band and aberration-free focus imaging to enhance image resolution [93].

In this work, high resolution transmission electron microscopy has been used in identifying the lattice structure and crystal orientations in nano-scaled reactive hydride composite material. To obtain crystallographic information, HRTEM images were analysed using the Gatan Digital Micrograph (DM) software to obtain the corresponding Fast Fourier Transform (FFT). In most cases, only a

single interplanar spacing was used for identification of phases. This could be at times assumptive because of the relatively small distances being measured. Hence, other confirmatory techniques are necessary to enhance accuracy.

3.6.4 Scanning transmission electron microscopy

In scanning transmission electron microscopy (STEM), a fine, convergent electron beam is scanned over an area of the specimen. The scanning of the electron beam is made possible by pairs of scan coils which keeps the beam parallel to the optic axis at all times [93]. In STEM, the scanned probe acts as multiple illumination sources and translate into discrete signals at the electron detector. At each spot on the specimen, the generated signal is recorded by selected detectors to build up an image of the scanned area after proportional amplification at corresponding points. Additionally, the convergent beam can provide well localized signals from the specimen. These signals are used for spectrometry. The convergence semi-angle α and the collection semi-angle β are essential parameters in quantitative STEM analysis involving energy dispersive X-ray spectroscopy and electron energy loss spectroscopy [93].

There are three types of STEM detectors and different types of STEM images can be obtained depending on the type of detector inserted:

When a bright field (BF) detector is used, only the intensity of the incident electron beam from a spot on the specimen is detected and this forms a bright field image.

The annular dark field (ADF) detector has a hole in its center and surrounds the BF detector. It detects all the scattered electrons and uses them to form an annular dark field image and the contrast primarily originates from coherent scattering and electron diffraction in crystalline regions of the specimen.

The high-angle annular dark field (HAADF) detector is a configured to only detect electrons scattered to higher angles greater than 5º. Therefore the central hole is much bigger than in the ADF detector. The resulting Z-contrast image which depends on elemental atomic number (Z) is almost all derived from incoherent scattering and can be very useful for phase identification.

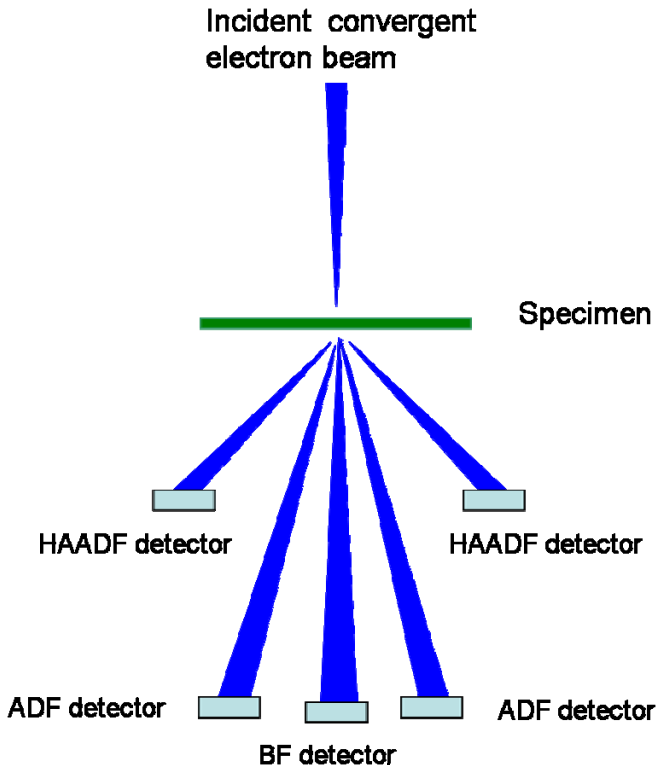

Figure 3.13: A schematic outline showing the arrangement of the various STEM detectors.

3.6.5 Energy dispersive X-ray spectroscopy

X-rays are among the signals generated as incident electrons interact with a specimen. The ionization of an atom in the specimen ejects an electron from an inner shell thereby creating an electron hole. This hole is immediately occupied by an outer shell electron leaving the atom in an excited energy state. To release the excess energy, a higher energy outer shell electron fills the created electron hole and in the process an X-ray photon is emitted, which is characteristic of energy difference between the two shells, and of the emitting atomic structure.

Furthermore if the high energy incident electrons are decelerated by interaction with the atomic nucleus or the field surrounding the nucleus, a background X-ray continuum or bremsstrahlung X-rays is produced [93]. Since any amount of energy can be lost by the incident electron beam, the energy distribution of the emitted X-trays is a continuum. The background radiation does not contain relevant information on material composition though it is a function of atomic number.

Energy dispersive X-ray spectroscopy (EDXS) is an important tool for quantitative and qualitative elemental analysis of a specimen. Each element has characteristic peak positions corresponding to the possible transitions in its electron shell. Most TEM are equipped with energy-dispersive spectrometers to detect generated X-rays. The processed EDX spectra as shown in figure 3.14 are recorded in the form of X-ray counts as a function of energy of the X-rays. The characteristic X-rays are displayed as Gaussian-shaped peaks superimposed on a background X-ray continuum. X-rays are produced from a

region in a specimen referred to as the excitation volume. The size and shape of the excitation volume depends on the incident electron beam energy and the specimen density. In a high Z material, the incident electrons are scattered further away giving rise to a greater interaction volume and reducing its penetration into the specimen. Whereas in low Z materials, the incident electrons penetrate more into the specimen losing some energy due to inelastic scattering events and consequently results in a smaller interaction area.

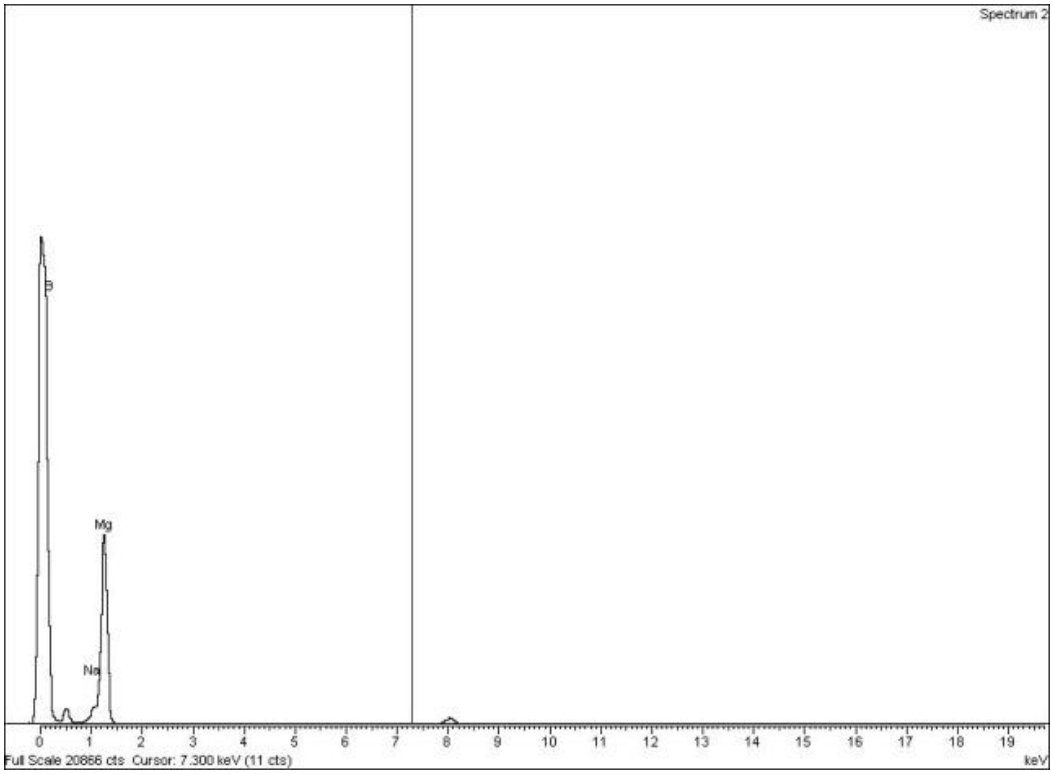

Figure 3.14: An EDX spectra of $2NaBH_4 + MgH_2$ reactive hydride composite.

The qualitative interpretation of EDXS data is generally easy. However, quantification is better for high Z elements due to better resolution. Low-energy X-rays from low Z elements are easily absorbed by the detector and by the

specimen or surrounding. During quantification, this absorption effect is not easily corrected with a high degree of accuracy. In addition, fluorescence yield is low for light elements as most events tend to produce more Auger electrons than X-rays. This consequently limits the detection sensitivity for light elements [94]. In the present work, EDXS was used to qualitatively analyze high Z elements (Na, Mg) in the $2NaBH_4+MgH_2$ reactive hydride composite.

3.6.6 Electron Energy loss spectroscopy

The inelastic scattering of the incident electrons as they interact with a specimen results in energy losses which are transmitted to the specimen exciting secondary signals. These signals carry plenty information about the sample and can be measured by Electron Energy loss spectroscopy (EELS) which analyzes the quantity of energy lost by electrons (ΔE). The Electron Energy loss spectrometer classifies the electrons based on their kinetic energy and generates an EELS spectrum in the form of the scattered intensity versus the energy losses.

A typical EELS spectrum, as schematically illustrated in figure 3.15 consists of three parts [95]:

(i) Zero-loss peak (ΔE = 0eV)

This mostly contains electrons that still possess the original beam energy E_0. This implies that the peak originates from only elastic interactions with the

specimen. The small energy spread of the incident electron beam as well as the inability of the spectrometer to resolve scattered phonons, results in peak broadening. The zero-loss peak is useful to measure the thickness of the sample.

(ii) Low-loss region (< 100eV)

This region mainly contains electrons that have suffered energy loss by plasma resonance of conduction or valence electrons in the specimen (induced plasmon oscillations) and inter-/intra-band transitions as the incident electrons interacts with a lone electron in an orbital. The signal generated in this region can provide vital information for microanalysis of the specimen chemistry. The intensity and number of plasmon peaks varies proportionally with the thickness of the specimen.

(iii) High-loss region (> 100eV)

The energy loses in this region arises from inelastic interactions of incident electrons as they ionize the inner or core shell electrons resulting in ionisation edges in the spectrum at energy losses which are characteristic for an element. For ionisation to take place, a specific minimum energy referred to as the ionization threshold is required. This threshold energy corresponds to the onset of the ionisation edge [95]. Furthermore, the amount of inelastically scattered electrons significantly decreases as the energy loss increases,

therefore the high-loss peaks appear as superimposed edges on a smoothly decreasing background.

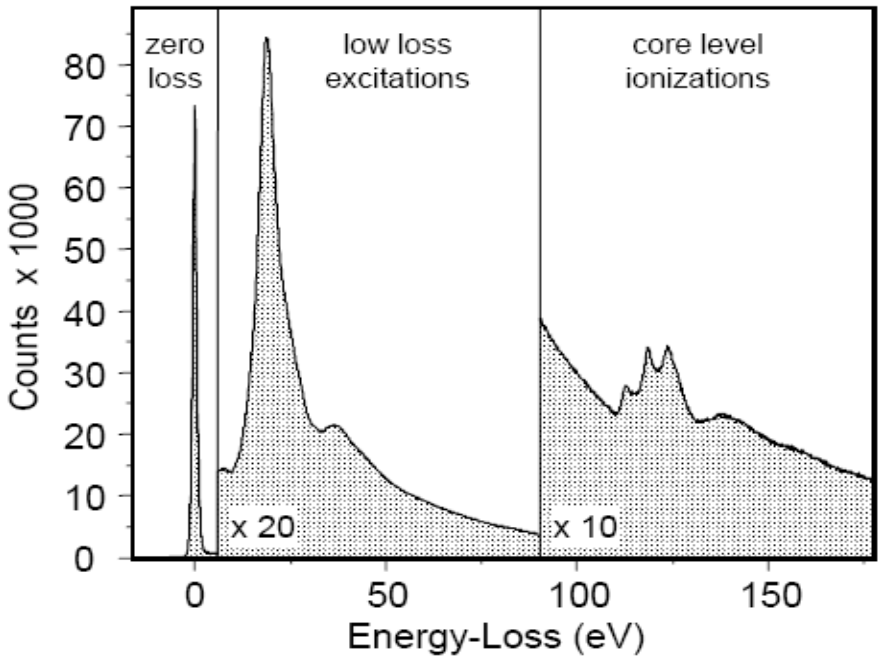

Figure 3.15: Schematic diagram of an EELS spectrum showing the zero-loss, low-loss and high-loss regions.

EELS is a complementary tool to EDXS and can also be used for qualitative and quantitative elemental analysis by comparing the experimental data with reference spectra. The main advantage of EELS over EDXS is its ability to detect low Z (light) elements with better energy resolution.

The main limitation in using EELS to analyse $NaBH_4$ - MgH_2/$NaMgH_3$ composites is the irradiation of the hydride material by incident electron beam. This contaminates the sample, resulting in multiple scattering which degrades peak resolution and prevents good microanalysis.

In this work, the microstructure of as-milled and heat-treated samples (after absorption and desorption) was investigated. Material handling and sample preparation for TEM were carried out in a dedicated glove box under a purified argon atmosphere because of the high sensitivity of these hydride materials to air and moisture. A ground powder sample was dispersed in n-hexane and a drop of the supernatant liquid placed on a lacey-carbon film supported on a copper grid. The coverage of the sample by hexane inhibits reaction with the environment and the hexane is pumped off in the air lock chamber of the microscope.

TEM, STEM and HRTEM investigations were carried out using the JEOL-JEM 2010 with LaB_6 emission gun microscope at 200kV and JEOL-JEM 3000F with field emission gun (FEG) microscope at 300kV.

The JEOL-JEM 2010 has a point resolution of 0.19nm and a maximum specimen tilt of 10 degrees along both axes. The instrument also has a Gatan 676 TV-rate image pickup system and an Erlangshen CCD camera located above the viewing screen. In addition it is equipped with an Oxford Instruments LZ5 windowless energy dispersive X-ray spectrometer (EDXS) controlled by INCA.

The JEOL-JEM 3000F has a point resolution of 0.16nm with (+/-25 degrees) for both single and double tilt specimen holders. The instrument also has an INCA controlled energy dispersive X-ray spectrometer (EDXS) with a super atmospheric thin window (SATW) detector. It is also equipped with a high angle annular dark field (HAADF) detector allowing electron energy loss spectra to be acquired in STEM mode. In addition, a Gatan imaging filter (GIF) equipped with a

2k 794IF/20 Mega Scan CCD camera allows chemical analysis using electron energy loss spectroscopy (EELS).

Although particular attention was paid to prevent the contamination of the samples by air and/or moisture, this could not be completely avoided because the samples were slightly exposed to air for approximately 5 seconds prior to inserting the sample holder into the microscope airlock chamber.

4.0 Results and discussion

This section explores the hydrogen absorption properties of 2NaH + MgB_2 and 3NaH + MgB_2 systems as well as the hydrogen desorption properties of $2NaBH_4$ + MgH_2, and $2NaBH_4$ + $NaMgH_3$ systems. The hydrogenation and dehydrogenation mechanisms in as-milled 2NaH + MgB_2 + $4H_2$ ↔ $2NaBH_4$ + MgH_2 and in as-milled 3NaH + MgB_2 + $4H_2$ ↔ $2NaBH_4$ + $NaMgH_3$ were carefully examined considering the effects of temperature and hydrogen backpressure.

Using a combination of various characterisation techniques like volumetric analysis, differential scanning calorimetry, ex-situ and in-situ X-ray diffraction techniques and electron microscopy, important properties like reaction kinetics, storage capacity, intermediate reactions and phases formed were analysed and relevant conclusions drawn.

4.1 Hydrogen absorption in 2NaH + MgB_2 composite

4.1.1 Analysis of as-milled 2NaH + MgB_2

In a first approach, the microstructure and phase distribution in as-milled 2NaH + MgB_2 was performed to reveal microstructural changes in the material as a result of ball milling and to confirm typical phases present in the material as well as their stability under the electron beam. The bright field image and selected area electron diffraction pattern (SAED) of as-milled 2NaH + MgB_2 are shown in figures 4.1a and 4.1b. In the diffraction pattern, NaH and MgB_2 are

observed as the major phases in the system after milling, thus indicating that neither significant reaction nor oxygen contamination of the starting materials took place during ball milling.

Similarly, these two main phases are clearly observed in the HREM image shown in figure 4.2 which displays fringe contrast in the crystalline regions of the sample. The lattice fringes are indexed as $d_{(111)}$ = 0.2830 nm / $d_{(220)}$ = 0.1730 nm and $d_{(101)}$ 0.2127 nm corresponding to cubic NaH and hexagonal MgB_2 respectively. There is a clear presence of amorphous regions in the image which could be due to interaction between the electron beam and the sample or probably generated by high energy milling.

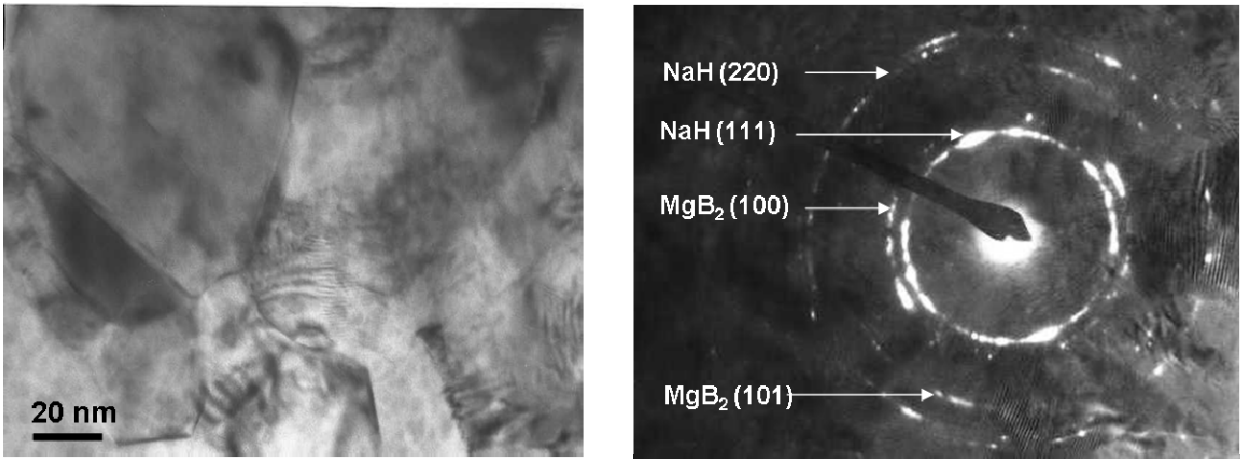

(a) (b)

Figure 4.1: (a) Bright field image of as-milled 2NaH + MgB_2 and **(b)** Selected area electron diffraction pattern of as-milled 2NaH + MgB_2 (JEOL-JEM 2010 at 200kV).

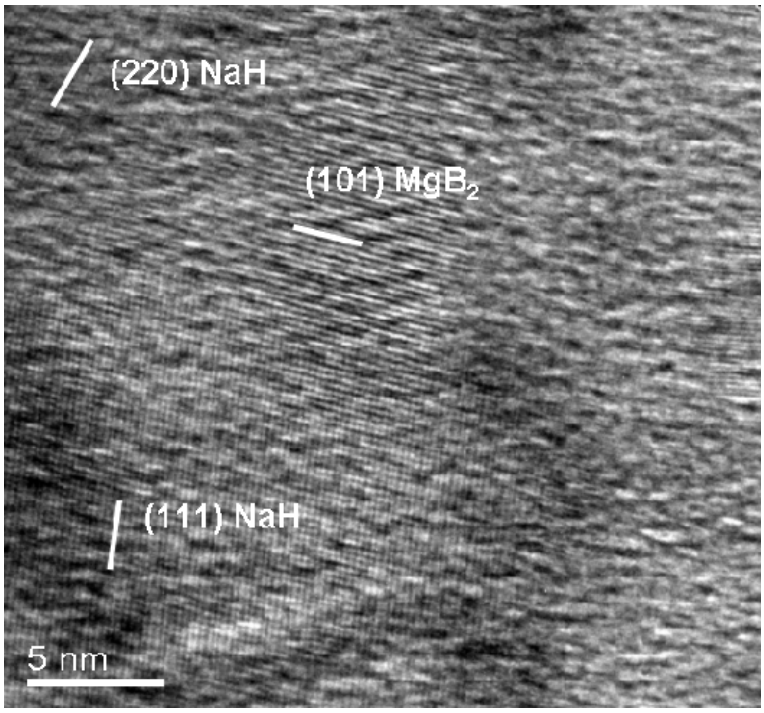

Figure 4.2: High resolution TEM image of as-milled 2NaH + MgB_2 (JEOL-JEM 3000F at 300kV).

4.1.2 Volumetric analysis – Kinetics

For a phenomenological understanding of the overall reactions during hydrogen sorption, volumetric analysis by hydrogen absorption was performed on as-milled 2NaH + MgB_2 in 50 bar hydrogen pressure. The system was heated to a temperature of 400 ^{o}C at a heating rate of 3 °Cmin^{-1} and then held isothermally at this temperature for several hours. Figure 4.3 shows the hydrogenation kinetics of the system indicating a two step absorption reaction with onset temperature of 250 ^{o}C. During the first step of reaction, only 0.6 wt.% hydrogen was absorbed into the sample while 3.2 wt.% hydrogen intake was

recorded in the second step yielding a total amount of 3.8 wt.% absorbed hydrogen. Considering a theoretical hydrogen capacity of 7.8 wt% for the system, it is obvious that the hydrogenation process is incomplete and does not follow a single step reaction according to the expected equation:

$$2NaH + MgB_2 \rightarrow 2NaBH_4 + MgH_2 \quad [11] \qquad (4.1)$$

Furthermore, it is worth mentioning that the estimated equilibrium temperature for the absorption reaction, based on the RHC concept is 350 ^{o}C. However, despite the thermodynamic driving force supplied by heating to 400 ^{o}C, the full absorption capacity was not attained.

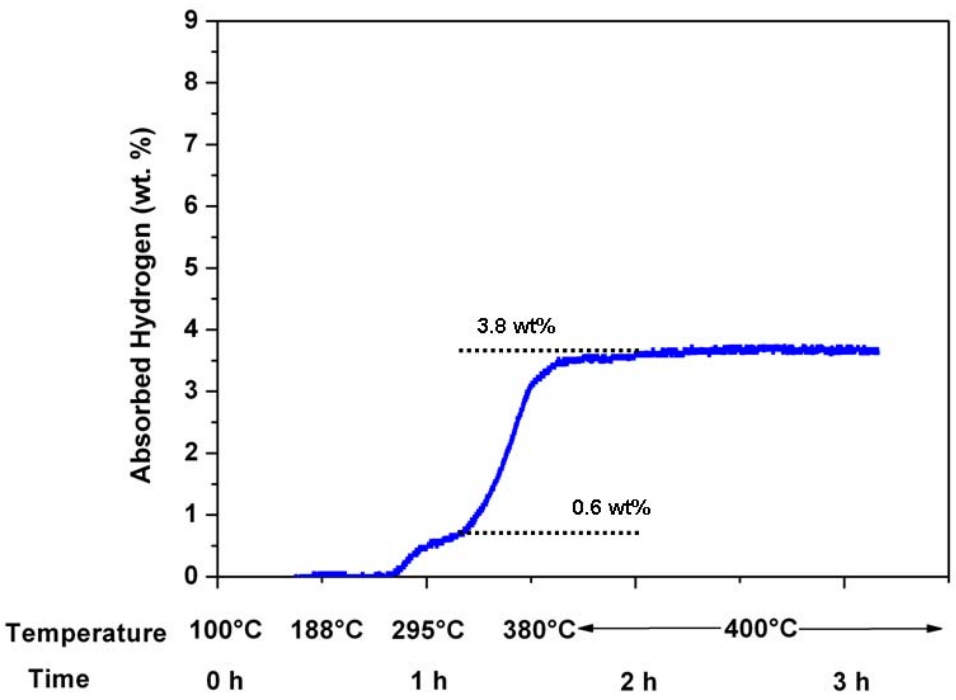

Figure 4.3: Absorption kinetics of as-milled 2NaH + MgB_2 heated to 400 ^{o}C from room temperature, in 50 bar H_2 at a heating rate of 3 ^{o}Cmin^{-1}.

To understand the reason(s) behind the partial hydrogenation process, the products of the absorption reaction were characterised by powder X-ray diffraction as shown in figure 4.4. Besides unconverted reactants (NaH and MgB_2), $NaBH_4$, $NaMgH_3$ and Mg were detected in the products of absorption reaction. The formation of $NaMgH_3$ and Mg (rather than MgH_2) was unforeseen, considering that MgH_2 is thermodynamically more stable than Mg under the experimental conditions of 400 ^oC in 50 bar hydrogen.

It can be noted that the reaction products seem to wet the inner surfaces of the sample holder, suggesting that one or more steps of the hydrogenation reaction occur via molten phase. In fact, previous work [96] reported the formation of a NaH-$NaBH_4$ molten phase during the absorption of 2NaH + MgB_2 in 50 bar H_2 .

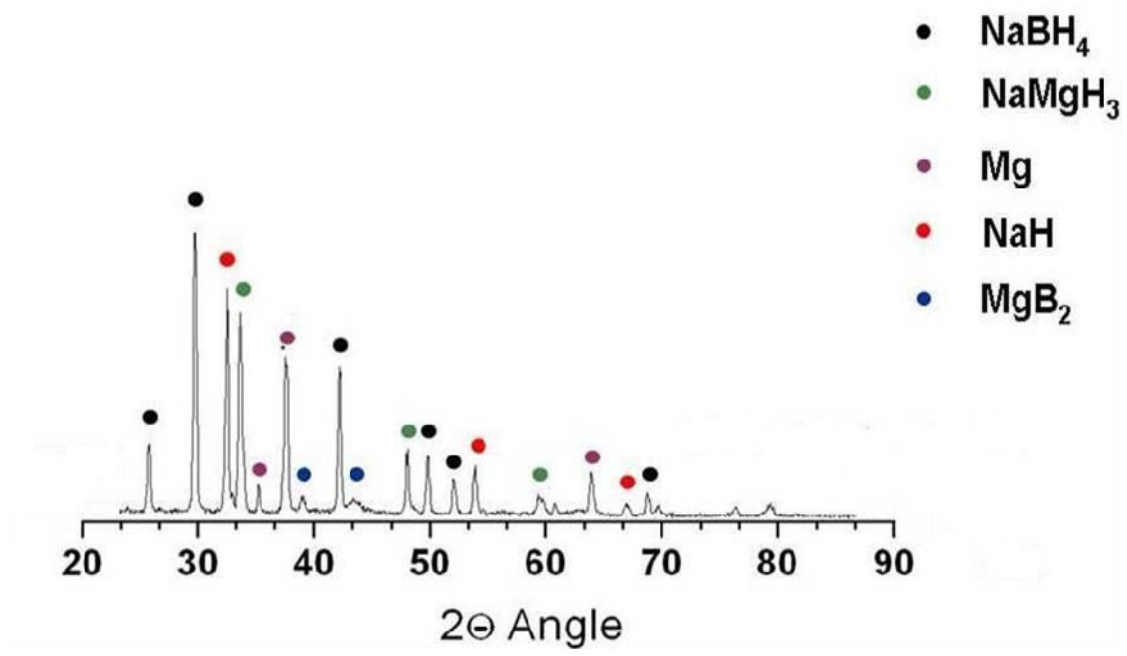

Figure 4.4: XRD pattern of 2NaH + MgB_2 after absorption under 50 bar H_2 at 400°C (wavelength λ= 1.54184 Å).

4.1.3 Thermal analysis

More details on the reactions occurring during hydrogen absorption were also investigated by HP-DSC analysis as shown in figure 4.5. The spectra were recorded while heating to 400 ^{o}C from room temperature, in 50 bar hydrogen pressure at a heating rate of 5 ^{o}Cmin^{-1}. During heating, two distinct exothermic peaks with onsets at 270°C and 353°C were observed and are associated with the formation of hydride phases. One endothermic peak was also observed at 330°C, corresponding to an unknown intermediate reaction. A detailed account of these events will be presented in the next section (4.1.4).

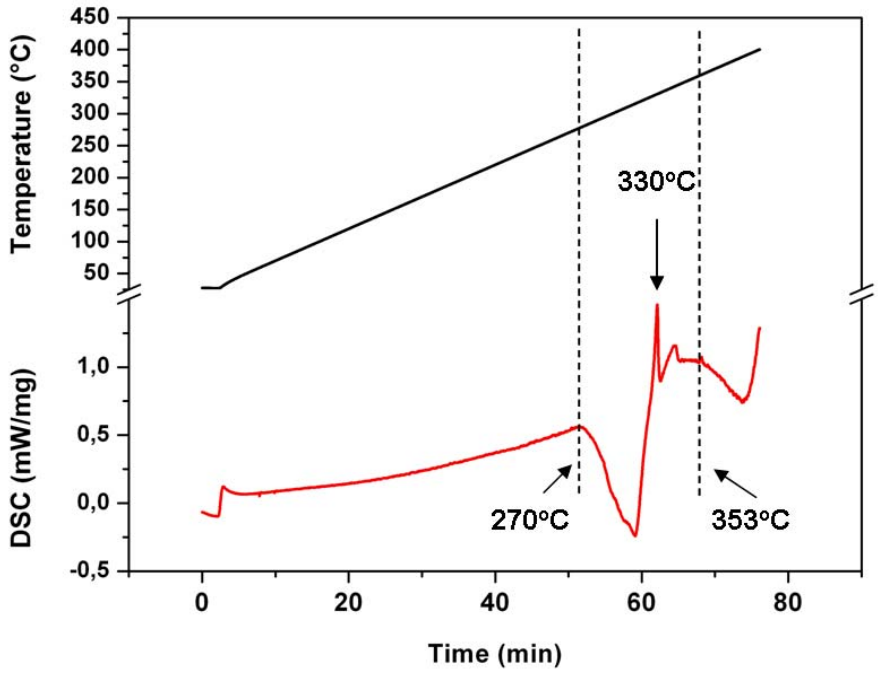

Figure 4.5: HP-DSC spectra of absorption reactions in as-milled 2NaH + MgB_2 heated to 400 ^{o}C from room temperature, in 50 bar H_2 at a heating rate of 5 ^{o}Cmin^{-1}.

4.1.4 In-situ X-ray diffraction analysis

Further investigation of the hydrogen absorption mechanism in the 2NaH + MgB_2 system was carried out by in-situ powder X-ray diffraction (SR-PXD) analysis. The in-situ X-ray technique is unique because results are not influenced by changes in experimental condition due to rapid cooling of the samples. In-situ hydrogenation measurement was carried out at the same temperature and pressure as the volumetric/kinetic analysis in figure 4.3.

Figure 4.6 shows the SR-PXD patterns (λ = 1.09719 Å) of 2NaH + MgB_2 absorbed in 50 bar hydrogen pressure from room temperature to 400°C at a heating rate of 5 $^{o}Cmin^{-1}$ and held isothermally. Because of thermal expansion during the heating cycle, it is observed that all peaks shift constantly towards lower 2θ angles. Un-reacted residues: NaH and MgB_2 were observed, as well as $NaBH_4$, $NaMgH_3$, Mg and an unknown phase. A stepwise description of this analysis shows that during heating from room temperature, an unknown phase with major reflections at 14.36, 16.59, 19.54, 23.54 and 27.79 2θ angles appears at about 280 ^{o}C and was observed to be stable up to about 320 ^{o}C after which the diffraction peaks disappear. This event is succeeded by the formation of perovskite-type $NaMgH_3$ at about 330 ^{o}C followed by an amorphous background (molten phase) at 19.50 2θ angle and the appearance of crystalline $NaBH_4$ at about 380 ^{o}C up to the final measurement temperature of 400 ^{o}C. The disappearance of the unknown phase reflections confirms that it is an intermediate phase eventually consumed in the course of the hydrogenation reaction. Furthermore, it can be seen that the formation of $NaMgH_3$ was

preceded by a massive reduction in the diffracted peak intensity of NaH while Mg appeared simultaneously as $NaBH_4$ was formed.

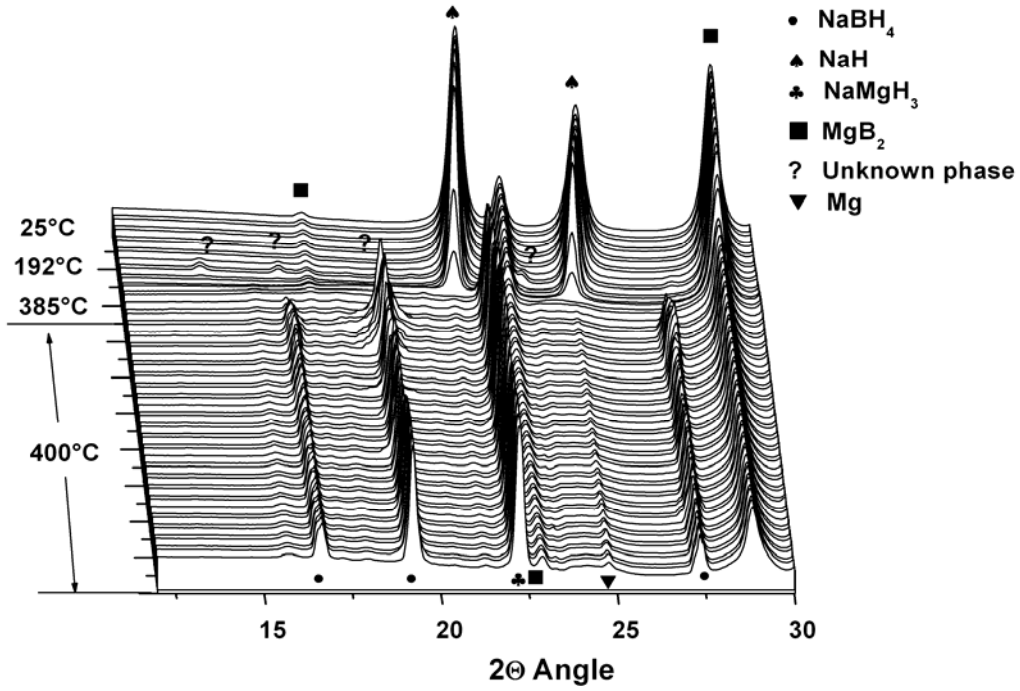

Figure 4.6: In-situ XRD patterns of as-milled 2NaH + MgB_2 absorbed in 50 bar H_2, from 20 ^oC to 400 ^oC at 5 °$Cmin^{-1}$and held isothermally (λ = 1.09719 Å).

To clarify the information described above, additional in-situ XRD analysis of as-milled 2NaH + MgB_2 was performed in 50 bar hydrogen, from room temperature to 400 ^oC at 5 °$Cmin^{-1}$ and then cooled to 240°C at a cooling rate of 5 °$Cmin^{-1}$ (see figure 4.7). During the heating cycle, the sequence of events is exactly the same as those described for figures 4.5 and 4.6. The cooling cycle can be described by two major events at 370 and 320°C, respectively. At about 370°C the peak intensity of NaH and $NaBH_4$ increased rapidly due to the solidification of the NaH-$NaBH_4$ molten phase. No changes to the $NaMgH_3$ formed during

heating were observed. Around 320°C, the peaks associated with the unknown phase re-emerged owing to the presence of un-reacted NaH and MgB_2. In addition, the earlier observed amorphous phase disappeared at the same time. No further changes occurred during cooling until the measurement was stopped.

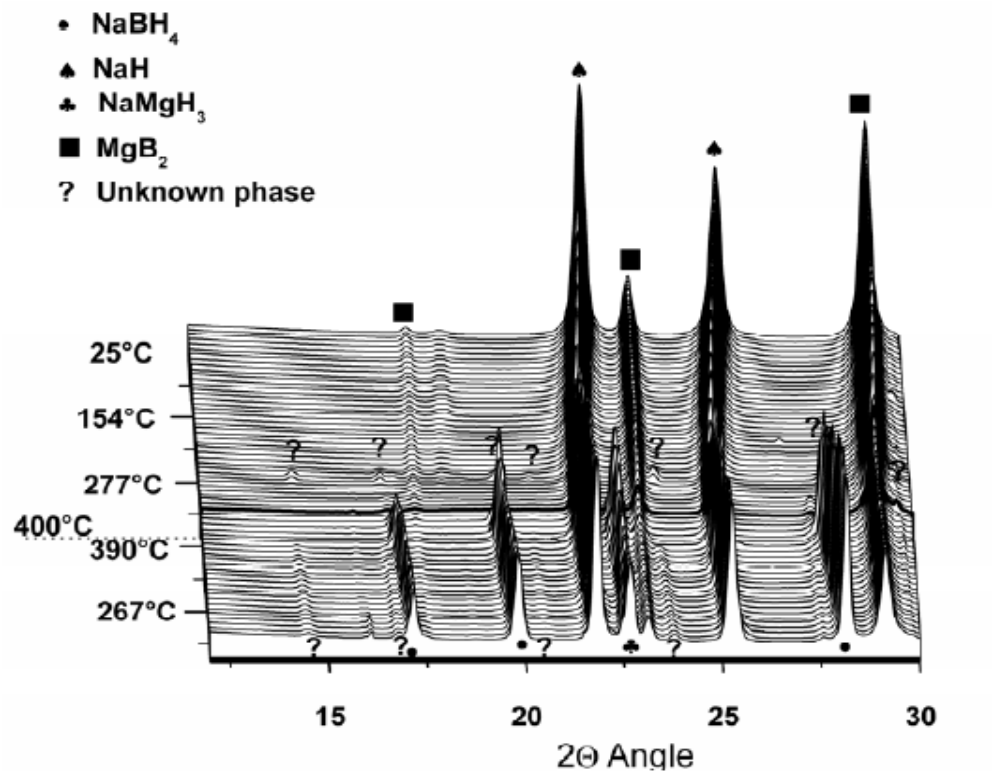

Figure 4.7: In-situ powder XRD patterns of as-milled 2NaH + MgB_2 absorbed in 50 bar H_2, from room temperature to 400 ^oC at 5 °C$min^{-1}$and then cooled to 240 ^oC at 5 °Cmin^{-1} (wavelength = 1.07200 Å).

4.1.5 Transmission electron microscopy analysis

TEM offers the capability to understand the structural transformations during the complex reactions in 2NaH + MgB_2 composite. Hence, to further comprehend

the reason(s) behind the partial hydrogenation observed in section 4.1.2, the products of the absorption reaction were characterised by transmission electron microscopy.

Figures 4.8a and 4.8b show a high resolution image and selected area diffraction pattern for 2NaH + MgB_2 after absorption in 50 bar hydrogen pressure at 400 ^{o}C. In both the HRTEM image and SAED pattern, the presence of the initial reactants; MgB_2 and NaH was clearly observed as well as the formation of $NaBH_4$, These are indicated by (101) hexagonal reflection of MgB_2 d_{101}= 0.2127 nm, (111) cubic reflections of NaH d_{111}= 0.2830 nm and the (002) cubic reflection of $NaBH_4$ d_{002}= 0.3065 nm. MgH_2 was not detected, instead reflections from (111) lattice fringes of perovskite-type hydride $NaMgH_3$ d_{111}=0.2720 nm were seen. Also, contrary to the in-situ XRD analysis in figure 4.6, free Mg was not detected.

Furthermore, an overlapping of lattice planes of MgB_2 with those of $NaMgH_3$ and $NaBH_4$ was observed and the formation of $NaMgH_3$ and $NaBH_4$ appeared to take place preferentially around the MgB_2 particles. Apparently, the presence of un-reacted starting materials as well as $NaMgH_3$ and free Mg substantiate the non-attainment of complete hydrogen capacity of 7.84 wt.% from absorption of the 2NaH + MgB_2 system.

The theoretical hydrogen capacity of $NaMgH_3$ according to equation 4.2 is approximately 4.0 wt%. Hence the partial hydrogen intake of about 3.8 wt% observed in this system is more or less consistent with equation 4.2.

$$NaH + Mg + H_2 \rightarrow NaMgH_3 \quad (4.2)$$

According to Ikeda et al [97] $NaMgH_3$ is thermodynamically more stable than MgH_2. This explains the non appearance of MgH_2 in the absorption product at 400 ^oC since the formation of MgH_2 is immediately succeeded by the formation of $NaMgH_3$ according to equation 4.3.

$$NaH + MgH_2 \rightarrow NaMgH_3 \quad (4.3)$$

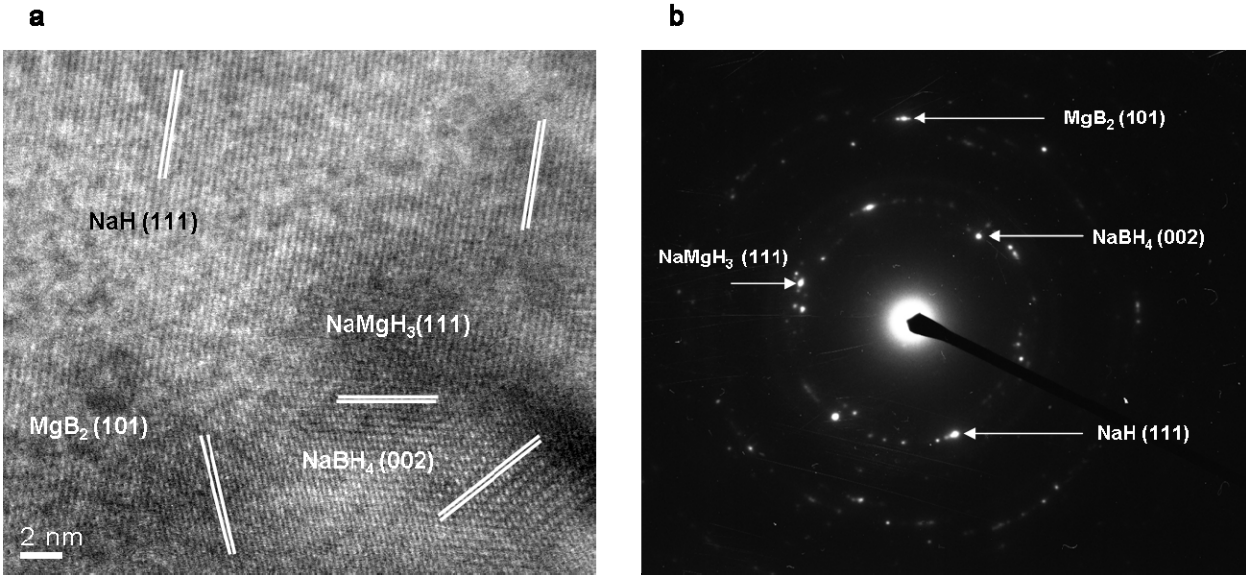

Figure 4.8: (a) HRTEM image of 2NaH + MgB_2 after absorption in 50 bar H_2 at 400 ^oC **(b)** Selected area electron diffraction pattern (SAED) of 2NaH + MgB_2 after absorption in 50 bar H_2 pressure at 400 ^oC (JEOL-JEM 3000F at 300kV).

4.1.6 Investigation of the unknown phase

To understand the make-up of the unknown phase observed in section 4.1.4 and its potential role in the mechanism of hydrogen absorption in 2NaH + MgB_2, hydrogenation measurement was performed in 50 bar hydrogen pressure from

room temperature to 280 ^{o}C. This measurement is of particular interest since the formation of the unknown phase commences at this temperature. Figure 4.9 shows, the hydrogen absorption kinetics of as-milled 2NaH + MgB_2 in 50 bar hydrogen. The system was heated from room temperature to 280 ^{o}C at a heating rate of 3 ^{o}Cmin^{-1}and held isothermally at this temperature and then cooled down to room temperature at the same rate. This was done to produce an appreciable amount of the unknown phase for microstructural analysis.

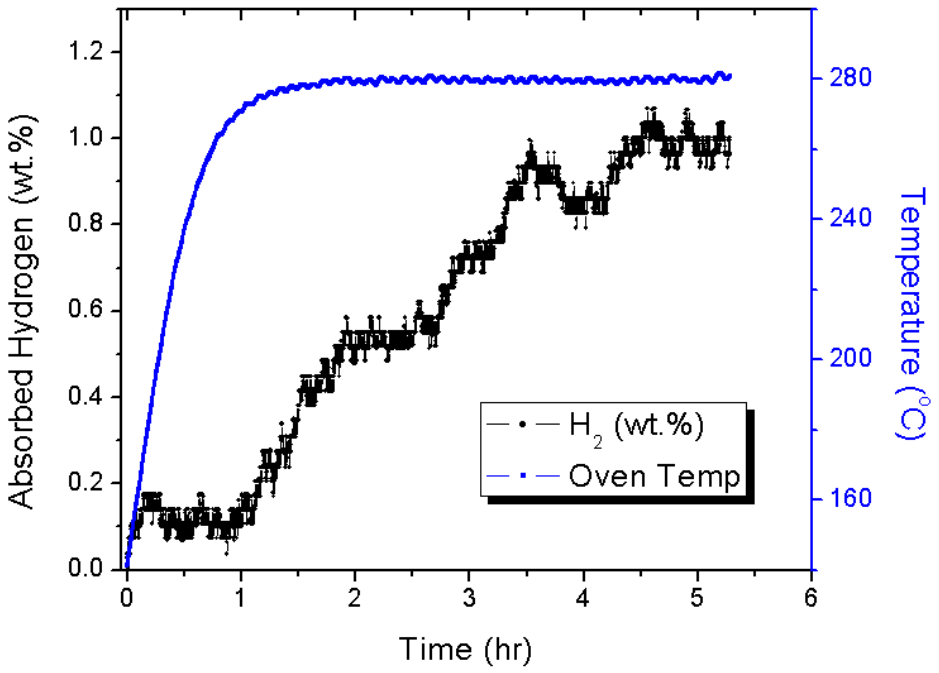

Figure 4.9: Absorption kinetics of as-milled 2NaH + MgB_2 in 50 bar H_2 from room temperature to 280 ^{o}C at a heating rate of 3 ^{o}Cmin^{-1}.

The results indicate a partial hydrogen intake of roughly 1.0 wt% into the system after 5 hours. The X-ray powder diffraction pattern (figure 4.10) of the

system after absorption in 50 bar hydrogen pressure at 280 ^{o}C clearly shows the presence of mainly starting reactants (NaH + MgB_2) with several other peaks ascribed to the unidentified phase. The unusual presence of NaOH is due to slight oxidation of the specimen probably during X-ray powder diffraction measurement. From the analysis of the XRD peak positions, the detected peaks belongs to neither MgH_2 nor $NaBH_4$, although both hydrides are expected to form in conditions of 280 ^{o}C and 50 bar hydrogen [11]. Hence, it is obvious that this detected unknown phase contains hydrogen and is thus a hydride phase [98].

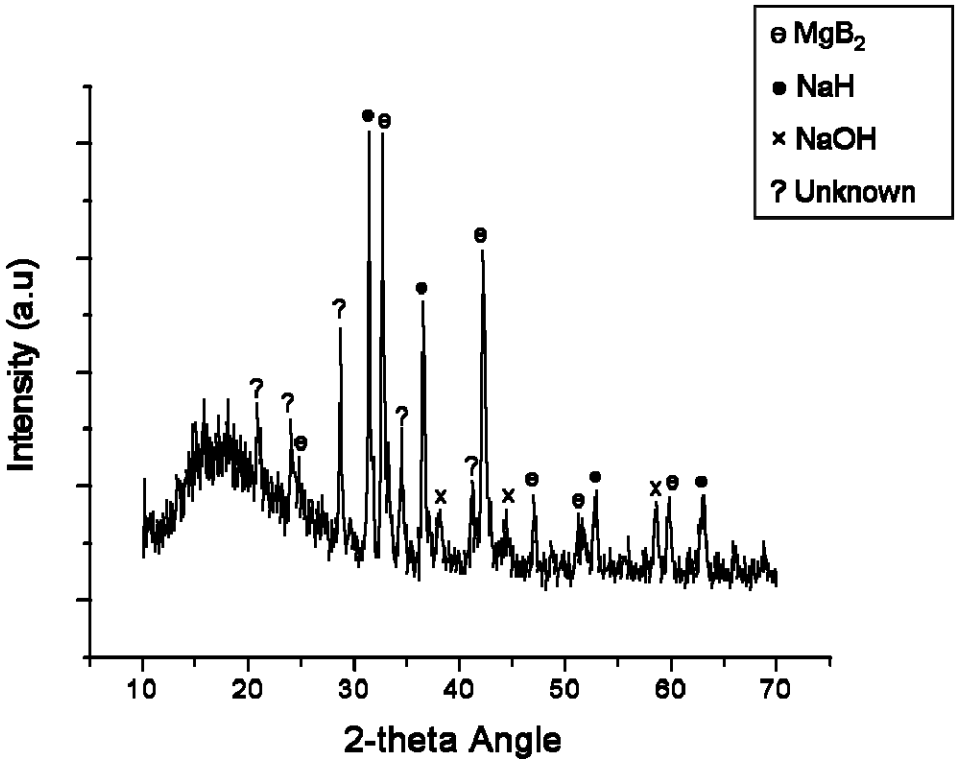

Figure 4.10: X-ray powder diffraction patterns of 2NaH + MgB_2 after absorption in 50 bar H_2 at 280 ^{o}C (wavelength = 1.54184 Å). Symbols: ɵ MgB_2, ● NaH, × NaOH, ? Unknown phase.

Scanning transmission electron microscopy (STEM) using a high angle annular dark field (HAADF) detector was also performed on 2NaH + MgB_2 absorbed in 50 bar hydrogen pressure from room temperature to 280 ^{o}C. Figure 4.11a shows the STEM-HAADF image with light and dark contrasts across the sample. The elemental maps indicate areas containing Mg and Na in the sample. B could not be detected by EDS due to its low (Z) atomic number. Point analyses on different regions of the sample in figure 4.11b reveal that lighter areas contain Mg-based particles while the darker areas contain Na-based particles. Furthermore, the very dark regions seem to show the presence of both Mg and Na particles.

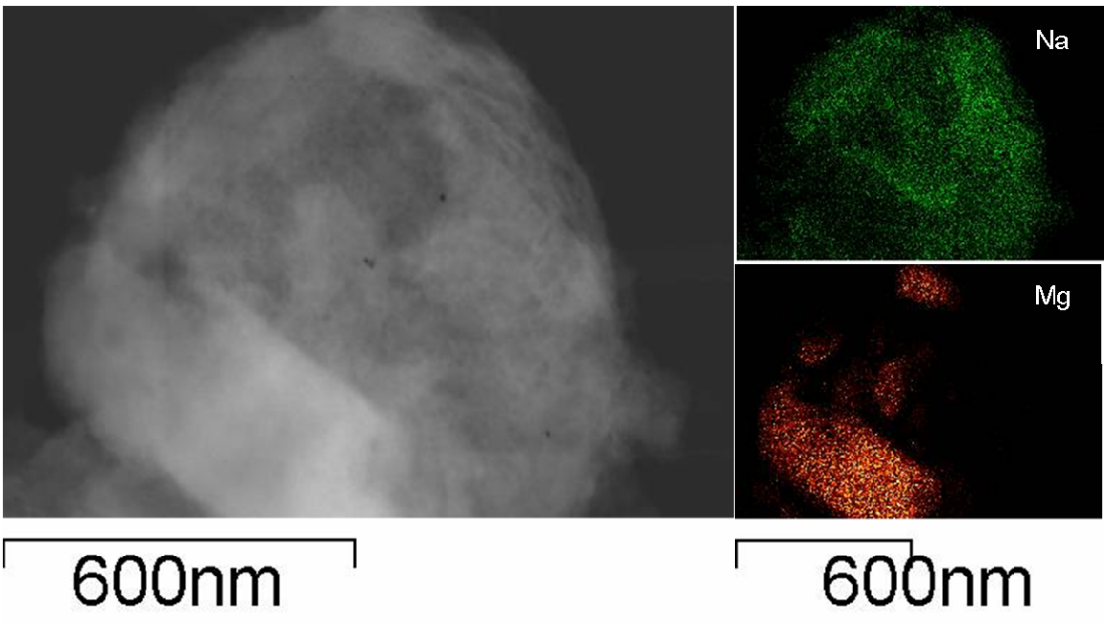

Figure 4.11a: STEM-HAADF image of 2NaH + MgB_2 after absorption in 50 bar H_2 from room temperature to 280 ^{o}C at a heating rate of 3 ^{o}Cmin^{-1} and EDS maps of Mg and Na (JEOL-JEM 3000F at 300kV).

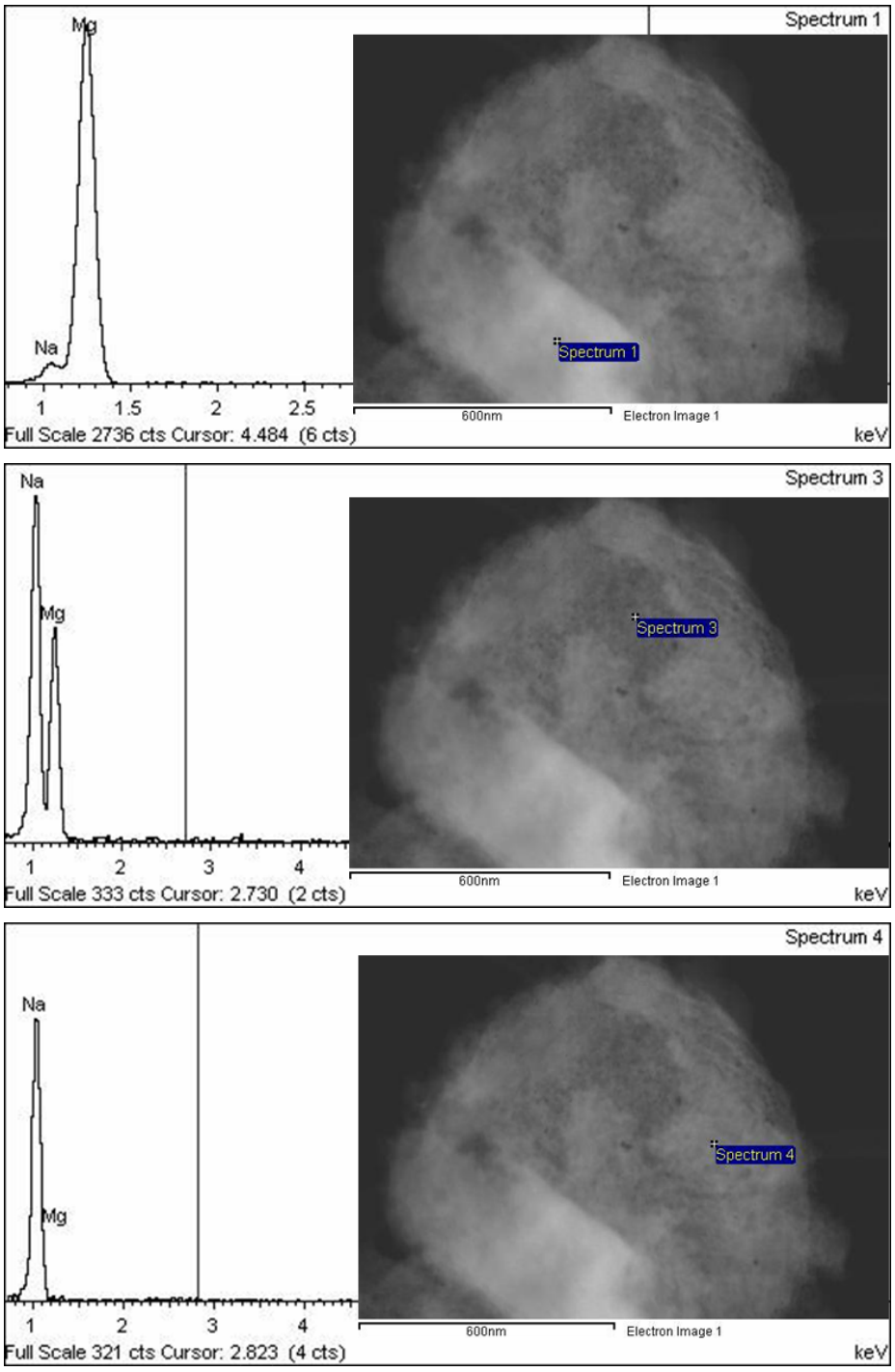

Figure 4.11b: EDX point analyses (spectrums 1, 3 and 4) on STEM-HAADF image of 2NaH + MgB_2 after absorption in 50 bar H_2 from room temperature to 280 ^oC at a heating rate of 3 $^oCmin^{-1}$ (JEOL-JEM 3000F at 300kV).

To obtain good spatial resolution, high resolution transmission electron microscopy was performed on the sample. The HRTEM image of 2NaH + MgB_2 partly absorbed in 50 bar hydrogen pressure at 280 ^{o}C is shown in figure 4.12 displaying fringe contrast in the crystalline regions of the sample. Similar to results in figures 4.6 and 4.10, this analysis also shows the presence of starting reactants indicated by $d_{(100)}$ = 0.2671 nm / $d_{(101)}$ = 0.2127 nm reflections for MgB_2 and $d_{(111)}$ = 0.2830 nm / $d_{(200)}$ = 0.2440 nm reflections for NaH and also a region corresponding to the unknown hydride phase with indexed $d_{(hkl)}$ = 0.1988 nm. This phase is observed to form between NaH and MgB_2 particles, leading to the supposition that the phase contains B and Na or Mg [98]. However, the indexed FFT pattern (figure 4.12 inset) of lattice fringes from the unknown phase could not be matched to any reference crystallographic data hence, further analysis is essential.

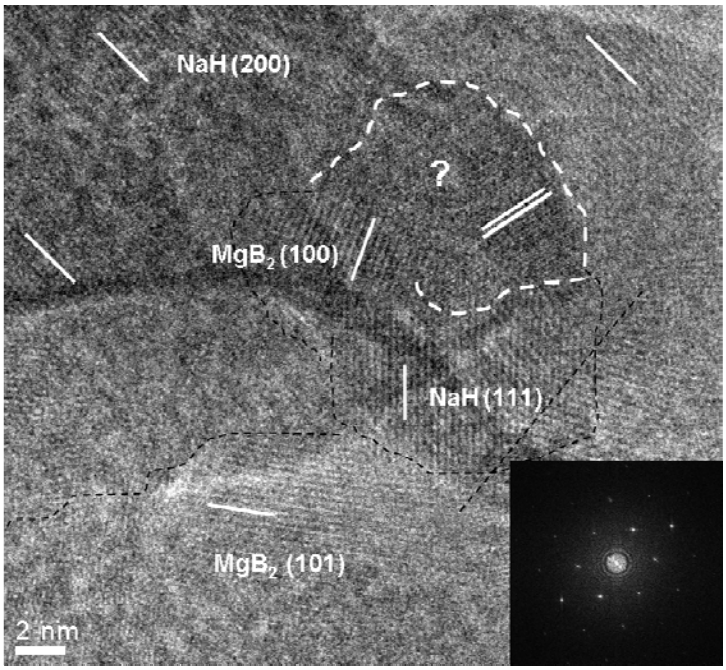

Figure 4.12: HRTEM image of 2NaH + MgB_2 after absorption in 50 bar H_2 from room temperature to 280 ^oC at a heating rate of 3 $^oCmin^{-1}$. (Inset: Fast Fourier Transform (FFT) of unknown phase) (JEOL-JEM 3000F at 300kV).

4.2 Hydrogen desorption in $2NaBH_4 + MgH_2$ composite

4.2.1 Analysis of as-milled $2NaBH_4 + MgH_2$

Microstructure and phase distribution are essential issues for the functionality of reactive hydride composites, because the diffusion of metal atoms has a significant effect on overall sorption reaction in these materials. To determine the effects of ball milling on the microstructure, the as-milled sample was examined by X-ray powder diffraction and transmission electron microscopy. Firstly, compositional and structural analysis of as-milled $2NaBH_4 + MgH_2$ was performed

by X-ray powder diffraction (XRD) to reveal any change(s) induced by ball milling. The diffraction pattern in figure 4.13 indicates diffraction peaks corresponding to $NaBH_4$ and β-MgH_2 with no trace of oxides found in the sample. Average crystallite size of 15 nm and 85 nm for βMgH_2 and $NaBH_4$ respectively were measured. The crystallite size for γMgH_2 could not be obtained because only very small proportions of the metastable high pressure polymorph γMgH_2 are formed from βMgH_2 during high energy ball milling.

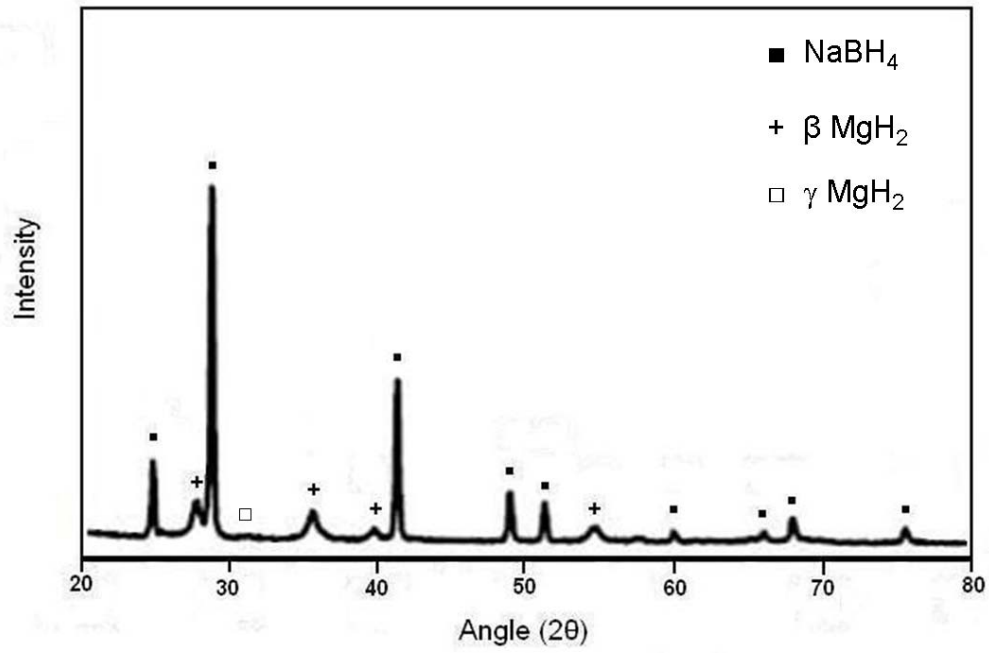

Figure 4.13: X-ray powder diffraction patterns of as-milled $2NaBH_4 + MgH_2$ (wavelength = 1.54184 Å). Symbols: + β-MgH_2, □ γ-MgH_2,▪ $NaBH_4$.

Secondly, transmission electron microscopy was used to examine the as-milled material showing the size and distribution of different phases present. Figure 4.14 shows the bright field and selected area electron diffraction (SAED)

pattern of the sample. The bright field image shows nanosized distribution of $NaBH_4$ and MgH_2 grains inside the polycrystalline powder as indicated by uniform diffraction rings in the SAED pattern. The indexed SAED pattern indicates strong intensities from cubic $NaBH_4$ and tetragonal MgH_2 phases and shows good stability under the electron beam with no evidence of significant contamination during mechanical milling. The diffused (311) reflection of cubic MgO, not seen in the X-ray study, can be attributed to slight oxidation of the hydride during transfer into the TEM or possibly due to the interaction of the sample with residual oxygen in the microscope airlock.

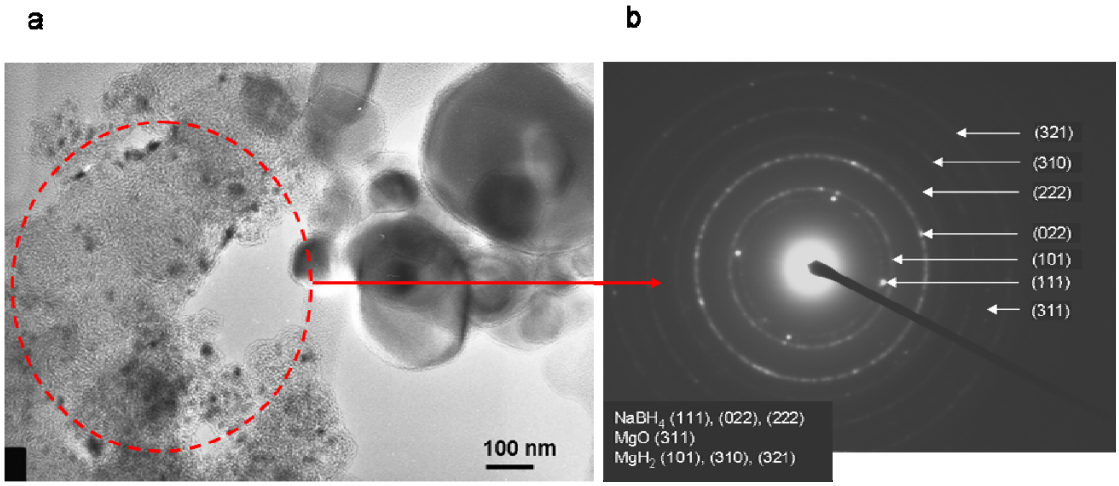

Figure 4.14: (a) Bright field image of as-milled $2NaBH_4 + MgH_2$ and **(b)** Selected area electron diffraction pattern of as-milled $2NaBH_4 + MgH_2$ (JEOL-JEM 2010 at 200kV).

As-milled $2NaBH_4 + MgH_2$ was further characterized by high resolution electron microscopy as shown in figure 4.15. The image shows fringe contrast in the crystalline regions of the sample. The presence of Mg indicates a slight

decomposition of MgH_2 under the electron beam. The following lattice spacings were indexed; 0.2510 nm, 0.2452 nm and 0.2167 nm corresponding to tetragonal $d_{(101)}$ MgH_2, hexagonal $d_{(101)}$ Mg and cubic $d_{(022)}$ $NaBH_4$ respectively. In addition, it is observed that MgH_2 seem to be embedded within the matrix of $NaBH_4$. Some amorphous regions are also visible in the image. This is due to the destructive interaction between the electron beam and the sample.

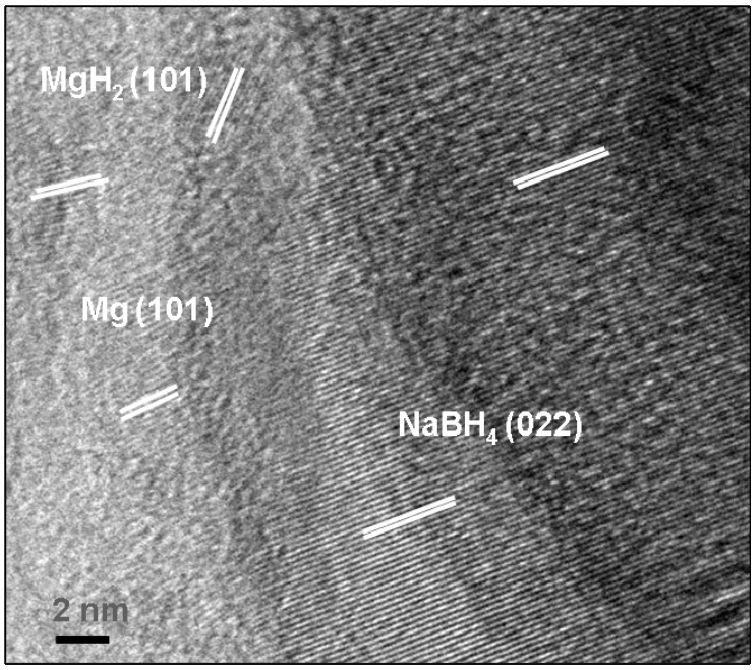

Figure 4.15: HRTEM image of as-milled $2NaBH_4 + MgH_2$ (JEOL-JEM 3000F at 300kV).

4.2.2 Volumetric analysis – Kinetics

Dehydrogenation measurement was performed on as-milled $2NaBH_4 + MgH_2$. The measured desorption kinetics are displayed in figure 4.16. Earlier attempts

to dehydrogenate as-milled $2NaBH_4 + MgH_2$ in equilibrium pressure condition of 1 bar H_2 from room temperature up to 450 ^oC proved abortive due to thermodynamic restrictions. The sample was heated in 0.1 bar hydrogen from room temperature to 450 ^oC at a heating rate of 3 $°Cmin^{-1}$ and then held isothermally at this temperature for several hours. The kinetic curve shows a two-step desorption reaction which are characterized by different reaction rates. The first desorption step commenced at about 295°C and released about 1.8 wt.% hydrogen, while in the second step 6.0 wt.% was released between 370-420°C. The two steps released a total of 7.8 wt% of hydrogen after 12 hours. Considering that the theoretical hydrogen storage capacity of $2NaBH_4 + MgH_2$ is 7.84 wt%, a complete reaction is thus obtained by 450°C according to equation 4.4.

$$2NaBH_4 + MgH_2 \rightarrow 2NaBH_4 + Mg + H_2 \rightarrow MgB_2 + 2NaH + 2H_2 \qquad (4.4)$$

Contrary to the 350 ^oC estimated as the equilibrium desorption temperature for this composite hydride by the RHC concept, it is noteworthy that a higher temperature up to 450 ^oC was required to provide the thermodynamic driving force for complete desorption. In addition, the formation of MgB_2, should take place at the same time as the decomposition of MgH_2 so as to obtain the desired thermodynamic effect. However, this is not the case because the reaction proceeds in multi-steps.

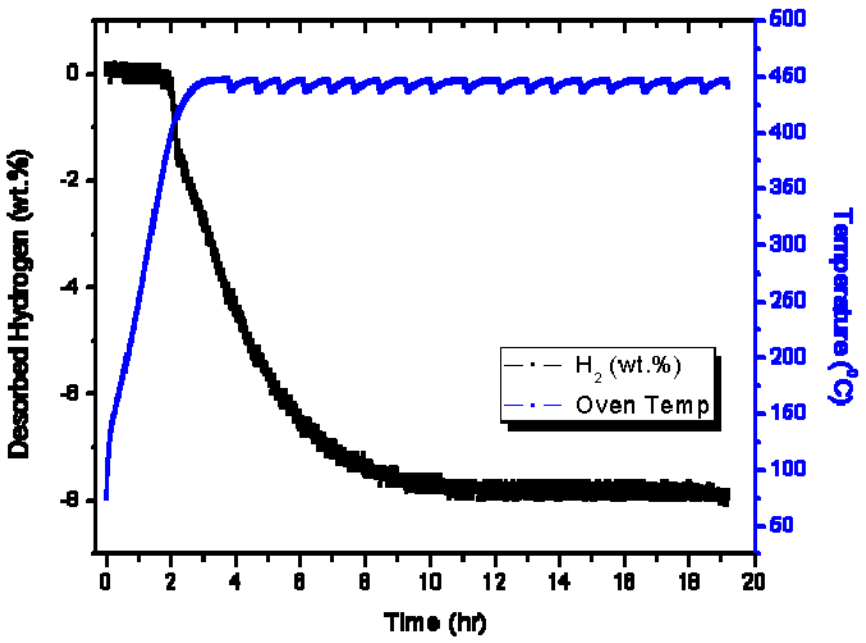

Figure 4.16: Desorption kinetics of as-milled $2NaBH_4 + MgH_2$ heated from room temperature to 450 ^oC at a rate of 3 $^oCmin^{-1}$, in 0.1 bar H_2.

4.2.3 Thermal analysis

For enhanced understanding of the complex reactions taking place during hydrogen desorption, the system $2NaBH_4 + MgH_2$ was examined by combined calorimetric and spectrometric techniques as shown in figure 4.17. The thermal analysis was obtained by heating the sample from room temperature up to 550°C at the rate of 5 $°Cmin^{-1}$ in a 150 $mLmin^{-1}$ continuous argon flow. The DSC trace (A) shows four distinct endothermic peaks, each of which is connected to a particular event as indicated by the mass spectrometry (B). The first broad endothermic peak with onset at 285°C is associated with the initial release of

hydrogen from MgH_2 and ends at about 350°C. At 400°C the second endothermic peak corresponding to some intermediate reactions is accompanied by a little release of hydrogen from the sample. Two additional endothermic peaks are observed at 450°C and 475°C. The former is linked to the melting of $NaBH_4$ while the latter, showing a considerable release of hydrogen, is related to the decomposition of $NaBH_4$. $NaBH_4$ is known to melt and decompose at about 505°C and between 550-650°C respectively under equilibrium pressure condition of 1 bar H_2 [2, 69]. However, the prior formation of metallic Mg from the decomposition of MgH_2 seem to have had a significant destabilizing effect on $NaBH_4$ thereby favouring its decomposition at lower temperature.

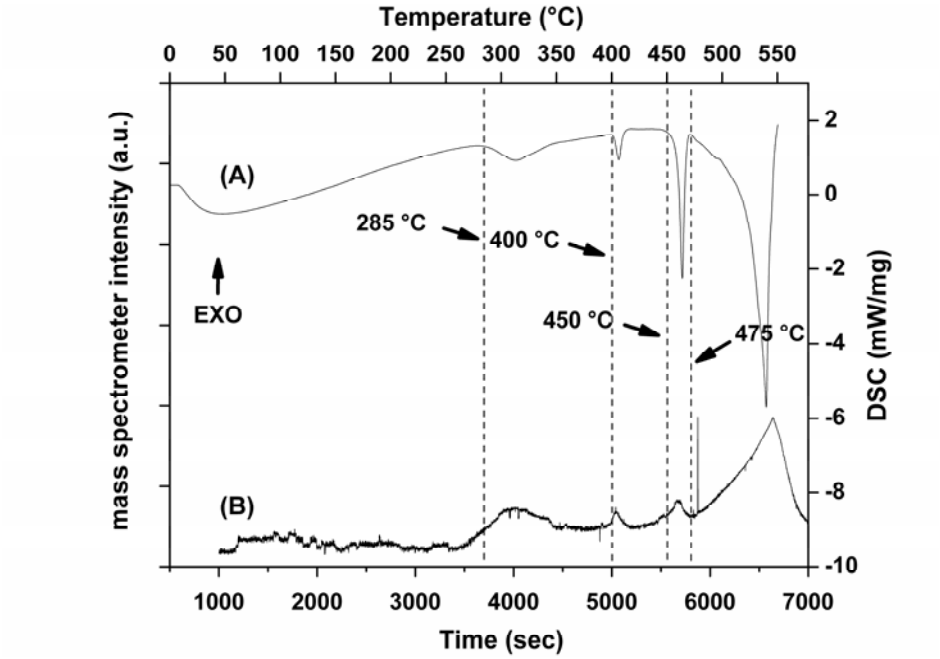

Figure 4.17: Differential scanning calorimetry and mass spectrometry of $2NaBH_4 + MgH_2$ from RT to 550°C at a rate of 5 °Cmin^{-1} in 150 mLmin^{-1} argon flow (curve A - DSC analysis ; curve B - mass spectrometry showing hydrogen release).

4.2.4 In-situ X-ray diffraction analysis

To further investigate the two-step dehydrogenation mechanism in the $2NaBH_4 + MgH_2$ system, in-situ powder X-ray diffraction (SR-PXD) analysis of the desorption reaction was carried out in similar conditions to the volumetric analysis in figure 4.16. Figure 4.18 shows the SR-PXD patterns (λ = 1.09719 Å) of $2NaBH_4 + MgH_2$ desorbed in 0.1 bar hydrogen pressure from room temperature to 400°C at a rate of 5 $^{o}Cmin^{-1}$ and then held isothermally for 2 hours. Between room temperature and 280°C, a decrease in the diffracted peak intensity of both $NaBH_4$ and MgH_2 peaks was observed. It is not thought that this reduction is due to any reaction since no product was detected. However artifacts arising from sample displacement from the beam focus during heating may be responsible. It was observed that at about 285°C MgH_2 began to decompose, as expected and metallic Mg was formed. Further at about 350°C the Mg began to react with $NaBH_4$ to form MgB_2. NaH was not detected in the in-situ analysis because of its amorphous nature at such a high temperature [16].

Furthermore, the evolution of phases during the desorption reaction was analyzed (see figure 4.19) using the normalized area of selected peaks as a function of temperature and time. Room temperature to 280°C is characterized by a decrease in the integrated areas of the $NaBH_4$ and MgH_2 peaks as discussed earlier. A decrease in peak intensity of MgH_2 as well as an increase in the integrated area of Mg is observed above 285°C. While, from about 350°C up to 400°C, a decrease in the intensity of $NaBH_4$ and Mg and the intensity of MgB_2 begin to rise simultaneously. Further increase in the intensity of MgB_2 is noticed

during isothermal heating even though no Mg and $NaBH_4$ are left. In addition, a slight anomalous behaviour is observed around 400°C where the signal associated with Mg stops decreasing and later drops away, while concurrently, the signal related to MgB_2 increases sharply, stops briefly and proceeds again for several minutes.

The difference in the rate of consumption of Mg and the formation of MgB_2 imply a likely presence of one or more intermediate reactions involving Mg/B-containing species. The detailed mechanism of desorption reaction in this system will be discussed in chapter 5.

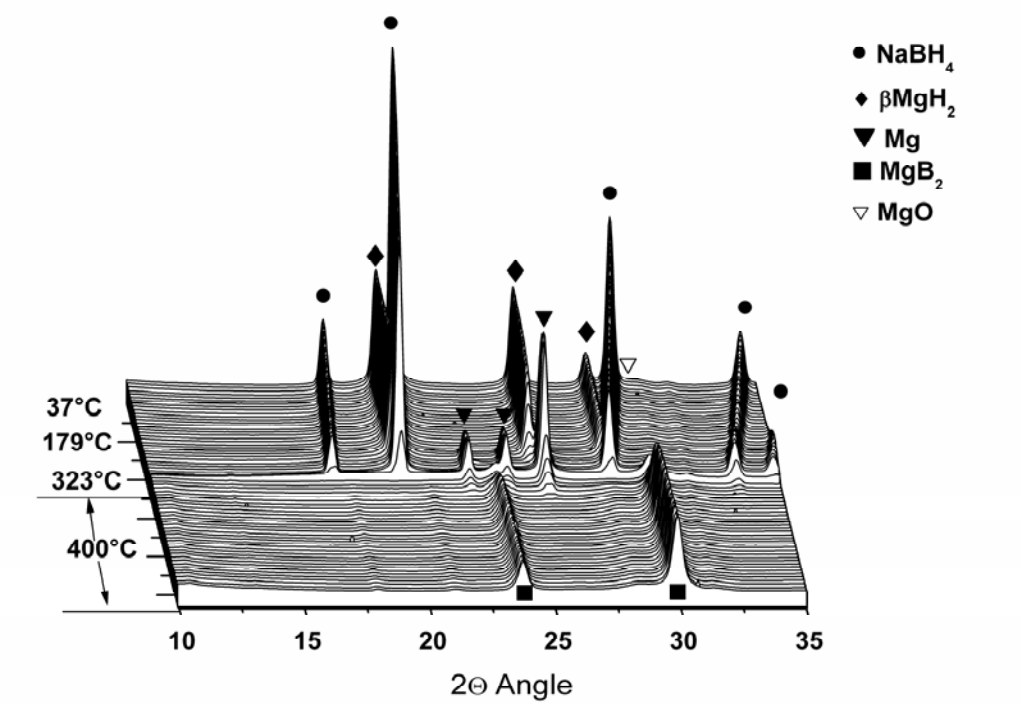

Figure 4.18: in-situ powder X-ray diffraction (SR-PXD) patterns of as-milled $2NaBH_4 + MgH_2$ desorbed in 0.1 bar H_2, from room temperature to 400 ^oC at 5 $°Cmin^{-1}$and held isothermally (λ = 1.09719 Å). Symbols: ● $NaBH_4$, ♦ βMgH_2, ▼□ MgO, ■MgB_2).

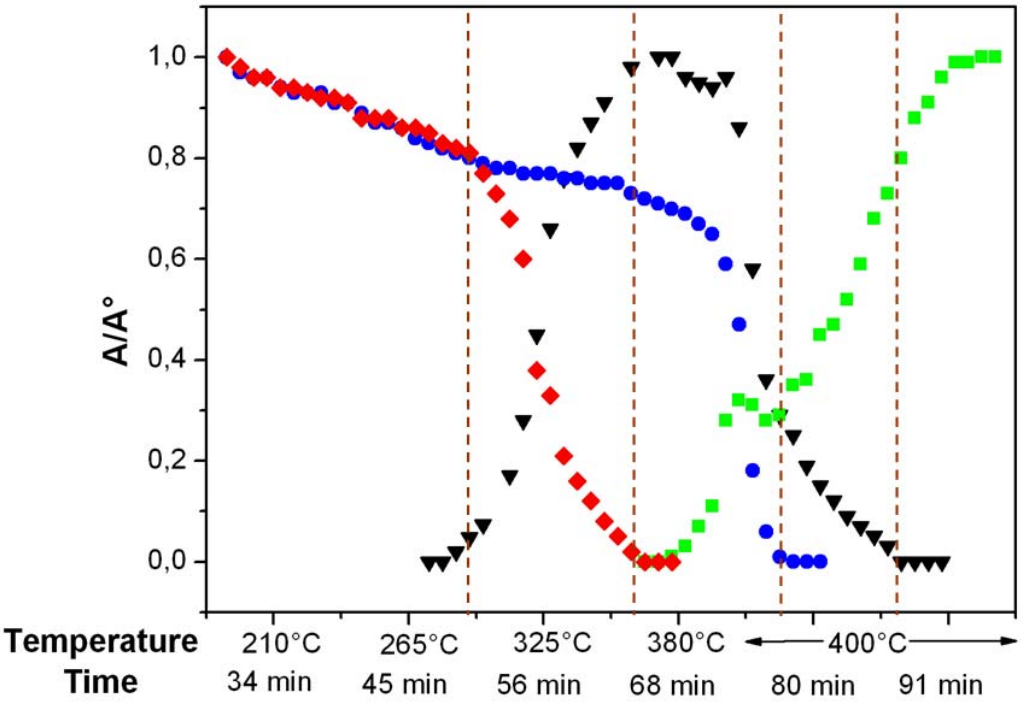

Figure 4.19: Normalized integrated diffracted intensity (A/A°) of reflections from the system $2NaBH_4 + MgH_2$ heated in 0.1 bar H_2 from RT to 400°C at 5°C/min. Symbols: ● (111) cubic $NaBH_4$, ♦ (110) tetragonal βMgH_2, ■ (001) hexagonal MgB_2, ▼ (100) hexagonal Mg.

4.2.5 Transmission electron microscopy analysis

Microstructural analysis was carried out on the reaction products of $2NaBH_4 + MgH_2$ after desorption in 0.1 bar hydrogen pressure from room temperature to 450 ^oC. Figures 4.20-4.22 shows the selected area electron diffraction pattern, high resolution and bright field images of the products after the desorption

reaction. From the indexed diffraction patterns in figure 4.20, the presence of NaH and MgB_2 are both clearly observed, indicating a complete dehydrogenation reaction in the sample according to the equation 4.4.

Similarly, the high resolution electron microscopy image of the same sample in figure 4.21 shows lattice fringes from both NaH and MgB_2 as indicated by $d_{(100)}$ = 0.2671 nm / $d_{(101)}$ = 0.2127 nm reflections of MgB_2 and $d_{(111)}$ = 0.2830 nm / $d_{(220)}$ = 0.1730 nm reflections of NaH. In the bright field image (see figure 4.22), plate-like structures of MgB_2 with typical dimensions of 10 - 20 nm by 50 - 200 nm in the in-plane direction are observed. This observation indicates that particles of MgB_2 grow as plates embedded in NaH during desorption reaction. A further discussion of this phenomenon is in chapter 5.

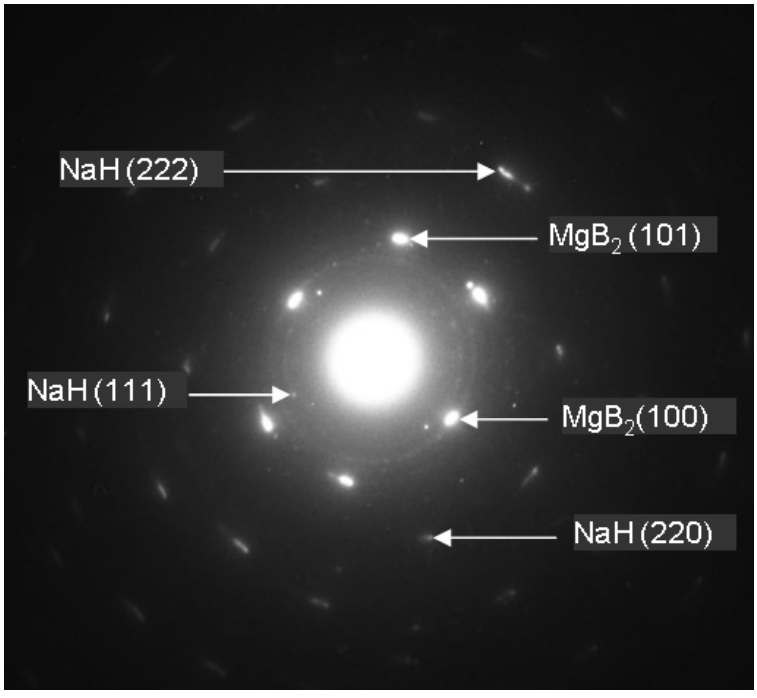

Figure 4.20: Selected area electron diffraction pattern (SAED) of $2NaBH_4$ + MgH_2 after desorption in 0.1 bar H_2 at 450 ^oC (JEOL-JEM 2010 at 200kV).

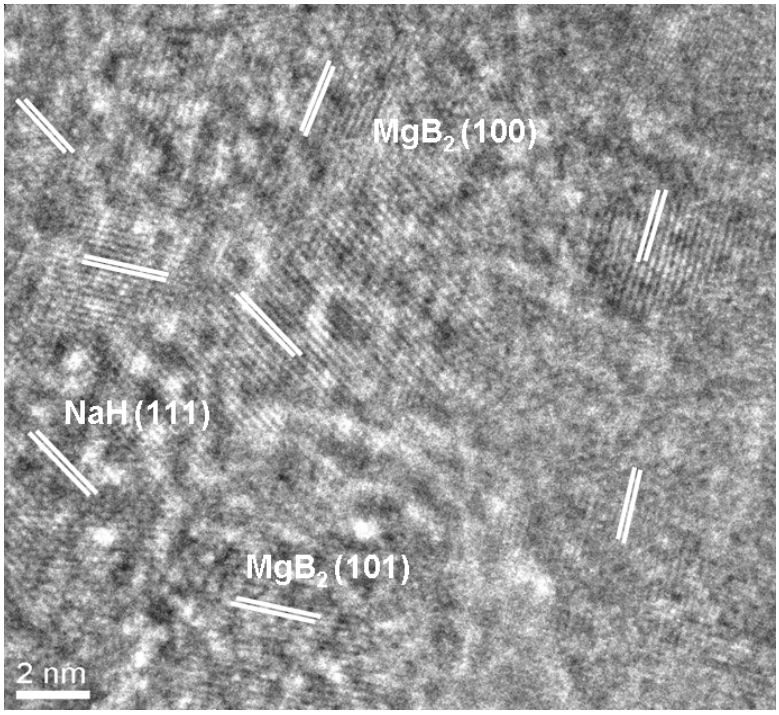

Figure 4.21: HRTEM image of $2NaBH_4 + MgH_2$ after desorption in 0.1 bar H_2 at 450 ^oC (JEOL-JEM 3000F at 300kV)**.**

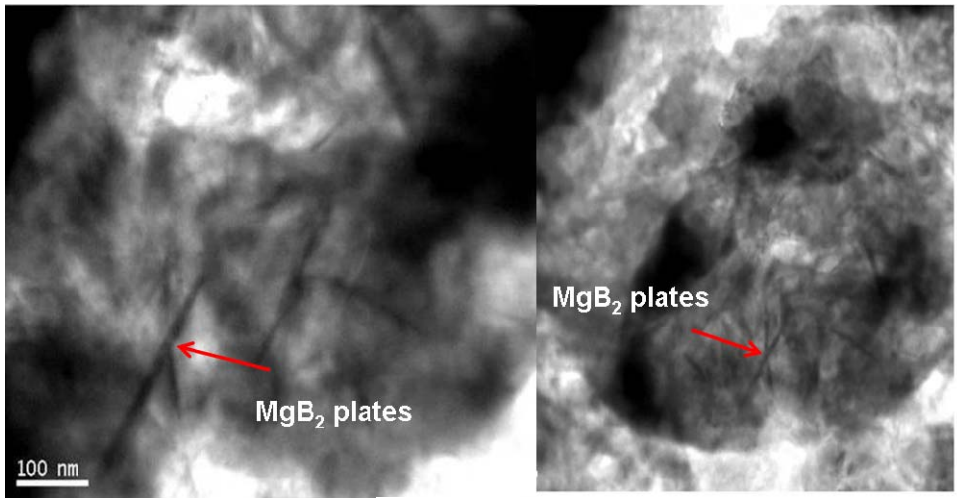

Figure 4.22: Bright field image of $2NaBH_4 + MgH_2$ after desorption in 0.1 bar H_2 at 450 ^oC showing plates of MgB_2 (red-arrowed) (JEOL-JEM 2010 at 200kV).

4.3 Desorption in $2NaBH_4 + MgH_2$ at low temperature

As indicated earlier by volumetric analysis in section 4.2.2, the dehydrogenation reaction in $2NaBH_4 + MgH_2$ proceeds in two steps, although at higher temperatures than predicted by the concept of reactive hydride composites. To shed more light on the reaction mechanism in this hydride composite, volumetric measurement was performed at 0.1 bar hydrogen pressure, from room temperature to 280 ^oC at a heating rate of 3 $^oC\ min^{-1}$. The kinetic analysis in figure 4.23 indicates that only about 1.4 wt % of hydrogen was released from the sample.

To determine the phases present, microstructural examination was carried out on the products of the desorption reaction. Figures 4.24 shows the bright field image and selected area electron diffraction pattern (Inset) of $2NaBH_4 + MgH_2$ after desorption in 0.1 bar hydrogen pressure from room temperature to 280 ^oC. The analysis reveal hexagonal reflections of (101) Mg indicating that MgH_2 had desorbed hydrogen. In addition, cubic reflections of (111) and (022) $NaBH_4$ were observed implying that only MgH_2 decomposed under these temperature and pressure conditions. No intermediate crystalline phases were detected at this temperature unlike the case during absorption at 280 ^oC (see section 4.16).

By this measurement, it is seen that the onset desorption temperature of MgH_2 in the composite had decreased slightly compared to that of its pure state [66].

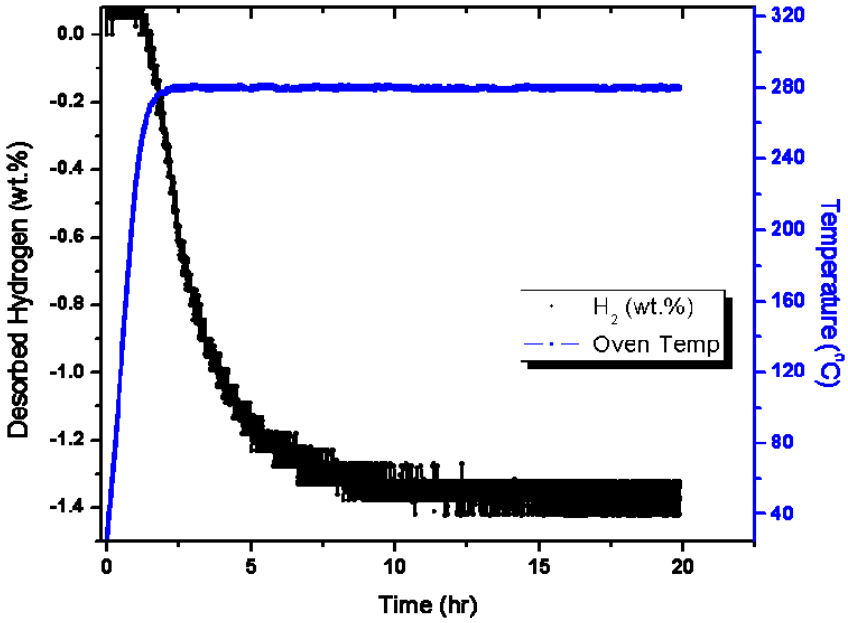

Figure 4.23: Desorption kinetics of as-milled $2NaBH_4 + MgH_2$ heated from room temperature to 280 ^oC at a rate of $3^oC\ min^{-1}$, in 0.1 bar H_2.

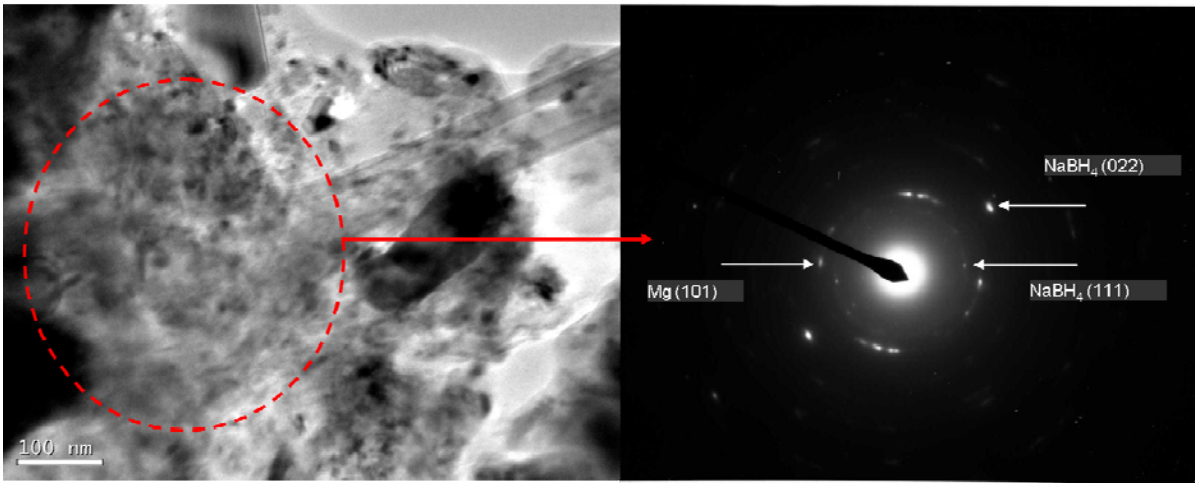

Figure 4.24: Bright field and selected area electron diffraction pattern (SAED) of $2NaBH_4 + MgH_2$ after desorption in 0.1 bar H_2 at 280 ^oC (JEOL-JEM 2010 at 200kV).

For further understanding of the mechanism of hydrogen desorption in $2NaBH_4 + MgH_2$, the reaction products of $2NaBH_4 + MgH_2$ after desorption in 0.1 bar hydrogen pressure from room temperature to 350 ^oC were characterised by transmission electron microscopy.

Figure 4.25 shows the bright field image and selected area electron diffraction pattern of the sample which reveal the presence of hexagonal particles of pure Mg with a diameter of several hundreds of nanometers (see figure 4.25a). The clear observation of magnesium crystals is also confirmed by the selected area electron diffraction pattern (see figure 4.25b). As in the sample measured at 280 ^oC, this observation is due to the decomposition of MgH_2 alone from the $2NaBH_4 + MgH_2$ composite at 350 ^oC and corresponds to the first reaction step described in sections 4.2.2 and 4.2.3. Similarly, the presence of $NaBH_4$ - an unconverted reactant - was also observed as indicated by the (111) and (022) cubic reflections of $NaBH_4$.

In contrast to the sample measured at 280 ^oC, where only (101) hexagonal reflections of Mg were seen, both (101) and (211) hexagonal reflections of Mg were observed due to the decomposition of more MgH_2.

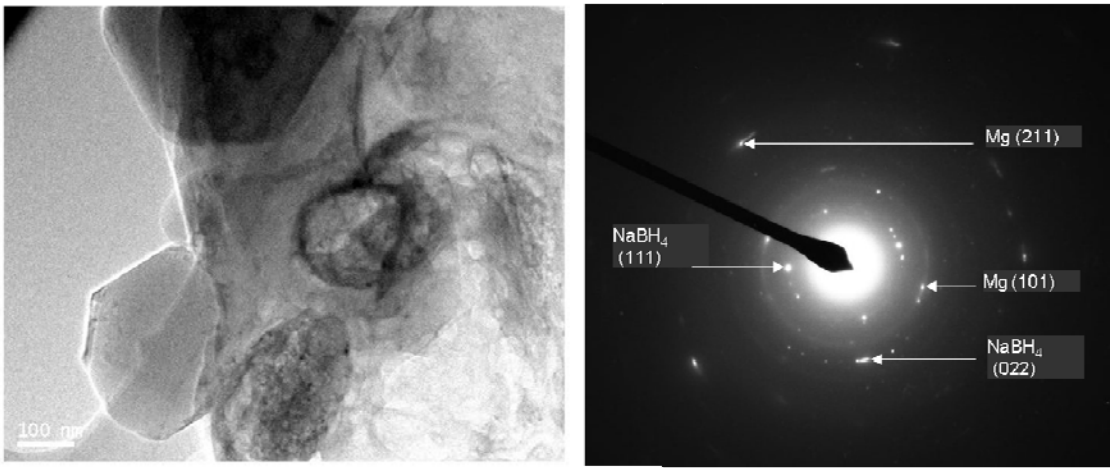

Figure 4.25: (a) Bright field image of $2NaBH_4 + MgH_2$ after desorption in 0.1 bar H_2 at 350 ^oC**. (b)** Selected area electron diffraction pattern (SAED) of $2NaBH_4 + MgH_2$ after desorption in 0.1 bar H_2 at 350 ^oC (JEOL-JEM 2010 at 200kV).

4.4 Effect of NaH/MgB_2 stoichiometric ratio

This section explores the effect of NaH/MgB_2 ratio on the sorption properties of NaH-MgB_2 composite. As clearly shown in section 4.1, kinetic and thermodynamic issues still limit hydrogen sorption in $2NaH + MgB_2$ composite, due to the formation of stable $NaMgH_3$ (perovskite-type hydride) during the absorption reaction.

To further investigate these problems, a three-to-one stoichiometric ratio of NaH/MgB_2 was used because it thermodynamically favours the formation of

$NaMgH_3$ instead of MgH_2 according to equation 4.5 and avoids the partial reaction of NaH and MgB_2 which was observed in the 2NaH + MgB_2 system.

$$3NaH + MgB_2 + 4H_2 \leftrightarrow 2NaBH_4 + NaMgH_3 \quad (4.5)$$

Assuming that the formation entropy ΔS_f of the composite is equal to the standard value, $-130 JK^{-1}mol^{-1}H_2$, the enthalpy change of reaction from the following standard formation enthalpies of NaH ($\Delta H_{(NaH)}$= -114.1 $kJmol^{-1}$ H_2) [99], MgB_2 ($\Delta H_{(MgB2)}$ = -91.85 $kJmol^{-1}$) [100], $NaBH_4$ ($\Delta H_{(NaBH4)}$ = -190.89 $kJmol^{-1}$ H_2) [68], and $NaMgH_3$ ($\Delta H_{(NaMgH3)}$ = -96.7 $kJmol^{-1}$ H_2) [97], is estimated to be 44.3 $kJmol^{-1}$ H_2.

It worth mentioning that this is the first time the investigation of such a stoichiometry is being reported. The examination of this system is of interest because the theoretical hydrogen storage capacity for this new composite system is 6.4 wt% which fully satisfies the gravimetric density criterion as stipulated by USDOE [1].

4.4.1 Hydrogen absorption in 3NaH + MgB_2 composite

Hydrogenation of 3NaH + MgH_2 was performed from room temperature to 300 ^oC at a rate of 3^oC min^{-1} under a hydrogen back pressure of 100 bars and held isothermally for several hours. Unlike the system with a 2:1 ratio of NaH/MgB_2, the kinetic curve in figure 4.26 shows complete absorption of hydrogen into the composite after 20 hours, according to equation 4.5. The initial

absorption of about 0.6 wt % as indicated by a red double arrow is an artifact due to the unstable high pressure at the beginning of measurement but stabilizes after a few minutes.

It is noteworthy that under these conditions, the direct synthesis of $NaMgH_3$ is possible. Perovskite-type hydride $NaMgH_3$ has been reported to decompose at 300 ^oC forming NaH and MgH_2 [97], and under these conditions the stability of hydrogen is greater in $NaMgH_3$ than MgH_2. This fact is corroborated by the results of microstructural analysis shown in figure 4.27 which clearly shows the presence of the expected reaction products; $NaBH_4$ and $NaMgH_3$.

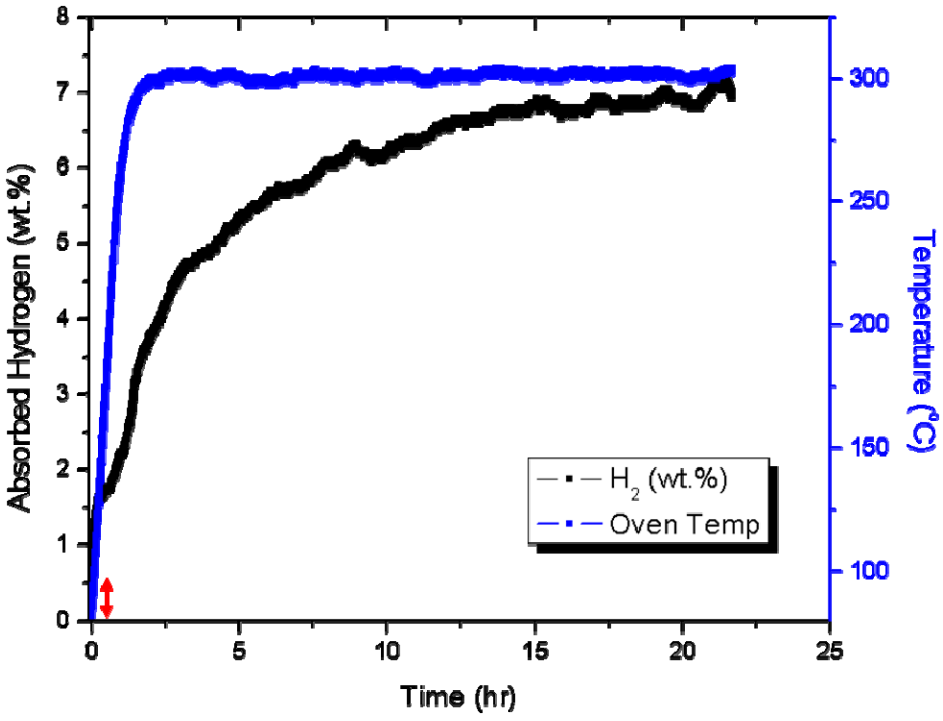

Figure 4.26: Absorption kinetics of as-milled 3NaH + MgB_2 heated from room temperature to 300 ^oC at a rate of 3^oC min^{-1}, in 100 bar H_2. The red double arrow indicates an artifact due to unstable high pressure at the start of measurement.

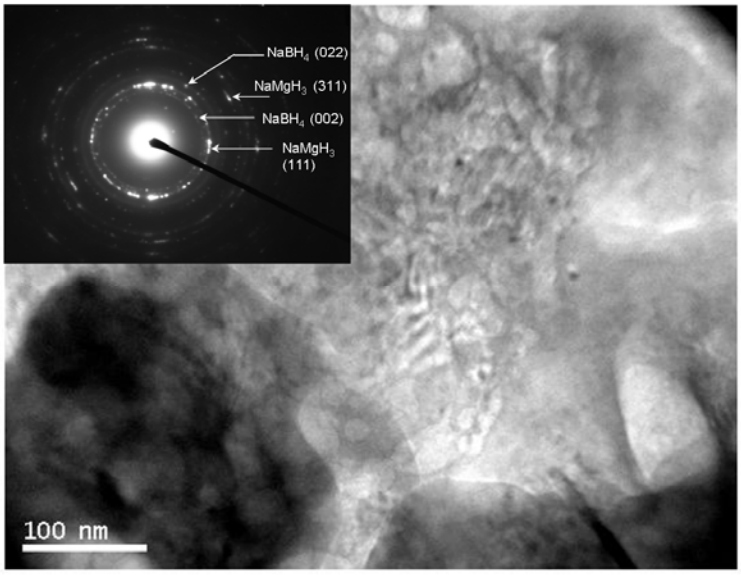

Figure 4.27: Bright field and selected area electron diffraction pattern (SAED) of 3NaH + MgB_2 after absorption at 300 ^oC in 100 bar H_2 (JEOL-JEM 2010 at 200kV).

4.4.2 Hydrogen desorption in $2NaBH_4 + NaMgH_3$ composite

Reversibility is an important requirement of metal hydrides. Therefore to test the reversibility of hydrogen sorption in this composite system, dehydrogenation was performed on $NaMgH_3$ + $2NaBH_4$ from room temperature to 450 ^oC a rate of 3^oC min^{-1} under a hydrogen back pressure of 1 bar (see figure 4.28). The sample was initially heated to 400 ^oC and held isothermally for 3 hours and finally heated further to 450 ^oC and kept in isothermal condition for several hours. Approximately 2.3 wt% hydrogen was released from the composite at 400 ^oC. Further increase in temperature to 450 ^oC led to more release of hydrogen

reaching a total capacity of 7.0 wt% hydrogen. Considering that the theoretical capacity of this system is 6.4 wt% hydrogen, it is most likely that some additional hydrogen was released by the decomposition of NaH. NaH is a very stable compound but decomposes into Na + ½H_2 at temperatures above 400 ^oC, with a reaction enthalpy of about 114.1 $kJmol^{-1}H_2$ [99, 101]. The multi-step reaction as well as the presence of Na along with MgB_2 particles in the products of desorption implies that the dehydriding reaction follows the suggested path in equation 4.6.

$$2NaBH_4 + NaMgH_3 \rightarrow 3NaH + MgB_2 + 4H_2 \rightarrow 3Na + MgB_2 + 5½H_2 \quad (4.6)$$

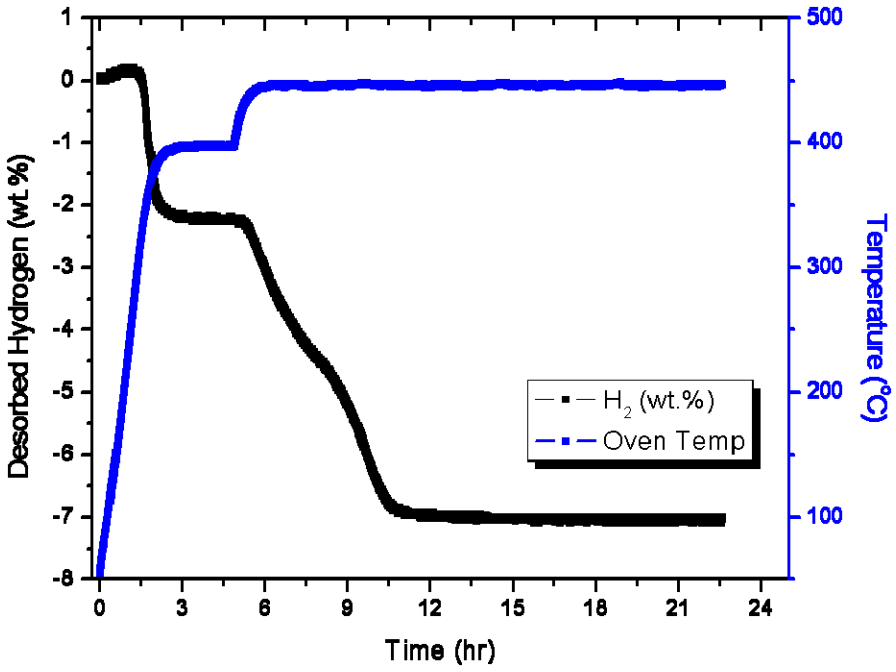

Figure 4.28: Kinetics of hydrogen desorption in as-milled $2NaBH_4 + NaMgH_3$ heated from room temperature to 450 ^oC at a rate of 3^oC min^{-1}, in 1 bar H_2.

Microstructural examination carried out on the products of desorption reaction indicate the presence of Na and MgB_2 particles (see figure 4.29). The presence of Na confirms that the extra amount of hydrogen released from the sample was due to the decomposition of NaH. Like in the $2NaBH_4 + MgH_2$ composite shown in figure 4.22, plate-like structures of MgB_2 with typical dimensions of 10 - 15 nm by 50 - 150 nm in the in-plane direction are observed.

Reversible hydriding cannot be achieved in this hydride composite under the conditions of 100 bar hydrogen and 400 ^{o}C because the hydrogenation of elemental Na thermodynamically requires very high temperatures.

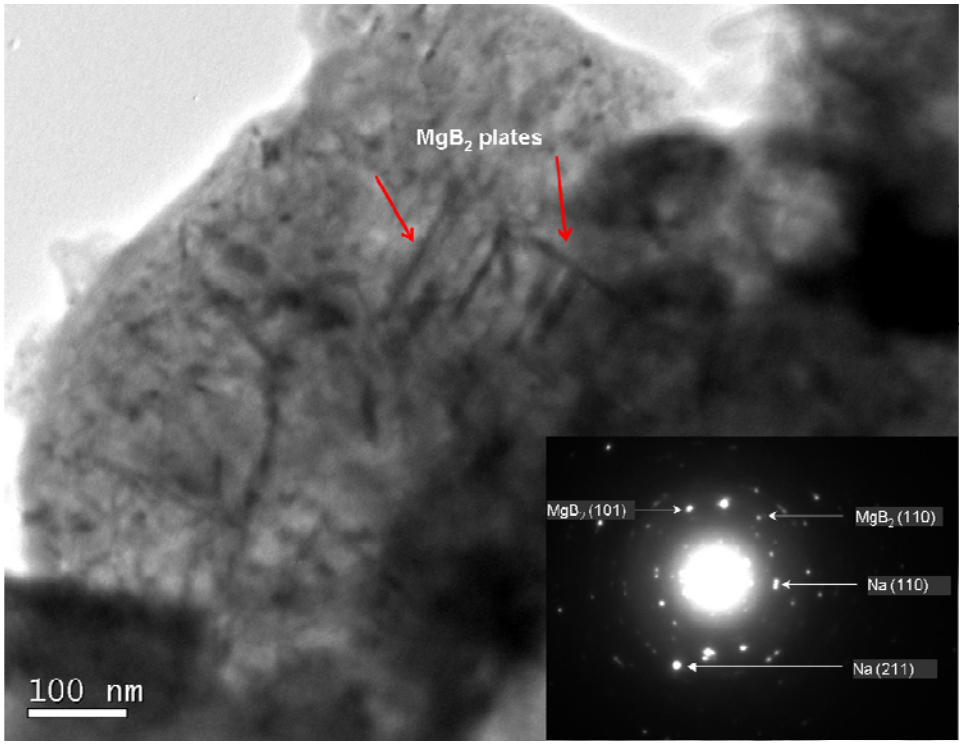

Figure 4.29: Bright field and selected area electron diffraction pattern (SAED) of $2NaBH_4 + NaMgH_3$ after desorption at 450 ^{o}C in 1 bar H_2 showing plates of MgB_2 (JEOL-JEM 2010 at 200kV).

5.0 Reaction mechanism in $NaBH_4$ - MgH_2 /$NaMgH_3$ composites

5.1 Mechanism of Hydrogen desorption

Experimental analysis of the dehydrogenation of $2NaBH_4 + MgH_2$, in sections 4.2 and 4.3 has clearly demonstrated that the release of hydrogen from the composite is a multistep reaction and does not follow the single pathway envisaged in the approach of reactive hydride composites This has also been observed in other investigations [14-16]. Volumetric analysis in figure 4.16 has shown that these reactions are kinetically sluggish despite the increased thermodynamic driving force.

Considering the high temperature and low pressure conditions applied in these measurements, the partial decomposition of $NaBH_4$ into the intermediate phase of $Na_2B_{12}H_{12}$ has been proposed [102, 103]. It is well established by NMR and Raman studies that metal borohydrides ($M(BH_4)n$ decompose via a multi-step reaction with the formation of a stable $M_{2/n}B_{12}H_{12}$ intermediate species [104-106].

The chemical structure of $M_{2/n}B_{12}H_{12}$ consists of closo-dodecaborate $[B_{12}H_{12}]^{2-}$ anions (figure 4.31) with hydrogen atoms positioned radially to each boron atom. The boron atoms form icosahedral units similar to those in pure boron (figure 4.30) with B-B bond length of 0.177-0.181nm for $[B_{12}H_{12}]^{2-}$ anions and 0.175 - 0.180nm for pure α-boron [107]. It is probable that the formation of this intermediate complex during desorption is easier than the direct formation of MgB_2.

The inactivity of this anion is due to its icosahedral structural symmetry with contact surfaces. Nonetheless $Na_2B_{12}H_{12}$ cannot be directly observed by in-situ XRD or TEM-SAED due to its amorphous structure which is integrated into the background. It is also possible that pure boron is formed during the desorption reaction since it possesses a very similar icosahedral structure to $[B_{12}H_{12}]^{2-}$ anion [107]. However, this would imply that MgB_2 is directly formed from Mg and B thereby having to cope with kinetic problems akin to those observed in the synthesis of MgB_2 for superconductor applications [108].

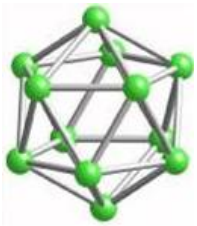

Figure 4.30: Structure of B_{12} icosahedral units of pure boron.

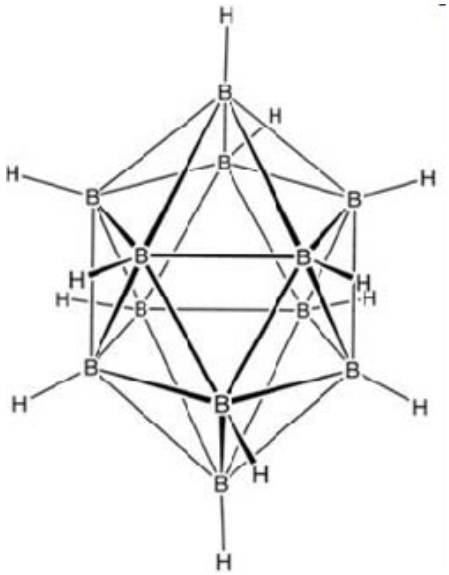

Figure 4.31: Structure of $[B_{12}H_{12}]^{2-}$ anion in $M_{2/n}B_{12}H_{12}$.

A reaction pathway for the dehydrogenation of $2NaBH_4 + MgH_2$ can be proposed as follows;

$2NaBH_4 + MgH_2 \rightarrow 2NaH + MgB_2 + 4H_2$

Step 1: $MgH_2 \rightarrow Mg + H_2$ (0.1 bar H_2, 280 - 350 ^oC)

Step 2a: $2NaBH_4 \rightarrow 1/6Na_2B_{12}H_{12} + 5/3NaH + 13/6H_2$ (0.1 bar H_2, >350 - 450^oC)

Step 2b: $1/6Na_2B_{12}H_{12} + Mg \rightarrow MgB_2 + ⅓NaH + 5/6H_2$ (0.1 bar H_2, >350 - 450 ^oC)

In this scheme, the first step involves the decomposition of MgH_2 which results in the formation of free metallic Mg. In the second and third steps, the formation of MgB_2 is facilitated through intermediate stages involving the decomposition of $NaBH_4$. Figure 4.19 shows that step 2b is slower than step 2a because $NaBH_4$ is completely decomposed long before the formation MgB_2 is complete. However, it can be seen that MgB_2 begins to form as soon as the first $Na_2B_{12}H_{12}$ is formed. Step 2a resembles a eutectoid reaction where two new phases grow from a single solid phase so that a fine scale microstructure should be favoured to facilitate diffusion. On the other hand in step 2b where two solid phases react to form a mixture of products will be strongly hindered by the products, forming a diffusion barrier between the reactants, as in a peritectoid reaction.

For complete dehydrogenation of this system, temperatures up to 450ºC are required, which are much higher than temperatures predicted theoretically. Hence the desorption reaction is kinetically restricted. However, it should be noted that lower temperatures have proved sufficient for complete decomposition

of $NaBH_4$ in the composite as compared to those required for pure $NaBH_4$ [68, 70].

From the foregoing analysis, the rate limiting step in the dehydrogenation of $2NaBH_4 + MgH_2$ could be associated with the growth of MgB_2 at the interface between Mg and $NaBH_4$ where the intermediate phase forms a barrier to diffusion. This implies that the desorption reaction is diffusion-controlled with the likely presence of localized constant reaction interfaces which causes MgB_2 to grow as plates as seen in figures 4.22 and 4.29. Restricted nucleation and growth of MgB_2 was also proposed for the composite system of MgH_2 + 20 wt.% $NaBH_4$, where the decomposition of $NaBH_4$ and the formation of MgB_2 did not occur until about 405 °C [16]. Furthermore, these issues arising from the formation of MgB_2 through intermediate steps could account for the differences in the rate of consumption of Mg and the formation of MgB_2 and suggests the possible presence of more intermediate reactions involving Mg and B species (see figure 4.19).

The decomposition of $2NaBH_4 + MgH_2$ reactive hydride composite takes place by solid state reaction with hydrogen released according to the suggested equation. Also, the desorption reaction in this complex hydride requires mass transport of the constituent elements. Electron microscopy has shown that sorption reactions primarily take place at interfaces. Therefore hydrogen has to be transported through the bulk of the composite to the surface, accompanied by the interdiffusion of B and Mg at the growing interface.

The most preferred route for mass transport in a bulk crystalline material is by means of lattice defects. Hence, it is also essential to identify the predominant defects in this composite hydride and to determine their energies of formation, so as to ascertain their contribution to the mechanism of desorption reaction.

5.2 Mechanism of Hydrogen absorption

As discussed in section 4.1, the hydrogenation reaction of $2NaH + MgB_2$ composite is partial and takes place in multi steps, leaving behind residues of the starting reactants in the final product. Based on combined volumetric analysis, in-situ powder x-ray diffraction and TEM analyses, it is logical to state that the formation of perovskite-type $NaMgH_3$ during the hydrogenation reaction of $2NaH + MgB_2$ adversely limit the rate of reaction. It is obviously detrimental to the absorption process as it binds NaH and limits the formation of $NaBH_4$ from the reaction between NaH, B and H_2.

From the HRTEM analysis in figure 4.8a, it is clear that $NaMgH_3$ forms between the MgB_2 and NaH particles. However due to the complexity of the reactions involved in solid state, there arise interdiffusion problems. Hence inter-atomic diffusion in this system is restricted because this perovskite phase acts as a barrier between the initial reactants (NaH and MgB_2). A similar situation was described during the formation of MgH_2 [109]. Furthermore, rapid hydrogen migration in $NaMgH_3$ has been observed and $NaMgH_3$ is considered to be a more

stable phase than MgH_2 [97]. Therefore, NaH is used up in the formation of $NaMgH_3$ which consequently reduces the yield of $NaBH_4$.

The role of the NaH-$NaBH_4$ molten phase observed during the absorption of 2NaH + MgB_2 is not clearly understood. Perhaps it has a kinetic effect on the reaction or rather forms a barrier to the diffusion of reacting species. However, the knowledge of hydrogen diffusion in complex hydrides is limited and could differ significantly from the general concept of hydrogen diffusion in binary metal hydrides. This molten phase apparently comprises only a molten salt mixture of NaH and $NaBH_4$. In effect, both phases re-emerge in the in-situ XRD analysis during the cooling cycle as the temperature fell below 370°C (see figure 4.7). This temperature is lower than the melting points of both individual compounds (NaH = >400°C) and ($NaBH_4$ = 505°C). Hence the measurement confirms a reaction involving only the two phases NaH and $NaBH_4$, and suggests a eutectic melting between NaH and $NaBH_4$.

The crystal structure of $NaMgH_3$ is consistent with the ABX_3 perovskite structure (space group *Pnma*) with each Na (A-site) cation surrounded by 12 H anions, and each Mg (B-site) cation coordinated with 6 H anions. Thus each H anion is bonded with 4 Na and 2 Mg cations resulting in a close packing of AX_3 layers with B-site cations in the centers of the BX_6 octahedra. The Mg-H interatomic bond lengths in $NaMgH_3$ are about 0.196 nm longer than the Mg-H interatomic bond lengths in MgH_2 [110].

The geometrical stability and bonding in $NaMgH_3$ significantly depends on its tolerance factor, lattice distortions and displacement of the MgH_6 octahedra. As

temperature increases during sorption reaction, the structure retains its *Pnma* symmetry. However, the atomic displacement of the MgH_6 octahedra (see figure 4.32) increases due to vibrations and dynamical disorder and causes the thermal atomic displacement ellipsoids of hydrogen in the MgH_6 octahedra to enlarge, spreading them towards the adjacent hydrogen atom [111] .

The overall impact of these structural variations on the activation energy for ion migration consequently leads to a high mobility of hydrogen atoms in the crystal.

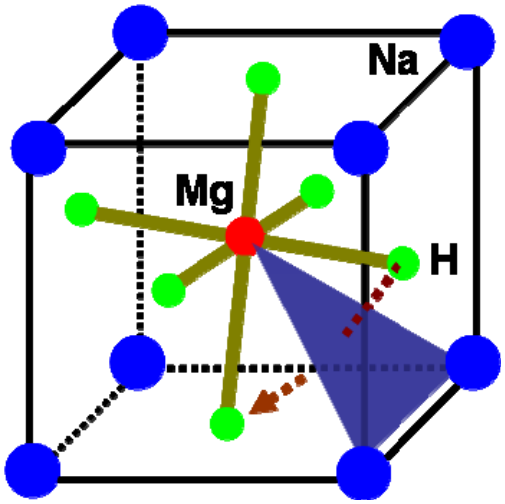

Figure 4.32: Schematic structure of $NaMgH_3$ sublattice with one hydrogen atom passing through a plane of 2Na + Mg to reach the adjacent vacant site.

Due to the incomplete reactions observed, a reaction pathway for the hydrogenation of 2NaH + MgB_2 is suggested as follows; where “UnPh” stands for the unknown phase and a, b, c, d, e, k, r, s, t, v, x, and y represent moles of the elements and compounds.

$2NaH + MgB_2 + kH_2$

$\rightarrow$ $xUnPh + sNaH + aMgB_2$ (50 bar H_2, 280 ^oC)

$\rightarrow$ $dNaMgH_3 + tNaH + bMgB_2$ (50 bar H_2, 330 ^oC)

$\rightarrow$ $eNaMgH_3 + yNaBH_4 + vNaH + cMgB_2 + rMg$ (50 bar H_2, 400 ^oC)

The first step is a solid state reaction leading to the formation of the unknown hydride phase at 280 ^oC. The second step involves the disappearance of the unknown phase above 320 ^oC, and the formation of perovskite type $NaMgH_3$ and possibly other unknown intermediate phases. In the third step, $NaBH_4$ and metallic Mg are formed following the partial decomposition of MgB_2.

It must be highlighted that very complex reactions with up to four phases in equilibrium are involved during hydrogen sorption of these reactive hydride composites, unlike in simple binary solid-gas systems. Hence significant mass transport of reacting species other than hydrogen occurs. It has been reported that the absorption reaction of $2NaH + MgB_2$ system is sensitive to the applied hydrogen pressure and if performed at lower H_2 pressures, the formation of $NaMgH_3$ can be suppressed resulting in more hydrogen intake into the system [96]. Therefore in order to avoid the unwanted incomplete reactions and the consequent loss in absorbed hydrogen capacity, the hydrogenation reaction should be carried out at temperature and hydrogen pressure conditions under which $NaMgH_3$ is unstable and cannot be formed by the reaction of NaH and MgH_2 as follows;

$NaH + MgH_2 \rightarrow NaMgH_3$

It may be possible that an $M_{2/n}B_{12}H_{12}$ complex is also formed as an intermediate phase during absorption of $2NaH + MgB_2 \rightarrow 2NaBH_4 + MgH_2$, considering its stability. However, the lower chemical potential of B in MgB_2 as compared to $Na_2B_{12}H_{12}$ would facilitate the direct formation of $NaBH_4$ thereby evading the formation of the intermediate phase.

In the $3NaH + MgB_2 \rightarrow 2NaBH_4 + NaMgH_3$ system, the high hydrogen mobility in perovskite-type $NaMgH_3$ discussed earlier plays a major role in the reversibility of hydrogen sorption observed in this composite system (see figures 4.26 and 4.28).

From the general concept of reactive hydride composites, the sorption reactions need be solid state reactions involving interdiffusion of atoms at low temperatures, however these reactions only proceed with sufficient speed at high temperatures as indicated by experiment.

6.0 Summary and conclusions

Reactive hydride composites offer promising properties as hydrogen storage materials for mobile applications due to their high gravimetric and/or volumetric energy densities. However, hydrogen sorption is a slow multi-step reaction and takes place at high temperatures. Hence, for realistic applications, it is vital to tune the kinetics and thermodynamics of hydrogen absorption and desorption reaction in these materials.

In this work the hydrogen sorption properties of $2NaBH_4 + MgH_2/2NaH + MgB_2$ and $2NaBH_4 + NaMgH_3/3NaH + MgB_2$ have been examined.

Results from volumetric analysis, in-situ powder x-ray diffraction and TEM analyses, reveal the formation of an unknown intermediate hydride phase during the hydrogenation reaction of $2NaH + MgB_2$. The subsequent formation of perovskite-type $NaMgH_3$ after the disappearance of the unknown phase impedes the absorption reaction by obstructing the formation of $NaBH_4$. As clearly indicated, NaH is used up in the formation of $NaMgH_3$ which consequently limits the formation of $NaBH_4$. Furthermore, the hydrogenation of the $2NaH + MgB_2$ system is sensitive to the hydrogen pressure at which the measurement is carried out .Therefore in order to overcome the partial reaction and the ensuing incomplete hydrogen intake, the absorption reaction could be performed at temperature and hydrogen pressure conditions that favour the instability of $NaMgH_3$.

The dehydrogenation of $2NaBH_4 + MgH_2$ is a multi-step reaction where $NaBH_4$ and MgH_2 are observed to decompose separately in 0.1 bar hydrogen up

to 450ºC. These temperatures are higher than those theoretically predicted from the thermodynamics of reactive hydride composites. Thus the desorption reaction is also kinetically restricted, although the onset desorption temperature of $NaBH_4$ in the composite is lower compared to pure $NaBH_4$ compound.

The observed kinetic constraints could result from the partial formation of intermediate $[B_{12}H_{12}]^{2-}$ complex species which have been confirmed to form during the decomposition of metal borohydrides. Therefore the desorption reaction of $2NaBH_4 + MgH_2$ is limited by the growth of MgB_2 at the interface between Mg and $NaBH_4$ where the intermediate phase forms a barrier to diffusion. These propositions however, require further confirmation using experimental methods that are sensitive to amorphous phases.

In respect to the $3NaH + MgB_2$ system, the direct formation of $NaMgH_3$ enhances the absorption reaction to attain full hydrogen capacity though at high temperatures too. The rapid hydrogen motion in $NaMgH_3$ perovskite plays a major role in the reversibility of hydrogen sorption observed in the hydride composite. Furthermore, it seems clear that the deliberate formation of $NaMgH_3$ may be advantageous, as compared to its accidental formation.

A good knowledge of the dominant mass transport phenomenon during sorption reactions in reactive hydride composites will contribute to a comprehensive understanding of the overall reaction mechanism and will permit directed optimization of their reaction kinetics and thermodynamics for efficient mobile applications in combination with a PEM fuel cell.

Bibliography

1. S. Satyapal, J. Petrovic, C. Read, G. Thomas, and G. Ordaz, *The U.S. Department of Energy's National Hydrogen Storage Project: Progress towards meeting hydrogen-powered vehicle requirements.* Catalysis Today, 2007. **120**(3-4): p. 246-256.
2. L. Schlapbach and A. Zuttel, *Hydrogen-storage materials for mobile applications.* Nature, 2001. **414**(6861): p. 353-358.
3. M. L. Trudeau, *Advanced materials for energy storage.* MRS bulletin, 1999. **24**(11): p. 23-26.
4. A. Züttel, *Materials for hydrogen storage.* Materials Today, 2003. **6**(9): p. 24-33.
5. B. Bogdanovi and M. Schwickardi, *Ti-doped alkali metal aluminium hydrides as potential novel reversible hydrogen storage materials.* Journal of Alloys and Compounds, 1997. **253-254**: p. 1-9.
6. P. Chen, Z. Xiong, J. Luo, J. Lin, and K. L. Tan, *Interaction of hydrogen with metal nitrides and imides.* Nature, 2002. **420**(6913): p. 302-304.
7. A. Züttel, A. Borgschulte, and S.-I. Orimo, *Tetrahydroborates as new hydrogen storage materials.* Scripta Materialia, 2007. **56**(10): p. 823-828.
8. J. J. Reilly and R. H. Wiswall, *Reaction of hydrogen with alloys of magnesium and copper.* Inorganic Chemistry, 1967. **6**(12): p. 2220-2223.
9. G. G. Libowitz, H. F. Hayes, and T. R. G. G. Jr., *The system zirconium-nickel and hydrogen.* Journal Physical Chemistry, 1958. **62**: p. 76.

10. G. Barkhordarian, T. Klassen, and R. Bormann, *International Patent pending, Publication No.: WO2006/063627 A1.* 2007.

11. G. Barkhordarian, T. Klassen, M. Dornheim, and R. Bormann, *Unexpected kinetic effect of MgB2 in reactive hydride composites containing complex borohydrides.* Journal of Alloys and Compounds, 2007. **440**(1-2): p. L18-L21.

12. J. J. Vajo, F. O. Mertens, S. L. Skeith, and M. P. Balogh, *International patent pending ed., WO 2005/097671.* 2006.

13. J. J. Vajo, S. L. Skeith, and F. Mertens, *Reversible Storage of Hydrogen in Destabilized $LiBH_4$.* The Journal of Physical Chemistry B, 2005. **109**(9): p. 3719-3722.

14. S. Garroni, C. Pistidda, M. Brunelli, G. B. M. Vaughan, S. Suriñach, and M. D. Baró, *Hydrogen desorption mechanism of $2NaBH_4 + MgH_2$ composite prepared by high-energy ball milling.* Scripta Materialia, 2009. **60**(12): p. 1129-1132.

15. J. F. Mao, X. B. Yu, Z. P. Guo, H. K. Liu, Z. Wu, and J. Ni, *Enhanced hydrogen storage performances of $NaBH_4$-MgH_2 system.* Journal of Alloys and Compounds, 2009. **479**(1-2): p. 619-623.

16. T. Czujko, R. A. Varin, Z. Wronski, Z. Zaranski, and T. Durejko, *Synthesis and hydrogen desorption properties of nanocomposite magnesium hydride with sodium borohydride (MgH2 + NaBH4).* Journal of Alloys and Compounds, 2007. **427**(1-2): p. 291-299.

17. J. E. Lennard-Jones, *Processes of adsorption and diffusion on solid surfaces*

Trans. Faraday Society, 1932 **28**: p. 333-359.

18. Z. X. Guo, C. Shang, and K. F. Aguey-Zinsou, *Materials challenges for hydrogen storage.* Journal of the European Ceramic Society, 2008. **28**(7): p. 1467-1473.

19. M. Song, J.-L. Bobet, and B. Darriet, *Improvement in hydrogen sorption properties of Mg by reactive mechanical grinding with Cr2O3, Al2O3 and CeO2.* Journal of Alloys and Compounds, 2002. **340**(1-2): p. 256-262.

20. N. E. Tran, S. G. Lambrakos, and M. A. Imam, *Analyses of hydrogen sorption kinetics and thermodynamics of magnesium-misch metal alloys.* Journal of Alloys and Compounds, 2006. **407**(1-2): p. 240-248.

21. H. I. Center, *Hydrogen: the renewable energy carrier for the 21st Century.* http://hydpark.ca.sandia.gov, 2007.

22. M. Dornheim, S. Doppiu, G. Barkhordarian, U. Boesenberg, T. Klassen, O. Gutfleisch, and R. Bormann, *Hydrogen storage in magnesium-based hydrides and hydride composites.* Scripta Materialia, 2007. **56**(10): p. 841-846.

23. F. Schuth, B. Bogdanovic, and M. Felderhoff, *Light metal hydrides and complex hydrides for hydrogen storage.* Chemical Communications, 2004(20): p. 2249-2258.

24. Z. Dehouche, T. Klassen, W. Oelerich, J. Goyette, T. K. Bose, and R. Schulz, *Cycling and thermal stability of nanostructured MgH2-Cr2O3*

composite for hydrogen storage. Journal of Alloys and Compounds, 2002. **347**(1-2): p. 319-323.

25. S. Orimo, Y. Nakamori, G. Kitahara, K. Miwa, N. Ohba, S. Towata, and A. Züttel, *Dehydriding and rehydriding reactions of LiBH4.* Journal of Alloys and Compounds, 2005. **404-406**: p. 427-430.
26. M. B. Smith and G. E. Bass, *Heats and Free Energies of Formation of the Alkali Aluminum Hydrides and of Cesium Hydride.* J. Chem. Eng. Data, 1963. **8**(3): p. 342-346.
27. K. Miwa, N. Ohba, S.-i. Towata, Y. Nakamori, and S.-i. Orimo, *First-principles study on lithium borohydride LiB H4.* Physical Review B, 2004. **69**(24): p. 245120.
28. J. Tobin, M. John, and R. Kolb, *Covalent transition metal, lanthanide, and actinide tetrahydroborate complexes.* Chemical Review, 1977.
29. B. G. Segal and S. J. Lippard, *Transition metal hydroborate complexes. 10. Crystal and molecular structure of tris(tetrahydroborato)tris(tetrahydrofuran)yttrium(III).* Inorg. Chem., 1978. **17**(4): p. 844-850.
30. Y. Nakamori, H. W. Li, K. Kikuchi, M. Aoki, K. Miwa, S. Towata, and S. Orimo, *Thermodynamical stabilities of metal-borohydrides.* Journal of Alloys and Compounds, 2007. **446-447**: p. 296-300.
31. K. Miwa, N. Ohba, S. Towata, Y. Nakamori, and S. Orimo, *First-principles study on copper-substituted lithium borohydride, (Li1-xCux)BH4.* Journal of Alloys and Compounds, 2005. **404-406**: p. 140-143.

32. Y. Nakamori and S.-i. Orimo, *Destabilization of Li-based complex hydrides.* Journal of Alloys and Compounds, 2004. **370**(1-2): p. 271-275.

33. C. X. Shang and Z. X. Guo, *Structural and desorption characterisations of milled (MgH2+Y,Ce) powder mixtures for hydrogen storage.* International Journal of Hydrogen Energy, 2007. **32**(14): p. 2920-2925.

34. V. Bérubé, G. Radtke, M. Dresselhaus, and G. Chen, *Size effects on the hydrogen storage properties of nanostructured metal hydrides: A review.* International Journal of Energy Research, 2007. **31**(6-7): p. 637-663.

35. J. J. Vajo and G. L. Olson, *Hydrogen storage in destabilized chemical systems.* Scripta Materialia, 2007. **56**(10): p. 829-834.

36. A. Zaluska, L. Zaluski, and J. O. Strom-Olsen, Applied Physics A, 2001. **72**: p. 157-165.

37. E. Veleckis, *Thermodynamic Investigation of the Li-Al. and Li-Pb Systems by the Hydrogen Titration Method.* Journal of the Less-Common Metals, 1980. **73**: p. 49-60.

38. J. J. Vajo, F. Mertens, C. C. Ahn, R. C. Bowman, and B. Fultz, *Altering Hydrogen Storage Properties by Hydride Destabilization through Alloy Formation: LiH and MgH2 Destabilized with Si.* J. Phys. Chem. B, 2004. **108**(37): p. 13977-13983.

39. G. Barkhordarian, T. Klassen, and R. Bormann, *Kinetic investigation of the effect of milling time on the hydrogen sorption reaction of magnesium catalyzed with different Nb2O5 contents.* Journal of Alloys and Compounds, 2006. **407**(1-2): p. 249-255.

40. R. L. Holtz, *Basic user's guide for NRL 6323 hydrogen storage system.* 1996.

41. G. Friedlmeier and M. Groll, *Experimental analysis and modelling of the hydriding kinetics of Ni-doped and pure Mg.* Journal of Alloys and Compounds, 1997. **253-254**: p. 550-555.

42. A. Zaluska, L. Zaluski, and J. O. Ström-Olsen, *Nanocrystalline magnesium for hydrogen storage.* Journal of Alloys and Compounds, 1999. **288**(1-2): p. 217-225.

43. A. Andreasen, T. Vegge, and A. S. Pedersen, *Compensation Effect in the Hydrogenation/Dehydrogenation Kinetics of Metal Hydrides.* J. Phys. Chem. B, 2005. **109**(8): p. 3340-3344.

44. J. Avrami, J. Chem. Phys. , 1939. **7**: p. 1103.

45. J. Avrami, J. Chem. Phys., 1940. **8**: p. 212.

46. J. Avrami, J. Chem. Phys., 1941. **9**: p. 177.

47. R. Schulz, S. Boily, L. Zaluski, A. Zaluska, P. Tessier, and J. O. Ström-Olsen, Innovations in Metallic Materials, 1995: p. 529.

48. R. Schulz, J. Huot, G. Liang, S. Boily, G. Lalande, M. C. Denis, and J. P. Dodelet, *Recent developments in the applications of nanocrystalline materials to hydrogen technologies.* Materials Science and Engineering A, 1999. **267**(2): p. 240-245.

49. C. Suryanarayana, *Mechanical alloying and milling.* Progress in Materials Science, 2001. **46**(1-2): p. 1-184.

50. L. Guoxian, W. Erde, and F. Shoushi, *Hydrogen absorption and desorption characteristics of mechanically milled Mg---35wt.%FeTi1.2 powders.* Journal of Alloys and Compounds, 1995. **223**(1): p. 111-114.

51. E. Ivanov, I. Konstanchuk, A. Stepanov, and V. Boldyrev, *Magnesium mechanical alloys for hydrogen storage.* Journal of the Less Common Metals, 1987. **131**(1-2): p. 25-29.

52. I. G. Konstanchuk, E. Y. Ivanov, M. Pezat, B. Darriet, V. V. Boldyrev, and P. Hagenmuller, *The hydriding properties of a mechanical alloy with composition Mg-25%Fe.* Journal of the Less Common Metals, 1987. **131**(1-2): p. 181-189.

53. G. Liang, J. Huot, S. Boily, A. Van Neste, and R. Schulz, *Catalytic effect of transition metals on hydrogen sorption in nanocrystalline ball milled MgH2-Tm (Tm=Ti, V, Mn, Fe and Ni) systems.* Journal of Alloys and Compounds, 1999. **292**(1-2): p. 247-252.

54. W. Oelerich, T. Klassen, and R. Bormann, *Metal oxides as catalysts for improved hydrogen sorption in nanocrystalline Mg-based materials.* Journal of Alloys and Compounds, 2001. **315**(1-2): p. 237-242.

55. N. Hanada, T. Ichikawa, S. Hino, and H. Fujii, *Remarkable improvement of hydrogen sorption kinetics in magnesium catalyzed with Nb2O5.* Journal of Alloys and Compounds, 2006. **420**(1-2): p. 46-49.

56. J. Huot, J. F. Pelletier, G. Liang, M. Sutton, and R. Schulz, *Structure of nanocomposite metal hydrides.* Journal of Alloys and Compounds, 2002. **330-332**: p. 727-731.

57. G. Barkhordarian, T. Klassen, and R. Bormann, *Fast hydrogen sorption kinetics of nanocrystalline Mg using Nb2O5 as catalyst.* Scripta Materialia, 2003. **49**(3): p. 213-217.

58. G. Barkhordarian, T. Klassen, and R. Bormann, *Effect of Nb2O5 content on hydrogen reaction kinetics of Mg.* Journal of Alloys and Compounds, 2004. **364**(1-2): p. 242-246.

59. G. Barkhordarian, T. Klassen, and R. Bormann, *Catalytic Mechanism of Transition-Metal Compounds on Mg Hydrogen Sorption Reaction.* J. Phys. Chem. B, 2006. **110**(22): p. 11020-11024.

60. B. Fromme, *d-d excitations in transition-metal oxides - Springer tracts in Modern Physics.* Springer, Berlin, 2001. **170**.

61. G. M. Schwab, Disc. Far. Soc, 1950. **8**: p. 166.

62. R. F. Klie, M. M. Disko, and N. D. Browning, *Atomic Scale Observations of the Chemistry at the Metal-Oxide Interface in Heterogeneous Catalysts.* Journal of Catalysis, 2002. **205**(1): p. 1-6.

63. B. Hammer, *Adsorbate-Oxide Interactions during the NO+CO Reaction on MgO(100) Supported Pd Monolayer Films.* Physical Review Letters, 2002. **89**(1): p. 016102.

64. J. P. Soulié, G. Renaudin, R. Cerný, and K. Yvon, *Lithium boro-hydride LiBH4: I. Crystal structure.* Journal of Alloys and Compounds, 2002. **346**(1-2): p. 200-205.

65. A. Züttel, S. Rentsch, P. Fischer, P. Wenger, P. Sudan, P. Mauron, and C. Emmenegger, *Hydrogen storage properties of LiBH4.* Journal of Alloys and Compounds, 2003. **356-357**: p. 515-520.

66. O. Kubaschewski, C. B. Alcock, and P. J. Spencer, *Materials Thermochemistry.* Pergamon Press, Oxford, 1993.

67. U. Bösenberg, S. Doppiu, L. Mosegaard, G. Barkhordarian, N. Eigen, A. Borgschulte, T. R. Jensen, Y. Cerenius, O. Gutfleisch, T. Klassen, M. Dornheim, and R. Bormann, *Hydrogen sorption properties of MgH2-LiBH4 composites.* Acta Materialia, 2007. **55**(11): p. 3951-3958.

68. D. S. Stasinevich and G. A. Egorenko, Russian Journal of Inorganic Chemistry, 1968. **13**: p. 341.

69. X. B. Yu, D. M. Grant, and G. S. Walker, *A new dehydrogenation mechanism for reversible multicomponent borohydride systems-The role of Li-Mg alloys.* Chemical Communications, 2006(37): p. 3906-3908.

70. J. Urgnani, F. J. Torres, M. Palumbo, and M. Baricco, *Hydrogen release from solid state $NaBH_4$.* International Journal of Hydrogen Energy, 2008. **33**(12): p. 3111-3115.

71. G. Barkhordarian, T. R. Jensen, S. Doppiu, U. Bosenberg, A. Borgschulte, R. Gremaud, Y. Cerenius, M. Dornheim, T. Klassen, and R. Bormann, *Formation of $Ca(BH_4)_2$ from Hydrogenation of CaH_2+MgB_2 Composite.* The Journal of Physical Chemistry C, 2008. **112**(7): p. 2743-2749.

72. J.-H. Kim, S.-A. Jin, J.-H. Shim, and Y. W. Cho, *Reversible hydrogen storage in calcium borohydride Ca(BH4)2.* Scripta Materialia, 2008. **58**(6): p. 481-483.

73. A. R. Yavari, J. F. R. de Castro, G. Vaughan, and G. Heunen, *Structural evolution and metastable phase detection in MgH2-5%NbH nanocomposite during in-situ H-desorption in a synchrotron beam.* Journal of Alloys and Compounds, 2003. **353**(1-2): p. 246-251.

74. Y. Kitano, Y. Fujikawa, N. Shimizu, S. Orimo, H. Fujii, T. Kamino, and T. Yaguchi, *Electron microscopy of Mg2Ni-H alloy synthesized by reactive mechanical grinding.* Intermetallics, 1997. **5**(2): p. 97-101.

75. B. Vigeholm, J. Kjøller, B. Larsen, and A. Schrøder Pedersen, *Hydrogen sorption performance of pure magnesium during continued cycling.* International Journal of Hydrogen Energy, 1983. **8**(10): p. 809-817.

76. B. Bokhonov, E. Ivanov, and V. Boldyrev, *A study of the electron-beam-induced decomposition of magnesium hydride single crystals.* Materials Letters, 1987. **5**(5-6): p. 218-221.

77. P. J. Herley and W. Jones, Zeit Phys. Chem., 1986. **147**: p. 785.

78. J. F. R. de Castro, S. F. Santos, A. L. M. Costa, A. R. Yavari, W. J. Botta F, and T. T. Ishikawa, *Structural characterization and dehydrogenation behavior of Mg-5 at.%Nb nano-composite processed by reactive milling.* Journal of Alloys and Compounds, 2004. **376**(1-2): p. 251-256.

79. O. Friedrichs, J. C. Sanchez-Lopez, C. Lopez-Cartes, T. Klassen, R. Bormann, and A. Fernandez, *Nb2O5 "Pathway Effect" on Hydrogen Sorption in Mg.* J. Phys. Chem. B, 2006. **110**(15): p. 7845-7850.

80. N. Hanada, E. Hirotoshi, T. Ichikawa, E. Akiba, and H. Fujii, *SEM and TEM characterization of magnesium hydride catalyzed with Ni nano-particle or Nb2O5.* Journal of Alloys and Compounds, 2008. **450**(1-2): p. 395-399.

81. J. W. Kim, J.-P. Ahn, S.-A. Jin, S. H. Lee, H.-S. Chung, J.-H. Shim, Y. W. Cho, and K. H. Oh, *Microstructural evolution of NbF5-doped MgH2 exhibiting fast hydrogen sorption kinetics.* Journal of Power Sources, 2008. **178**(1): p. 373-378.

82. M. Porcu, A. K. Petford-Long, and J. M. Sykes, *TEM studies of Nb2O5 catalyst in ball-milled MgH2 for hydrogen storage.* Journal of Alloys and Compounds, 2008. **453**(1-2): p. 341-346.

83. A. Léon, O. Kircher, H. Rösner, B. Décamps, E. Leroy, M. Fichtner, and A. Percheron-Guégan, *SEM and TEM characterization of sodium alanate doped with TiCl3 or small Ti clusters (Ti13·6THF).* Journal of Alloys and Compounds, 2006. **414**(1-2): p. 190-203.

84. M. Felderhoff, K. Klementiev, W. Grunert, B. Spliethoff, B. Tesche, J. M. B. v. Colbe, B. Bogdanovic, M. Hartel, A. Pommerin, F. Schuth, and C. Weidenthaler, *Combined TEM-EDX and XAFS studies of Ti-doped sodium alanate.* Physical Chemistry Chemical Physics, 2004. **6**(17): p. 4369-4374.

85. C. M. Andrei, J. Walmsley, D. Blanchard, H. W. Brinks, R. Holmestad, and B. C. Hauback, *Electron microscopy studies of lithium aluminium hydrides.* Journal of Alloys and Compounds, 2005. **395**(1-2): p. 307-312.

86. M. Danaie and D. Mitlin, *TEM analysis and sorption properties of high-energy milled MgH_2 powders.* Journal of Alloys and Compounds, 2009. **476**(1-2): p. 590-598.

87. J. W. Kim, O. Friedrichs, J.-P. Ahn, D. H. Kim, S. C. Kim, A. Remhof, H.-S. Chung, J. Lee, J.-H. Shim, Y. W. Cho, A. Züttel, and K. H. Oh, *Microstructural change of $2LiBH_4$/Al with hydrogen sorption cycling: Separation of Al and B.* Scripta Materialia, 2009. **60**(12): p. 1089-1092.

88. E. Deprez, A. Justo, T. C. Rojas, C. López-Cartés, C. Bonatto Minella, U. Bösenberg, M. Dornheim, R. Bormann, and A. Fernández, *Microstructural study of the $LiBH_4$-MgH_2 reactive hydride composite with and without Ti-isopropoxide additive.* Acta Materialia, 2010. **58**(17): p. 5683-5694.

89. F. Abbattista, P. Rolando, and G. B. Grassi, Ann. Chim (Rome), 1970. **60**: p. 426.

90. J. B. Goodenough, *Electronic and ionic transport properties and other physical aspects of perovskites.* Reports on Progress in Physics, 2004(11): p. 1915.

91. B. D. Cullity, *Elements of X-ray Diffraction.* Addison-Wesley Publishing Company, Inc., 1978.

92. Y. Cerenius, K. Stahl, L. A. Svensson, T. Ursby, A. Oskarsson, J. Albertsson, and A. Liljas, *The crystallography beamline I711 at MAX II.* Journal of Synchrotron Radiation, 2000. **7**: p. 203-208.

93. D. B. Williams and C. B. Carter, *Transmission Electron Microscopy: A Textbook for Materials Science, Springer, New York.* 1996.

94. R. D. Leapman and J. A. Hunt, *Comparison of detection limits for EELS and EDXS, Microsc. Microanal. Microstruct.* 1991. **2**: p. 231-244.

95. R. F. Egerton, *Electron Energy-Loss Spectroscopy in the Electron Microscopy, Plenum Press, New York.* 1986.

96. C. Pistidda, S. Garroni, C. B. Minella, F. Dolci, T. R. Jensen, P. Nolis, U. Boì^senberg, Y. Cerenius, W. Lohstroh, M. Fichtner, M. D. Baroì , R. d. Bormann, and M. Dornheim, *Pressure Effect on the 2NaH + MgB_2 Hydrogen Absorption Reaction.* The Journal of Physical Chemistry C. 2010. **114**(49): p. 21816-21823.

97. K. Ikeda, Y. Kogure, Y. Nakamori, and S. Orimo, *Reversible hydriding and dehydriding reactions of perovskite-type hydride NaMgH3.* Scripta Materialia, 2005. **53**(3): p. 319-322.

98. C. C. Nwakwuo, C. Pistidda, M. Dornheim, J. L. Hutchison, and J. M. Sykes, *Microstructural analysis of hydrogen absorption in 2NaH + MgB_2.* Scripta Materialia, 2011. **64**(4): p. 351-354.

99. T. N. Dymova and S. I. Bakum, Russian Journal of Inorganic Chemistry 1969. **14**: p. 1683.

100. J. A. Dilts and E. C. Ashby, Inorganic Chemistry, 1972. **11**: p. 1230.

101. M. D. Banus, J. J. McSharry, and E. A. Sullivan, Journal of American Chemical Society, 1955. **77**: p. 2007.

102. A. R. Pitochelli and F. M. Hawthorne, *THE ISOLATION OF THE ICOSAHEDRAL $[B_{12}H_{12}]^{-2}$ ION.* Journal of the American Chemical Society, 1960. **82**(12): p. 3228-3229.

103. J. E. Huheey, E. A. Keiter, and R. Keiter, *Inorganic Chemistry* 4th ed. . 1993: HarperCollins

104. S. I. Orimo, Y. Nakamori, N. Ohba, K. Miwa, M. Aoki, S. I. Towata, and A. Zuttel, *Experimental studies on intermediate compound of $LiBH_4$.* Applied Physics Letters, 2006. **89**(2).

105. N. Ohba, K. Miwa, M. Aoki, T. Noritake, S.-i. Towata, Y. Nakamori, S.-i. Orimo, and A. Zuttel, *First-principles study on the stability of intermediate compounds of $LiBH_4$.* Physical Review B, 2006. **74**(7): p. 075110.

106. S.-J. Hwang, R. C. Bowman, J. W. Reiter, Rijssenbeek, G. L. Soloveichik, J.-C. Zhao, H. Kabbour, and C. C. Ahn, *NMR Confirmation for Formation of $[B_{12}H_{12}]^{2-}$ Complexes during Hydrogen Desorption from Metal Borohydrides.* The Journal of Physical Chemistry C, 2008. **112**(9): p. 3164-3169.

107. N. N. Greenwood and A. Earnshaw, *Chemistry of the Elements*. 2 ed. 1997: Butterworth Heinemann.

108. S. Lee, *Crystal growth of MgB_2.* Physica C, 2003. **385**: p. 31-41.

109. C. M. Stander, Zeitschrift Fur Physikalische Chemie-Frankfurt, 1977. **104**: p. 229-238.

110. M. Bortz, B. Bertheville, G. Boettger, and K. Yvon, Journal of Alloys and Compounds, 1999. **287**: p. 4-6.

111. H. Wu, W. Zhou, T. J. Udovic, J. J. Rush, and T. Yildirim, *Crystal Chemistry of Perovskite-Type Hydride $NaMgH_3$: Implications for Hydrogen Storage.* Chemistry of Materials, 2008. **20**(6): p. 2335-2342.